

國立交通大學

材料科學與工程學系

博士論文

探討金及硒化鎘奈米粒子自身組織排列於
PS-*b*-P4VP 雙塊式高分子薄膜之 P4VP 區塊中
之集合電子傳導性質



Collective Electron Transport in Au and CdSe
Nanoparticles Self-Assembled in the
Poly(4-vinylpyridine) Nanodomains of a
Poly(styrene-*b*-4-vinylpyridine) Diblock Copolymer
Thin Film

研究生： 李中斌 (Chung-Ping Li)

指導教授： 韋光華 (Kung-Hwa Wei)

中華民國 九十五年 五月

Abstract

In this dissertation, thin films that consisted of Au and CdSe nanoparticles (NPs), self-assembled in a poly(4-vinylpyridine) (P4VP) nanodomain of poly(styrene-*b*-4-vinylpyridine) (PS-*b*-P4VP) diblock copolymer were prepared by polar interaction and solvent selectivity. Collective electron transport of these organic nanodomain confined nanoparticles were investigated.

From conductive atomic force microscopy and device measurements, we found that the electron tunneling rate constant in the case of CdSe quantum dots confined in a P4VP nanodomain is much larger than that in the randomly-distributed case. The calculated electron tunneling coefficient for hopping between confined CdSe quantum dots was 0.3 1/\AA . The conductivity of the CdSe/P4VP nanodomain increased upon increasing the amount of CdSe, following a percolation model (Chapter 2).

From the current–voltage characteristics of PS-*b*-P4VP thin films that consist of Au NPs, we found that the collective electron transport behavior of Au NPs sequestered in the spherical P4VP nanodomains was dictated by Coulomb blockade and was quasi one-dimensional, as opposed to the three-dimensional behavior displayed by Au NPs that had been dispersed randomly in homo-P4VP (Chapter 3).

Moreover, CdSe nanorods self-assembled in the P4VP nanodomains of a PS-*b*-P4VP diblock copolymer thin film were aligned under the influence of the polarization forces created by an applied electric field. The electron mobilities of CdSe/P4VP nanodomains incorporating the out-of-plane CdSe nanorods were much larger than those incorporating in-plane nanorods (chapter 4).

摘要

此論文主旨為利用有機 PS-*b*-P4VP 雙塊式高分子薄膜自身組織成週期性結構的特性作為模版並以選擇性分散之技術，分別將無機 Au、CdSe 奈米粒子侷限於 P4VP 奈米區塊中形成特定結構之奈米陣列，並探討此具有奈米侷限效應之奈米粒子之群體電子傳導特性。

利用導電的原子力顯微鏡及電性量測儀器，針對於具有奈米侷限效應之 CdSe 量子點/P4VP 奈米區塊進行量測，發現電子在此具奈米侷限效應之量子點間之傳導速度遠較不具侷限效應之量子點之傳導速度快。

利用低溫電性量測儀器，針對於具有奈米侷限效應之 Au 奈米粒子/P4VP 奈米區塊進行量測，在 78K 之低溫量測下，Au 奈米粒子具有庫侖阻塞效應，進而發現具有奈米侷限之奈米粒子呈現出趨近於一維電子傳導之特性。

此外，將 CdSe 奈米柱選擇性分散於 P4VP 奈米區塊中並在高溫下加入電場作為驅動力，製備出具方向性且大面積規則排列之 CdSe/P4VP 陣列，並量測加入電場前後之電子遷移速率。

Table of Content

Abstract	
摘要.....	
Chapter 1: Introduction	
1-1 Block Copolymers	1
1-2 Nanostructured Materials	12
1-3 Motivation and Scope of Dissertation	21
Chapter 2: Basic Electron Transport Theory	
2-1 Introduction	48
2-2 Conduction Mechanisms	48
2-3 Alkanethiol Self-assembled Monolayers Metal-Insulator-Metal Tunneling	49
Chapter 3: Enhanced Collective Electron Transport by CdSe Quantum Dots Self-Assembled in the Poly(4-vinylpyridine) Nanodomains of a Poly(styrene-<i>b</i>-4-vinylpyridine) Diblock Copolymer Thin Film	
3-1 Introduction	54
3-2 Methods and Analysis	55
3-3 Results and Discussions	57
3-4 Conclusions	65
Chapter 4: Collective Electron Transport in Au Nanoparticles Self-Assembled in the Poly(4-vinylpyridine) Nanodomains of a Poly(styrene-<i>b</i>-4-vinylpyridine) Diblock Copolymer Thin Film	
4-1 Introduction	75
4-2 Methods and Analysis	76
4-3 Results and Discussions	78
4-4 Conclusions	83
Chapter 5: The Orientation of CdSe Nanorods Affects the Electron Mobility of CdSe/P4VP Nanodomains Self-Assembled within a Poly(styrene-<i>b</i>-4-vinylpyridine) Diblock Copolymer Thin Film	
5-1 Introduction	93
5-2 Methods and Analysis	94

5-3 Results and Discussions96
5-4 Conclusions101

Chapter 6: Conclusions109

Chapter 7: References110



Figure List

Chapter 1: Introduction

- Figure 1-1-1** Schematic phase diagram showing the various ‘classical’ block copolymer morphologies adopted by linear diblock copolymer.....24
- Figure 1-1-2** Schematic of morphologies for linear ABC triblock copolymer. A combination of block sequence (ABC, ACB, BAC), composition and block molecular weights provides an enormous parameter space for the creation of new morphologies25
- Figure 1-2-1** The well-known structures of block copolymers in melt, solution or solid state26
- Figure 1-3-1** Schematic of various applications of block copolymers in nanotechnologies.....27
- Figure 1-3-2** Schematic of the production process of a metal nanodot array using block copolymer lithography28
- Figure 1-3-3** SEM image of polystyrene-*b*-polyferrocenyldimethylsilane mask, after the polystyrene has been removed by O₂ RIE29
- Figure 1-3-4** Schematic representation of high density nanowire fabrication in a polystyrene-*b*-poly(methylmethacrylate) matrix30
- Figure 1-3-5** The morphological transformation from a hexagonally packed cylinder structure of pure polystyrene-*b*-poly(4-vinylpyridine) (PS-*b*-P4VP) diblock copolymers to lamellar (CdS/P4VP)-*b*-PS composites.....31
- Figure 1-3-6** Schematic of selected distribution of TiO₂ nanoparticles in polystyrene-*b*-poly(methylmethacrylate) diblock copolymer.....32
- Figure 1-3-7** (a) Secondary electron SEM image of the surface of a thin film of a diblock copolymer–CdSe nanoparticle mixture spin-coated onto a silicon wafer and annealed at 170 °C for 2 days (image width, 250 nm) taken at 1-kV acceleration voltage. (b) Schematic representation of nanoparticle assembly at the poly(2-vinylpyridine) cylinders.33

Figure 1-3-8 TEM micrograph of a ternary blend of polystyrene-*b*-poly(ethylene propylene) + AuR₁ + SiO₂R₂ with inorganic filling fraction $f = 0.02$; respectively, after micro-sectioning normal to the layer direction (no stain)34

Figure 1-3-9 (a) Assembly of Au nanoparticles (core: 3.9 ± 1.0 nm; shell: polystyrene; (core+shell)=7.7 nm) into polystyrene-*b*-poly(2-vinylpyridine) diblock copolymers. (b) Assembly of Au nanoparticles (core: 3.9 ± 1.0 nm; shell: polystyrene and poly(2-vinylpyridine); (core+shell)=7.7 nm) into polystyrene-*b*-poly(2-vinylpyridine) diblock copolymers. (c), (d) The respective histograms of particle locations for the samples shown in (a) and (b). Reprinted with permission.....35

Figure 1-3-10 Cross-sectional transmission electron micrograph showing Au nanoparticles patterned within the poly(4-vinylpyridine) lamellae formed by a polystyrene-*b*-poly(4-vinylpyridine) diblock copolymer36

Figure 1-3-11 Schematic of synthesis of needle-like TiO₂ nanostructures with ordered patterns.....37

Figure 1-3-12 SEM image of an etched polystyrene-*b*-polyisoprene diblock, showing a fracture surface. The polystyrene network channels remaining after removal of polyisoprene are clearly visible38

Figure 1-4-1 Schematic illustration the density of state in semiconductors.39

Figure 1-4-2 EL spectra collected on ITO/PPV (400 Å)/CdSe(CdS)/Mg/Ag devices having average nanocrystal layer thicknesses of 100 (a), 200 (b), and 400 Å (c). (d) Show the voltage dependence of the ratio of integrated nanocrystal EL to integrated PPV EL for the device shown in (b)40

Figure 1-4-3 (a) The structure of regioregular P3HT. (b) The schematic energy level diagram for CdSe nanorods and P3HT showing the charge transfer of electrons to CdSe and holes to P3HT. (c) The device structure consists of a film ;200 nm in thickness sandwiched between an aluminum electrode and a transparent conducting electrode of PEDOT:PSS41

Figure 1-4-4 *I-V* curve of Al/Au-2NT NPs+PS/ Al. The arrows indicate the biasscanning directions and the inset the device structure.....42

Figure 1-4-5 (a) SEM image of a chain consisting of three Au nanoparticles incorporated in a system of source, drain, and gate metal electrodes. (b) Scheme of electrode pattern defined by electron beam lithography. (c) Drain current (I_D) versus source-drain voltage (VSD) characteristics of the SET transistor measured at 4.2 K with various gate voltages (V_G)43

Figure 1-4-6 (a) Preparation of “nanocrystal molecules” consisting of two or three DNA modified Au particles attached to a complementary DNA template. (b) TEM images of the binary AuNPs network materials supported on holey carbon grids....44

Figure 1-4-7 Schematic of a threshold voltage proportional to the linear array size45

Figure 1-4-8 (a) Representative TEM images of Au nanoparticles /silica mesophases. (b) I - V curves measured from 300 K to 78 K. The inset plots the zero-bias conductance (G_0) versus $1/T$. (c) At $T = 78$ K, current displays a power-law dependence for $V > V_T$ with scaling exponent $\alpha = 2.7$ (negative bias) and $\alpha = 3.0$ (positive bias).....46

Figure 1-4-9 (a) SEM image of self-assembled Co nanoparticles superlattice device (b) Device I - V characteristic, for $T = 2$ K (dark line) and 20, 40, and 70 K (light lines). (Inset) Plot of zero-bias conductance versus $1/T$. (c) For $V > V_T$, current displays a power-law dependence.....47

Chapter 2: Basic Electron Transport Theory

Figure 2-1 E - k relationship (symbols) generated from the length-dependent measurement data for alkanethiols. 53

Chapter 3: Enhanced Collective Electron Transport by CdSe Quantum Dots Self-Assembled in the Poly(4-vinylpyridine) Nanodomains of a Poly(styrene-*b*-4-vinylpyridine) Diblock Copolymer Thin Film

Figure 3-1 (a) TEM image of a thin film of 48% (CdSe/P4VP)-*b*-PS obtained without staining. (b) A schematic representation of the conductive-AFM imaging mode

employed. (c) Conductive-AFM image of a thin film of 48% (CdSe/P4VP)-*b*-PS.70

Figure 3-2 (a) *I*–*V* curves of thin film (CdSe/P4VP)-*b*-PS by conductive-AFM. The dotted lines denote best fits to the FN equation. Inset: The energy bands of the conductive-AFM tip, CdSe/P4VP monolayer, and the substrate. E_f is the electron Fermi energy inside the Pt, and ϕ_e is the barrier height between Pt and CdSe/P4VP. eV_a is the applied potential energy difference between the tip and the substrate. (b) Plot of the conductivity vs. the amount of CdSe in P4VP.71

Figure 3-3 (a) Plot of $-\ln(\sigma_{(CdSe/P4VP)-b-PS})$ vs. δ_e as measured by conductive-AFM and device. (b) Schematic diagram of the barrier height for electron tunneling from the conduction band of CdSe to the LUMO of P4VP and from the Fermi level of Au to the LUMO of an alkanethiol.72

Figure 3-4 (a) I_{ave} –*V* curves of thin film (CdSe/P4VP)-*b*-PS nanocomposites having various contents of CdSe as measured in a device. The dotted lines denote best fits to the FN equation. (b) Plot of the conductivity vs. the amount of incorporated CdSe in P4VP.73

Figure 3-5 (a) Small-angle X-ray scattering of bulk (CdSe/P4VP)-*b*-PS nanocomposites having various contents of CdSe. (b) A schematic representation of the cubic lattice model for the free volume per CdSe dot in a single P4VP domain. ...74

Chapter 4: Collective Electron Transport in Au Nanoparticles Self-Assembled in the Poly(4-vinylpyridine) Nanodomains of a Poly(styrene-*b*-4-vinylpyridine) Diblock Copolymer Thin Film

Figure 4-1 (a) Conventional, (b) high-resolution, and (c) cross-sectional TEM images, obtained without staining, of a thin film of 48% (Au NPs/P4VP)-*b*-PS.86

Figure 4-2 *I*–*V* curves of (a) 48% (Au NPs/P4VP)-*b*-PS and (b) Au NPs/homo-P4VP thin films measured at temperatures between 250 and 78 K. (c) Scaling behavior of the *I*–*V* curves of 48% (Au NPs/P4VP)-*b*-PS and Au NPs/homo-P4VP at 78 K. (d) Plots of V_T vs. *d* for the 48% (Au NPs/P4VP)-*b*-PS and Au NPs/homo-P4VP samples

having various contents of Au NPs.....87

Figure 4-3 (a) Small-angle X-ray scattering of bulk (Au NPs/P4VP)-*b*-PS nanocomposites having various contents of Au NPs. (b) Schematic representation of the cubic lattice model for the free volume per Au nanoparticle in a single P4VP domain.89

Figure 4-4 *I*–*V* Curves measured at 78 K for (Au NPs/P4VP)-*b*-PS and Au NPs/P4VP thin films. Details of the fitting and determination of the threshold voltages and scaling exponents are provided in the corresponding tables.....90

Figure 4-5 (a) *I*–*V* Curves, measured at 78 K, of (Au NPs/P4VP)-*b*-PS thin films having various contents of Au NPs. (b) Scaling behavior of the *I*–*V* curves of (Au NPs/P4VP)-*b*-PS having various contents of Au NPs at 78 K.91

Figure 4-6 (a) *I*–*V* Curves, measured at 78 K, of Au NPs/homo-P4VP thin films having various contents of Au NPs. (b) Scaling behavior of the *I*–*V* curves of Au NPs/homo-P4VP having various contents of Au NPs at 78 K.....92

Chapter 5: The Orientation of CdSe Nanorods Affects the Electron Mobility of CdSe/P4VP Nanodomains Self-Assembled within a

Poly(styrene-*b*-4-vinylpyridine) Diblock Copolymer Thin Film

Figure 5-1 TEM images, obtained without staining, of thin films of (a) 65%, (b) 48%, and (c) 33% (CdSe/P4VP)-*b*-PS.104

Figure 5-2 SEM images of 33% (CdSe/P4VP)-*b*-PS thin films prepared (a) in the absence and (b) in the presence of an applied electric field.105

Figure 5-3 Cross-sectional TEM images of 33% (CdSe/P4VP)-*b*-PS thin films prepared (a) in the absence of and (b) in the presence of an applied electric field. The insets display the respective HRTEM lattice images of a CdSe NR incorporated within a single P4VP nanodomain of (CdSe/P4VP)-*b*-PS. (c) A schematic depiction of the electron transport process.106

Figure 5-4 Averaged current density–electric field (*J*–*E*) curves of a single CdSe/P4VP nanodomain in a PS matrix incorporating various contents of (a)

out-of-plane and (b) in-plane CdSe NRs. The dashed lines denote best fits to the FN equation; the dotted lines denote best fits to the SCLC model, which includes the field-dependent mobility.....107

Figure 5-5 Orientation angle of the protruded CdSe NRs with respect to the plane of the P4VP-*b*-PS thin film as function of the electric field strength.108



Scheme & Table List

Chapter 2: Basic Electron Transport Theory

Table 2-1 Possible conduction mechanisms.....	52
--	----

Chapter 3: Enhanced Collective Electron Transport by CdSe Quantum Dots Self-Assembled in the Poly(4-vinylpyridine) Nanodomains of a Poly(styrene-*b*-4-vinylpyridine) Diblock Copolymer Thin Film

Scheme 3-1 Fabrication of a self-assembled (CdSe/P4VP)-*b*-PS thin film by incorporating selectively dispersed pre-synthesized CdSe QDs in P4VP domain... 66

Table 3-1 Conductivity (σ) and electron tunneling rate constant (k_{ET}) for confined and non-confined CdSe in P4VP domain as measured by conductive-AFM and in a device67

Table 3-2 Characteristic Properties of CdSe Quantum Dots.....68

Table 3-3 Electrical conductivity parameters for the CdSe/P4VP nanodomain.....69

Chapter 4: Collective Electron Transport in Au Nanoparticles Self-Assembled in the Poly(4-vinylpyridine) Nanodomains of a Poly(styrene-*b*-4-vinylpyridine) Diblock Copolymer Thin Film

Scheme 4-1 Fabrication of a self-assembled (Au NPs/P4VP)-*b*-PS thin film through the selective incorporation of dispersed pre-synthesized Au NPs into P4VP domains.84

Table 4-1 Details of the Fitting of $I-V$ Curves, Measured at 78 K, for (Au NPs/P4VP)-*b*-PS and Au NPs/P4VP Thin Films Having Various Contents of Au NPs, and Determination of the Threshold Voltages and Scaling Exponents.....85

Chapter 5: The Orientation of CdSe Nanorods Affects the Electron Mobility of CdSe/P4VP Nanodomains Self-Assembled within a Poly(styrene-*b*-4-vinylpyridine) Diblock Copolymer Thin Film

Scheme 5-1 Fabrication of a self-assembled (CdSe/P4VP)-*b*-PS thin film through the selective incorporation of dispersed pre-synthesized CdSe NRs into P4VP nanodomains102

Table 5-1 Electron barrier heights (ϕ_e), electron mobilities (μ_0), and field coefficients (E_0) for in-plane and out-of-plane CdSe NRs incorporated within P4VP nanodomains in a PS matrix.103



Chapter 1 Introduction

1-1 Block Copolymers

A block copolymer (BCP) can self-assemble into an ordered periodic structures with a nanometer thicknesses that depends on molecular weight, segment size, and the strength of interaction between the blocks, represented by the Flory–Huggins interaction parameter, χ .^[1-3] The periodicity thickness is in the range 10–200 nm.

The morphology depends on χ and the composition of the copolymer, parametrized as the volume fraction of one of the constituent blocks. For the simplest class of A-B diblock copolymers, the following structures are known to be stable, as confirmed by theory^[4] and experiment^[2, 5]: lamellar, hexagonal-packed cylinder, body-centred cubic, close-packed spherical (which may exhibit only liquid-like ordering) and bicontinuous cubic gyroid structures, as shown in Figure 1-1-1. For ABC triblocks, the combination of two independent composition variables (e.g. volume fraction f_A and f_B , $f_A + f_B + f_C = 1$) and three parameters (χ_{AB} , χ_{AC} and χ_{BC}) leads to a much wider range of possible morphologies shown in Figure 1-1-2. Many have been observed, although others await discovery.^[6] Theory provides guidelines for rationalizing the observed morphologies, and in the future may be used to predict structures.^[7]

1-1-1 The Structure of Block Copolymer melts, solids, and solutions

A remarkable property of block copolymers is their ability to self-assemble in the melt in to a variety of ordered structures with nanoscale periodicities. These structures can be controlled by varying the composition of the block copolymer or the segregation between blocks (via temperature or degree of polymerization). In addition to the now well-established lamellar (lam), hexagonal-packed cylinder(hex)

and body-centered cubic (BCC) micelle phase, a number of few morphologies have been discovered, which supplement the “classical structure”. The identification of a bicontinuous cubic phase of $Ia\bar{3}d$ symmetry, sometimes called the gyroid phase, is now established. Figure 1-2-1 shows the well-known structure of block copolymers in melt, solution or solid state. [8]

Melts

Two competing effects govern the thermodynamics of block copolymer melts. At high temperature, the chains are mixtures homogeneously, as in any polymer melt. As the temperature is reduced, the tendency for the blocks to segregate is enhanced, i.e. the enthalpic process of demixing is favored. However, this is necessarily accompanied by a reduction in entropy as the chain configuration becomes more constrained. The extent of segregation of the copolymer may then be expressed using the reduced parameter χ_{AB} . Here N is the copolymer degree of polymerization, reflecting the N -dependent translation and configuration entropy.

The segment–segment interaction parameter (Flory–Huggins) described the free energy cost per monomer of conducts between the A and B monomeric units and is given by: $\chi_{AB} = \left(\frac{Z}{\kappa_B T} \right) [\varepsilon_{AB} - (\varepsilon_{AA} + \varepsilon_{BB}) / 2]$, where ε_{AB} is the interaction energy per monomer units between A and B monomers and Z is the number of nearest neighbor monomers to a copolymer configuration cell. Thus, positive χ_{AB} (which is the vast majority of cases) shows repulsion between the A and B monomers, whereas a negative value signifies mixing of unlike monomers. Moreover, χ_{AB} usually varies inversely with temperature. The second parameter that strongly influences the block copolymer behavior is the total degree of polymerization N . For large N the loss of translational and configurational entropy leads to a reduction

of the A-B monomer contacts and thus to local ordering. Since the entropic and enthalpic contributions to the free energy scale as N^{-1} and N , respectively, it is the product N^2 that is of interest in the block copolymer phase state.

Solutions

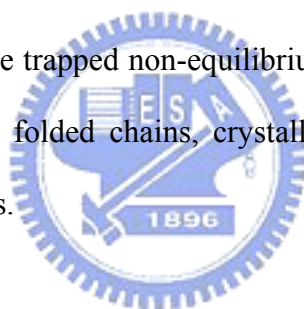
There are two basic processes that characterize the phase behavior of block copolymers in solution: micellization and gelation. Micellization occurs when block copolymer chains associate into, often spherical, micelles in dilute solution in a selective solvent. The core of the micelle is formed by the insoluble or poorly solvated block, whilst the corona contains the selectively solvated block. At a fixed temperature, micellization occurs on increasing concentration at the critical micelle concentration (CMC). The cmc is usually determined from the sharp decrease in the surface tension as a function of concentration, although other properties such as viscosity also exhibit pronounced changes.

In concentrated solutions, micelles can order into gels. Soft and hard gels are distinguished from each other and from micellar solutions by their flow properties, gels being characterized by a finite yield stress. The hard gels seem to be associated with the formation of cubic phases of spherical micelles, whereas soft gels are usually lamellar or hexagonal-packed rod micellar phase. The phase behavior of these materials has only recently begun to be elucidated using small angle scattering. It promises to be even richer than that of block copolymer melts, at least if results for analogous conventional surfactants are any guide. The flow behavior of these gels is the basis for many of their applications, and study of the rheology and behavior under shear of these materials will enhance the fundamental understanding underpinning future developments.

Solids

The structure of block copolymer melts is usually trapped upon vitrification. The mechanism underlying the glass transition are similar to those of the constituent homopolymers. Thus there are little distinct physicals associated with the formation of solid phase by glassy block copolymers.

In contrast, crystallization of one or both components of a block copolymer is accompanied by profound structure and dynamic changes. The fundamental process in crystallization of chains in a crystallizable block copolymer is the change in block conformation, i.e. the adoption of an extended or a folded structure rather than a coiled configuration found in the melt or solution. Crystallization from the melt often leads to a distinct (usually lamellar) structure, with a different periodicity from the melt. Crystallization from solution can lead to non-lamellar crystalline structures, although these may be often be trapped non-equilibrium morphology. In addition to the formation of extended or folded chains, crystallization may also lead to gross orientational changes of chains.



1-1-2 Applications

Until recently, most industrial applications of BCPs were as adhesives or for their mechanical properties (e.g. as thermoplastic elastomers). Only in the past 10 years have researchers taken BCPs into the “high-technology” area, to the so-called “nanotechnologies”. Many attempts have been made to utilize BCPs in nanotechnology. Self assembled BCP microstructures with 10 to 100 nm dimensions are useful as nanometer scale membranes, templates for fabrication of nano-objects such as metal, ceramic nanodots and wires, as 1-, 2- and 3D photonic crystals, and as nanopattern masks for fabrication of high density information storage media. The majority of applications proposed to date rely on the use of thin film structures and this is a major focus of the current review, although bulk nanoporous materials and photonic crystals are considered. The applications of various BCP

enabled nanotechnologies are summarized in Figure 1-3-1.^[9]

Nanolithography

Nanosizes greater than 150 nm can be routinely produced by photolithography techniques. The minimum size that can be achieved by photolithography is determined by the wavelength of light used in the exposure. Electron beam lithography is commonly used to access feature sizes between 150 nm and 30 nm. However, sizes less than 30 nm are not easily obtained by standard lithography. One way to overcome this problem is by using self-assembled block copolymers.

In a pioneering paper, Park *et al*^[10] demonstrated the use of block copolymer films as masks to transfer dot and stripe patterns into semiconductors. The feature density of holes achieved was $\sim 10^{11} \text{ cm}^{-2}$. The method they developed relies on the selective ozonation of polyisoprene (PI) or polybutadiene (PB) in block copolymers with polystyrene (PS) as the other, majority, component. Ozone cleaves the double bonds in the unsaturated polymers, so that they can be etched away. This process leaves holes or stripes in a PS matrix. This pattern was transferred from the block copolymer into silicon nitride by RIE using CF₄ or CF₄/O₂ gases. The quality of pattern transfer is excellent, producing nanoscale arrays of pits or channels. Park *et al* also discuss how to prepare a nanoscale array of posts by use of an “inverse” mask to that used to produce the array of pits. If the PI is fixed by staining with osmium tetroxide, then etching of the matrix will occur preferentially. The regions under the PI domains will be left as an array of posts. Details of the ozone etching method of preparing block copolymer film masks were elaborated on in a subsequent paper,^[11] which also contains data illustrating pattern transfer into other semiconductors, including silicon and germanium. A patent was awarded for this technology in 1999.^[12] In a further extension of the technique, it has been demonstrated that arrays of nano-sized metal posts can be fabricated, by an extension of the preceding method,

illustrated in figure 1-3-2.^[13] A lithographic procedure in which the ozone etching step can be omitted has also been demonstrated.^[14] Here the reactive ion etch rate is sufficiently different between the two blocks in a PS-*b*-PFS (PFS = polyferrocenyldimethylsilane) diblock, for selective etching of PS to occur directly. The application again was the development of a self-assembly route to produce a high-density magnetic storage medium (in this case cobalt nanodots). O₂ RIE leaves PFS spheres, the pattern then being transferred into silicon oxide (which improves pattern transfer) then into tungsten by RIE. The multiplayer structure is necessary because magnetic materials, such as cobalt, nickel and iron are not amenable to RIE. In the next step, the polymer and silica are removed. Finally, the pattern is transferred from the tungsten hard mask into the magnetic cobalt layer using ion-beam etching. The result is the array of cobalt nanoposts illustrated in figure 1-3-3.

Ultrahigh-density metal nanocolumn arrays can be fabricated using block copolymer templates. Russell *et al*^[15] oriented the poly(methylmethacrylate) (PMMA) cylinders in a PS-*b*-PMMA diblock by applying an electric field across the polymer film (Figure 1-3-4(a)). The PMMA was then degraded by deep UV radiation, which simultaneously cross-links the PS. The degraded PMMA was removed by acid rinsing. The resulting array of nanopores (Figure 1-3-4(b)) was subsequently filled with cobalt by electrodeposition from a methanol solution. Due to the size of the nanowires, single magnetic domain behaviour was anticipated, with obvious potential in patterned magnetic storage media (Figure 1-3-4(c)). The magnetic behavior was also highly anisotropic, with a much larger coercivity field parallel to the wire. The application of the approach to the fabrication of nanoelectrode arrays has also been reported.^[16] Russell and coworkers have also used porous PS films, formed from PS-*b*-PMMA precursors, as masks for pattern transfer (by RIE) into FeF₂/Fe bilayers to create magnetic nanostructures.^[17]

Nanoparticle Templates

BCPs have also been utilized not only as surfactants to inhibit coalescence and aid in dispersion of nanoscale particles such as metal, metal oxide, inorganics, molecular chromophores and quantum dots but also to spatially pattern the particles.

In previous works of our group, we reported a morphological transformation of PS-*b*-P4VP (P4VP = poly(4-vinylpyridine)) from a hexagonally packed cylinder structure to a lamellar structure, which occurred upon sequestering CdS nanoparticles in the P4VP block.^[18] The surface of the CdS nanoparticles was stabilized with mercaptoacetic acid as a surfactant, which renders each CdS nanoparticle hydrophilic. Thus, CdS nanoparticles segregated selectively into the P4VP domains due to the dipole-dipole interactions between the carboxylic acid on the CdS surface and the P4VP chains. Whereas pure PS-*b*-P4VP showed a hexagonally packed cylindrical structure, the composite transformed into a lamellar structure in the presence of 7 wt% CdS nanoparticles (Figure 1-3-5). The morphological transformation from the cylindrical to lamellar structure was mediated by strong interaction forces such as hydrogen bonds between carboxylic acid units of the CdS nanoparticles and the P4VP chains. In another paper,^[19] ordered clusters of surfactant-modified TiO₂ nanoparticles in the selective block of lamellar assemblies of the diblock copolymer PS-*b*-PMMA have been reported (Figure 1-3-6). Instead of using an water or alcohol phase, the TiCl₄ or tetra(isopropoxide) (TTIP) precursors were used to synthesize the TiO₂ nanoparticles in tetrahydrofuran (THF), which is a good solvent, for block copolymers. Cetyl trimethyl ammonium chloride (TMAC) amphiphilics or 3-(methacryloyloxypropyl)-trimethoxy silane (TMS) surfactant was used to modify the TiO₂ nanoparticles. To our knowledge, this presents a new approach to selectively disperse quantum-confined nanoparticle clusters in a PS-*b*-PMMA diblock copolymer with an ordered lamellar phase. 3-D and 2-D nanostructure of CdS

clusters by dispersing pre-synthesized CdS nanoparticles, containing hydroxyl groups on surface, in the PEO block selectively of polystyrene-*b*-poly(ethylene oxide) (SEO) block copolymers as template in the bulk form and thin films were reported. [20-24] Russell [25] et al. reported that mixtures of diblock copolymers and either cadmium selenide- or ferritin-based nanoparticles exhibit cooperative, coupled self-assembly on the nanoscale. In thin films, the copolymers assemble into cylindrical domains, which dictate the spatial distribution of the nanoparticles; segregation of the particles to the interfaces mediates interfacial interactions and orients the copolymer domains normal to the surface, even when one of the blocks is strongly attracted to the substrate. Organization of both the polymeric and particulate entities is thus achieved without the use of external fields opening a simple and general route for fabrication of nanostructured materials with hierarchical order (Figure 1-3-7). Thomas et al. [26] have identified that the localization of particles along the interface or at the center of the respective polymer domain was also affected by the particle-core sizes. In the system consisting of a symmetric PS-*b*-PEP (PEP = poly(ethylene propylene)), large silica nanoparticles ($d = 21.5$ nm; $d/L \sim 0.26$, where d is the particle diameter and L is the respective domain dimension of the block copolymer) were located at the center of the PEP domain. The smaller gold nanoparticles ($d = 3.5$ nm, $d/L \sim 0.06$) segregated at the interface between two block phases (Figure 1-3-8) in accordance with theoretical simulations. [26] Interfacial segregation of nanoparticles is expected to occur for particle sizes with $d/L < 0.2$, whereas localization of nanoparticles at the center of the lamellae phase is expected for $d/L > 0.3$. Figure 1-3-9a shows a cross-sectional TEM image of 100% PS thiol-coated gold nanoparticles dispersed on symmetric PS-*b*-P2VP block copolymer. [27] PS-coated gold nanoparticles are located near the center of the PS block phase of the lamellae structure, whereas poly(2-vinylpyridine) (P2VP)-coated gold

nanoparticles were located in the P2VP domain as expected. Particles coated with a similar homopolymer can lower their enthalpy by segregating into the corresponding domain of the block copolymer. Positioning the particle near the center of the corresponding polymer domain leads to a better embedding of the NP since the polymer chains can accommodate particles by moving apart rather than by stretching. Particles coated with a mixture of PS and P2VP thiols are exactly localized at the interface between the PS and P2VP block phases (Figure 1-3-9b).

Nanoreactors for nanostructure production

Block copolymer domains can be used as ‘nanoreactors’ for the synthesis of inorganic nanoparticles. Reviews of the subject are available. [28, 29] Two basic approaches have been developed. The first involves the binding of inorganic species to the monomer prior to polymerization or to one of the blocks of a copolymer prior to micellization (which may be induced by the ion binding [28]). The most important approach, however, involves the loading of pre-formed micelles, whether in solution or in bulk.

Micellar nanoreactors for metallic nanoparticles based around several different block copolymers have been investigated by Bronstein and coworkers. In many cases, the ability of poly(vinylpyridine), P2VP or P4VP, to form complexes with metal salts due to the presence of an N atom is exploited. [30-31] For example, palladium clusters have been produced by reduction of $\text{Pd}(\text{CH}_3\text{COO})_2$ that coordinates to the P4VP micellar core formed by PS-*b*-P4VP diblocks in toluene. [30, 32] Other metal nanoclusters including cobalt, [33] gold, [30, 31, 32] rhodium [30] and platinum [30] have been prepared in a similar way. The catalytic hydrogenation properties of the nanoclusters have been compared. [30, 32] Bimetallic colloids have also been prepared. [30] The methods may be extended to thin films where surface interactions may be exploited to prepare highly aligned nanostructures. Sohn and

Seo ^[34] exploited strong preferential interfacial segregation of the blocks in a thin film of a PS-*b*-P4VP diblock to fabricate a multilayer stack consisting of alternating P4VP lamellae containing gold nanoparticles and nanoparticle-free PS lamellae (Figure 1-3-10). Titania nanoparticles are interesting for applications such as catalysis, water purification and UV blocking. Spatz *et al* ^[35] have shown how nanoparticles can be produced within block copolymer micelle nanoreactors. They prepared micelles from a PS-*b*-PEO (PEO = poly(ethylene oxide)) diblock in a non-polar solvent with a PS corona and a PEO core. HCl was mixed with the micelle solution to create reservoirs within the micelle cores. Titanium alkoxides were then added, the reaction with the acid and subsequent heating leading to the formation of TiO₂ particles. Individual particles and chains were both obtained. In previous works of our group, we have reported synthesis of arrayed, TiO₂ needle-like nanostructures via a PS-*b*-P4VP diblock copolymer template. ^[36] Arrayed, needle-like nanostructures of rutile phase crystal TiO₂ were grown on a Si substrate containing TiO₂ seeds prepared through a thin PS-*b*-P4VP (use unabbreviated name first) diblock copolymer template. By using TiO₂ seeds prepared from their diblock copolymer PS-*b*-P4VP template, arranged needle-like rutile TiO₂ nanostructures with variable spatial positions and densities were fabricated. The distance between two TiO₂ needle bunches could be controlled using block copolymer templates with different molecular weights (120nm and 160 nm) (Figure 1-3-11).

Photonic Crystals

Photonic crystals are attracting immense attention since they can be used to control and confine light. Materials with a complete bandgap reflect light (incident in any direction) within the wavelength range of the gap. Block copolymers are interesting materials with which to construct photonic crystals because they can self-assemble into periodic structures in one, two and three dimensions. The

inherently low dielectric contrast between the polymeric domains can be overcome by selective doping and/or removal of one component. Another prime constraint is the requirement for telecommunications applications of a domain size of about 250 nm (to control near-IR radiation with a wavelength of 1.55 μm).^[37] Additionally, long-range order of the materials must be achieved. Much of the current research comes from the Thomas group, and they have provided a good review of material requirements and possibilities, as well as research up to year 2000,^[37] this is also being complemented by an earlier overview.^[38]

Theory has been used to predict the possibility of photonic bandgaps in single and double network bicontinuous cubic structures.^[39] However, the calculations indicated that (for the parameter space explored) no complete bandgaps exist for bicontinuous double primitive, double gyroid (body-centred cubic) or double diamond (face-centred cubic) structures. However, bandgaps are anticipated for the single network analogues, the best candidate being a single diamond structure with a dielectric contrast as low as 3.6. The optical reflectivity characteristics of an experimentally realized large domain double gyroid structure were subsequently assessed.^[40] The initial material was a PS-*b*-PI diblock with high molar mass leading to a cubic lattice parameter $a = 258$ nm. The optical properties were measured for a bulk film, and also for sample in which the PI block was removed by UV/ozone treatment (Figure 1-3-12), creating an interpenetrating PS network structure. As anticipated by theory, a complete bandgap was not observed, although a wavelength range with high reflectivity was identified. This was shifted to lower wavelength in the etched structure. A fruitful way to enhance the dielectric contrast in such an etched bicontinuous structure may be to coat the nanochannels with metal. Electroless deposition of nickel (using suitable activators) onto PS channels formed

by etching the PI in a bicontinuous PS-*b*-PI morphology (with PS homopolymer) has been carried out successfully. ^[41]

1-2 Nanostructured Materials

Colloidal nanocrystals are sometimes referred to as “artificial atoms” because the density of their electronic states — which controls many physical properties — can be widely and easily tuned by adjusting the crystal’s composition, size and shape. The combination of size- and shape-dependent physical properties and ease of fabrication and processing makes nanocrystals promising building blocks for materials with designed functions. ^[42,43] But the ability to control the uniformity of the size, shape, composition, crystal structure and surface properties of the nanocrystals is not only of technological interest: access to defined nanoscale structures is essential for uncovering their intrinsic properties unaffected by sample heterogeneity. Rigorous understanding of the properties of individual nanocrystals will enable us to exploit them, making it possible to design and build novel electronic, magnetic and photonic devices and other functional materials based on these nanostructures. Figure 1-4-1 shows variation of states of electrons with increase the quantization dimension in quantum structure.

1-2-1 Semiconductor Nanoparticles

Characteristics of Semiconductor Nanoparticles

Semiconductor nanoparticles have an inorganic core that is stabilized by a layer of surface surfactants. Nanoparticles with a semiconductor as the inorganic material — so-called quantum dots — exhibit size-tunable band gaps. Shape control of such colloidally prepared nanostructures has been recently achieved by modifying the synthesis to obtain rod shaped particles—nanorods.

Quantum dots have two obvious characteristics. One is the *surface area effect* and the other is *quantum confinement effect*. In surface area effect, for particles in such a small size regime, a large percentage of the atom is on or near the surface, for example, 99% of the atoms are on the surface for a 1nm size particles.^[44] The existence of this vast interface between the nanoparticles and the surrounding medium can have a profound effect on the particles properties. The imperfect surface of the nanoparticles may act as electron and/or hole traps upon optical excitation. Thus the presence of these trapped electrons and holes can in turn modify the optical properties of the particles. In quantum confinement effect, “confinement” and “quantization” are two closely related definition: If a particles is “confined” then its energy is “quantized”, and vice versa. According to the dictionary, to “confine” mean to “restrict within limits” to “enclose”, and even to “imprison”. The quantum confinement not only causes the increase of the energy gap (blue shift of the absorption edge) and the splitting of the electronic states, but also changes the densities of state and the exciton oscillator strength.^[45] It was revealed that many of the differences between the electronic behaviors of the bulk and the quantum-confined low-dimensional semiconductors are due to their difference densities of state.

Nanorods exhibit electronic and optical properties that differ from quantum dots. For example, unlike the spherical dots, nanorods demonstrate linearly *polarized emission*^[46, 47] leading also to polarized lasing.^[48] In addition to size and shape, *nanocrystals’ charging* may also significantly influence their electrical and optical properties. Millo et al. reported optical and tunneling spectroscopies on CdSe nanorods and correlated the experimental data with the level structure calculated using a multi-band effective-mass model for an infinite potential well.^[49] However, the experimental set-up in both optical and tunneling measurements was tuned so as to avoid nanorods charging.

Applications of CdSe Nanoparticles

In 1993, a paper entitled “Synthesis and Characterization of Nearly Monodisperse CdX (X=S, Se, Te) Semiconductor Nanoparticles” by Murray, Norris, and Bawendi appeared in the Journal of the American Chemical Society.^[50] CdSe nanoparticles are (potential) building blocks for new electronic and optical nanodevices such as light-emitting diodes, solar cells, lasers, and biological labels.

Light-emitting diodes Alivisatos et al. reported improved efficiencies in light emitting diodes made with CdSe (CdS) core/shell type nanoparticles and a semiconducting polymer.^[51] They reported experiments on bilayer light emitting diodes made with organically capped CdSe(CdS) core/shell type semiconductor nanoparticles and an electroluminescent (EL) semiconducting polymer poly(*p*-phenylenevinylene) (PPV). The devices emit from red to green with external quantum efficiencies of up to 0.22% at brightnesses of 600 cd/m² and current densities of 1 A/cm². They have operating voltages as low as 4 V and lifetimes under constant current flow of hundreds of hours. Most of these numbers are significant improvements over similar devices made with CdSe nanoparticles. The devices show either nanoparticle-only EL or a combination of nanoparticle and PPV EL, depending on nanoparticle layer thickness. The nanoparticle EL is dependent on nanoparticle size. Some devices show a voltage dependent spectral output. The spectral output is consistent with a field dependent electron range in the nanoparticle layer limited by carrier trapping (Figure 1-4-2).

Solar cells Alivisatos et al. reported hybrid CdSe nanorods-conjugated polymer solar cells.^[52] They demonstrated that semiconductor nanorods can be used to fabricate readily processed and efficient hybrid solar cells together with polymers. By controlling nanorod length, we can change the distance on which electrons are transported directly through the thin film device. Tuning the band gap by altering

the nanorod radius enabled us to optimize the overlap between the absorption spectrum of the cell and the solar emission spectrum. A photovoltaic device consisting of 7-nanometer by 60-nanometer CdSe nanorods and the conjugated polymer poly-3(hexylthiophene) was assembled from solution with an external quantum efficiency of over 54% and a monochromatic power conversion efficiency of 6.9% under 0.1 milliwatt per square centimeter illumination at 515 nanometers. Under Air Mass (A.M.) 1.5 Global solar conditions, we obtained a power conversion efficiency of 1.7% (Figure 1-4-3).

Lasers Bawendi et al. reported optical gain and stimulated emission in semiconductor nanoparticles.^[53] The development of optical gain in chemically synthesized semiconductor nanoparticles has been intensely studied as the first step toward semiconductor nanoparticles lasers. They examined the competing dynamical processes involved in optical amplification and lasing in semiconductor nanoparticles and found that, despite a highly efficient intrinsic nonradiative Auger recombination, large optical gain can be developed at the wavelength of the emitting transition for close-packed solids of these nanoparticles. Narrowband stimulated emission with a pronounced gain threshold at wavelengths tunable with the size of the semiconductor nanoparticle was observed, as expected from quantum confinement effects. These results unambiguously demonstrate the feasibility of nanocrystal quantum dot lasers.

Biological labels Alivisatos et al. reported semiconductor nanoparticles as fluorescent biological labels.^[54] Semiconductor nanoparticles were prepared for use as fluorescent probes in biological staining and diagnostics. Compared with conventional fluorophores, the nanoparticles have a narrow, tunable, symmetric emission spectrum and are photochemically stable. The advantages of the broad, continuous excitation spectrum were demonstrated in a dual-emission,

single-excitation labeling experiment on mouse fibroblasts. These nanoparticle probes are thus complementary and in some cases may be superior to existing fluorophores.

1-2-2 Metal Nanoparticles

Characteristics of Metal Nanoparticles

Physicists predicted that metal nanoparticles in the diameter range 1-10 nm (intermediate between the size of small molecules and that of bulk metal) would display electronic structures, reflecting the electronic band structure of the nanoparticles, owing to quantum-mechanical rules.^[55] The resulting physical properties are neither those of bulk metal nor those of molecular compounds, but they strongly depend on the particle size, interparticle distance, nature of the protecting organic shell, and shape of the nanoparticles.^[56] The few “last metallic electrons” are used for tunneling processes between neighboring particles, an effect that can be detected by impedance measurements that distinguish intra- and intermolecular processes.

The *quantum size effect* is involved when the de Broglie wavelength of the valence electrons is of the same order as the size of the particle itself. Then, the particles behave electronically as zero-dimensional quantum dots (or quantum boxes) relevant to quantum-mechanical rules. Freely mobile electrons are trapped in such metal boxes and show a characteristic collective oscillation frequency of the plasma resonance, giving rise to the so-called plasmon resonance band (PRB) observed near 530 nm in the 5-20-nm-diameter range. In nanoparticles, there is a gap between the valence band and the conduction band, unlike in bulk metals. The size induced metal-insulator transition, described in 1988, is observed if the metal particle is small enough (about 20 nm) that size-dependent quantization effects occur. Then, standing electron waves with discrete energy levels are formed. *Single-electron*

transitions occur between a tip and a nanoparticle, causing the observation of so-called Coulomb blockades if the electrostatic energy, $E_a = e^2/2C$, is larger than the thermal energy, $E_T = kT$. The capacitance C becomes smaller with smaller particles. This means that single-electron transitions can be observed at a given temperature only if C is very small, i.e., for nanoparticles since they are small enough ($C < 10^{-18}$ F). Large variations of electrical and optical properties are observed when the energy level spacing exceeds the temperature, and this flexibility is of great practical interest for applications (transistors, switches, electrometers, oscillators, biosensors, catalysis).
[57]

Applications of Au Nanoparticles

Au nanoparticles are the most stable metal nanoparticles, and they present fascinating aspects such as their assembly of multiple types involving materials science, the behavior of the individual particles, size-related electronic, magnetic and optical properties (quantum size effect), and their applications to catalysis and biology. Their promises are in these fields as well as in the bottom-up approach of nanotechnology, and they will be key materials and building block in the 21st century.

Memory cells Yang et al. reported electric-field-induced charge transfer between Au nanoparticles and capping 2-naphthalenethiol and organic memory cells. [58] An electrical transition, induced by a high electric field, was observed in a device consisting of a polystyrene film containing 2-naphthalenethiol-capped Au nanoparticles sandwiched between two Al electrodes. The current through the device changed from a charge-injection-controlled current to a space-charge-limited current. The latter current is higher than the former by more than three orders of magnitude at 2 V. Asymmetrical current-voltage curve was observed along the two polarity directions for the device after the transition. This transition is attributed to an electric-field-induced charge transfer between the Au nanoparticle and the capping

2-naphthalenethiol. The device exhibits good stability in the high conductivity state, so it can be used as a write-once-read-many times (Figure 1-4-4).

Single-electron transistors Simon reported single electron tunneling in Au nanoparticle arrangements.^[59] Coulomb charging of chemically prepared nanoparticles has already been utilized to build up “single electron tunneling” (SET) transistors. Sato et al.^[60] reported the electrical characteristics of a SET transistor, where single 1,6-hexanedithiol-stabilized 10 nm Au nanoparticles were attached by self-assembly to 3-(2-aminoethylamino) propyltrimethoxysilane-functionalized metal electrodes, fabricated by electron beam lithography (Figure 1-4-5). Since not all steps of this procedure could be controlled in detail, the number of nanoparticles in the chain bridging the 30 nm gap between electrodes differed from device to device. Up to 77 K conduction was dominated by single electron charging. The capacitance of all junctions in the chain turned out to be $1.8\text{-}2 \times 10^{-18}$ F and the Coulomb gap calculated from this value was in reasonable agreement with the value of 150 mV obtained from the I (U) characteristics. The latter was systematically squeezed, when a gate voltage of -0.4 to 0.4 V was applied, which reflects the desired function of the single electron transistor.

Biological sensors The two groups of Mirkin-Letsinger at Northwestern^[61] and Alivisatos-Schultz at Berkeley^[62] have pioneered strategies for the organization of functionalization of Au nanoparticles with oligonucleotides. The former group used DNA as a linker to form macroscopic assemblies consisting in discrete 13-nm-diameter particles. The DNA attached to the nanoparticles retained its ability to hybridize with complementary DNA, and the annealing process was thermally reversible and nondestructive. The reaction was sequence-specific (Figure 1-4-6a). The latter group used DNA as a template to prepare nanocrystal molecules consisting of two or three 1.4-nm-diameter particles on a single oligonucleotide strand.

DNA-driven assemblies of Au nanoparticles have indeed attracted considerable interest, and a new colorimetric technique based on the sensitivity of the SPB to monitor DNA modification was designed by the Mirkin-Letsinger group. In this strategy, Au nanoparticles are used as building blocks, allowing the assembly of alkanethiol-capped oligonucleotides such as single-stranded DNA and complementary linker oligonucleotide (DNA) strands (Figure 1-4-6b).

Catalysts Au is very popular for being chemically inert. It is indeed one of the most stable metals in the group 8 elements, and it is resistant to oxidation. In the 1970s, however, Parravano's group reported the investigation of the activity of Au in oxygen/hydrogentransfer reactions ^[63] and the reduction of NO by dihydrogen, but these studies remained isolated. Therefore, the discovery by Haruta et al., reported in 1989, that Au nanoparticles supported on Co_3O_4 , Fe_2O_3 , or TiO_2 were highly active catalysts, under high dispersion, for CO and H_2 oxidation, NO reduction, water-gas shift reaction, CO_2 hydrogenation, and catalytic combustion of methanol was a surprise, and was considered important by the chemical community. Catalysis with Au nanoparticles, in particular the very active oxide-supported ones, is now an expanding area, and a large number of new catalytic systems for various reactions are now being explored.

1-2-3 Electrical Properties of Two- and Three-Dimensional Arrangements of Nanoparticles

Generally speaking, the nanoparticles thin films and similar assemblies can be classified into three categories: three-dimensional (3D), two-dimensional (2D), and one-dimensional (1D) systems. 2D and 3D nanoparticle assemblies have been made by many research groups, by using a large variety of techniques, such as solvent evaporation, Langmuir-Blodgett transfer, producing self-assembled monolayers and

multilayers, and layer-by-layer assembly. In comparison, anisotropic 1D assemblies of nanoparticles are seldom reported due to the difficulties arising with their preparation, which stem from the perception of the isotropic structure and morphology of 0D nanoparticles.

In 1993, Middleton and Wingreen reported collective transport in arrays of small metallic dots.^[64] They examine the low-temperature, non-linear charge transport in such an array. The dots are treated as capacitively coupled conductors with charges allowed to tunnel between neighboring dots. In contrast with previous work,^[65] they explicitly include the effects of random offset charges on each dot and investigate the limit where the number of dots becomes large. They find that the onset of conduction occurs at a voltage V_T proportional to the linear array size (Figure 1-4-7). This sharp onset is to be contrasted with conduction in one- and two-dimensional disordered materials, where an increasing electric field leads to a smooth increase in conductivity. One of the correlation lengths that diverges near this threshold is found from a general argument based on interface growth, while another is found by focusing on “slow points” which control the current. These correlation lengths determine the branching of current paths in the array and hence the current near onset. In particular, they predict that the current through linear and square arrays behaves as

$$I \propto \left(\frac{V}{V_T} - 1 \right)^{\zeta} \dots\dots\dots(1-1)$$

with $\zeta = 1, 5/3$ in dimensions $d=1, 2$, respectively.

Three-dimensional arrangements Brinker et al. reported self-assembly of ordered, robust, three-dimensional gold nanoparticle/silica arrays.^[66] They reported the synthesis of a new nanoparticle mesophase through self-assembly of water-soluble nanoparticle micelles with soluble silica. The mesophase comprises Au nanoparticles

arranged within a silica matrix in a face-centered cubic lattice with cell dimensions that are adjustable through control of the nanocrystal diameter and/or the alkane chain lengths of the primary alkanethiol stabilizing ligands or the surrounding secondary surfactants (Figure 1-4-8a). Under kinetically controlled silica polymerization conditions, evaporation drives self-assembly of nanoparticle micelles into ordered nanoparticle /silica thin-film mesophases during spin coating. The intermediate nanoparticle micelles are water soluble and of interest for biolabeling. Initial experiments on a metal-insulator-metal capacitor fabricated with an ordered three-dimensional Au nanoparticle /silica array as the “insulator” demonstrated collective Coulomb blockade behavior below 100 kelvin and established the current-voltage scaling relationship for a well-defined three-dimensional array of Coulomb islands (Figure 1-4-8b, c).

Two-dimensional arrangements Black et al. reported spin-dependent tunneling in self-assembled two-dimensional cobalt-nanoparticle superlattices (Figure 1-4-9a).^[67] The voltage dependence of current (for $V > V_T$) depends on the number of accessible current paths through the superlattice. In their nanoparticle devices they measure $2.2 < \alpha < 2.7$, implying an array dimensionality slightly higher than 2D and consistent with our experimental geometry. Thus, the scaling exponent confirms that all paths through the superlattice can contribute to device conductance. A plot of I versus $(V/V_T - 1)$ shows that for $V > V_T$, the current follows a power-law dependence for over three orders of magnitude (Figure 1-4-9b, c). The variation in α from device to device (~9%) is comparable to that measured for lithographically patterned arrays.

1-3 Motivation and Scope of Dissertation

Block copolymers are versatile platform materials because they can self-assemble—if they have appropriate compositions and are subjected to suitable

conditions—into various nanostructures having period thicknesses between 10 and 100 nm through microphase separation of incompatible blocks. Nanostructured block copolymers can be used as templates for selectively controlling the spatial position of nanostructured materials within one of the blocks.

Zero-dimensional nanostructures, such as quantum dots and nanoparticles, have diameters in the range of 1–10 nm are the subject of much current research interest because the optical, electronic, and chemical properties of these materials. As a result, such nanostructures are being investigated for use in various applications, including light-emitting diodes, solar cells, lasers, transistors, memory cells, biological sensors, and catalysts. In these applications, the quantum dots or nanoparticles are often capped with organic ligands or are surrounded by other dielectric materials. Thus, an understanding of the collective electron transport of quantum dots or nanoparticles dispersed in organic or dielectric materials is of both scientific and technological importance. In the present study, we prepared self-assembled thin films that consisted of CdSe quantum dots or Au nanoparticles sequestered in a poly(4-vinylpyridine) nanodomain of poly(styrene-*b*-4-vinylpyridine) diblock copolymer and investigated the collective electron transport of the structures.

Moreover, the unique optical and electrical properties of one-dimensional (1D) semiconductor nanostructures, such as nanorods and nanowires, can be exploited for use in a number of applications. To take full advantage of the material properties of these 1D nanostructures, they must be pre-aligned or ordered in some other way. Although there are many bottom-up growth techniques for preparing 1D nanostructures in the out-of-plane 2D arrays and many techniques for pre-synthesized NRs in the in-plane 2D arrays, finding techniques for arranging pre-synthesized nanorods in out-of-plane 2D arrays remains a great challenge. The powerful aligning force of an electric field can be used to manipulate the orientation of

anisotropic materials by taking advantage of their different anisotropic dielectric constants. In this thesis, we applied an electric field to induce the orientation of CdSe nanorods that had been self-assembled in the poly(4-vinylpyridine) nanodomains of a poly(styrene-*b*-4-vinylpyridine) diblock copolymer thin film.



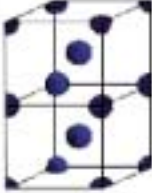
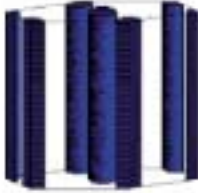
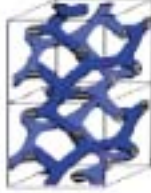


Nature of patterns	Spheres (SPH) (3D)	Cylinders (CYL) (2D)	Double gyroid (DG) (3D)	Double diamond (DD) (3D)	Lamellae (LAM) (1D)
Space group	$Im\bar{3}m$	$p6mm$	$Ia\bar{3}d$	$Pn\bar{3}m$	pm
Blue domains: A block					
Volume fraction of A block	0-21%	21-33%	33-37%	33-37%	37-50%

Figure 1-1-1 Schematic phase diagram showing the various ‘classical’ block copolymer morphologies adopted by linear diblock copolymer. ^[6]



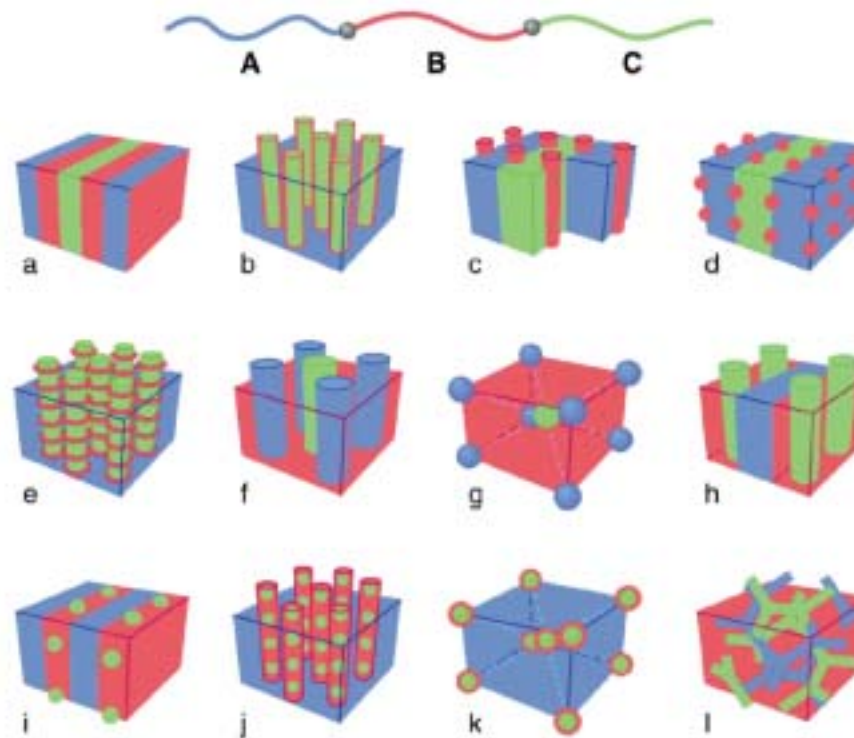


Figure 1-1-2 Schematic of morphologies for linear ABC triblock copolymer. A combination of block sequence (ABC, ACB, BAC), composition and block molecular weights provides an enormous parameter space for the creation of new morphologies. ^[6]

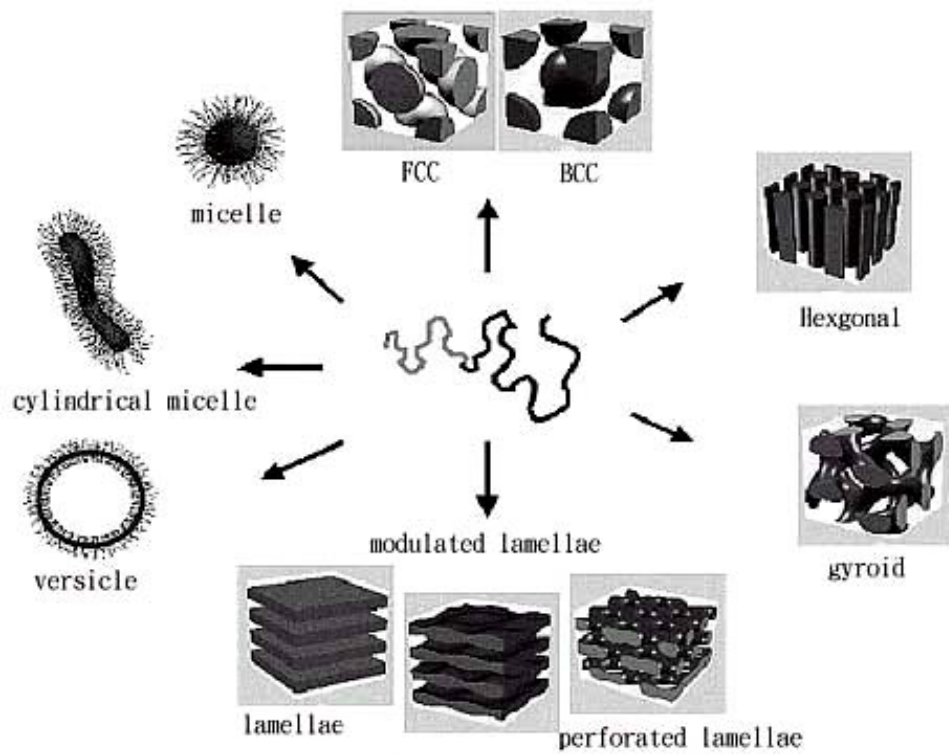
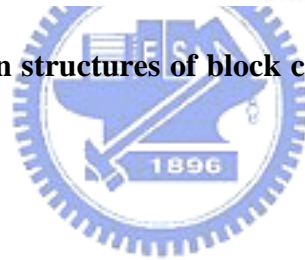


Figure 1-2-1 The well-known structures of block copolymers in melt, solution or solid state. [8]



Block Copolymer Nanotechnology

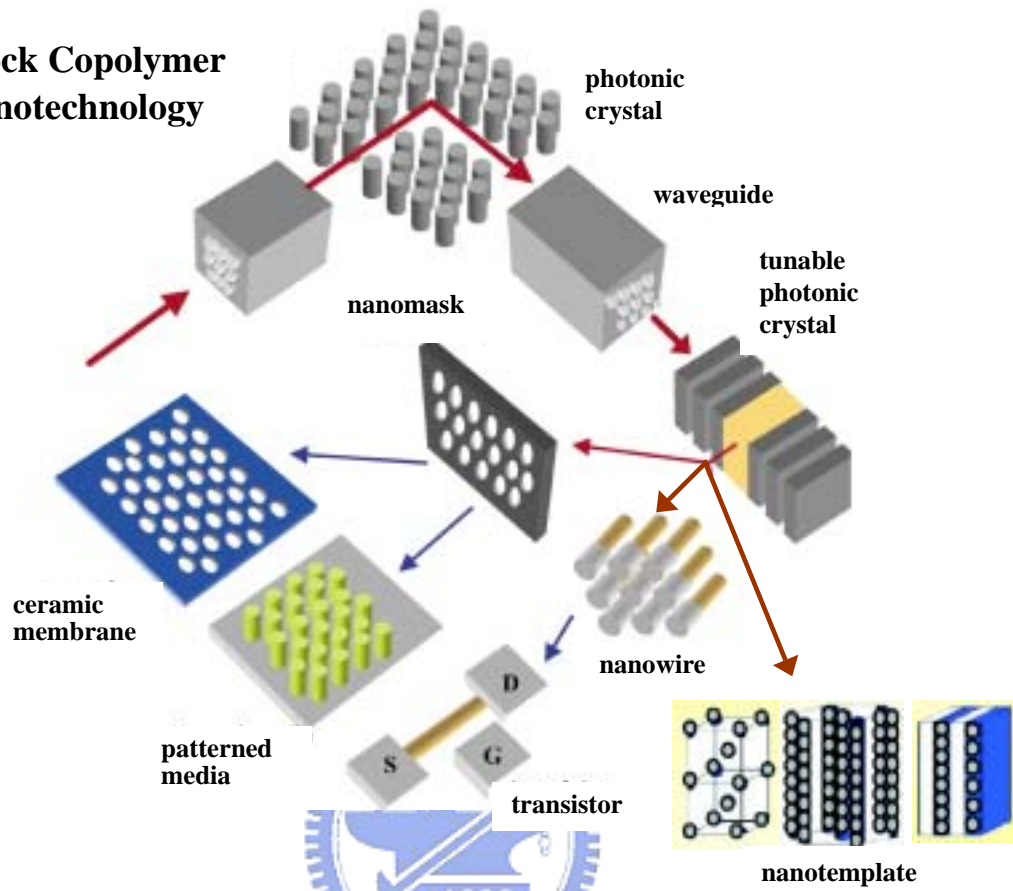


Figure 1-3-1 Schematic of various applications of block copolymers in nanotechnologies. ^[9]

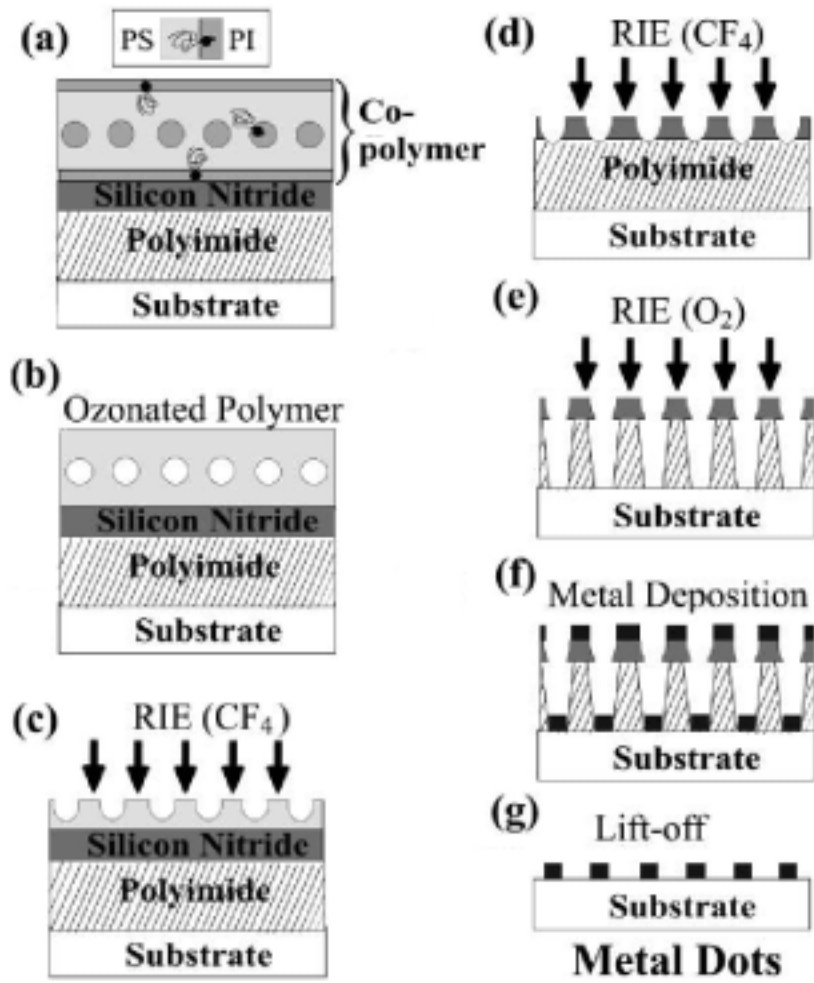


Figure 1-3-2 Schematic of the production process of a metal nanodot array using block copolymer lithography. ^[12]

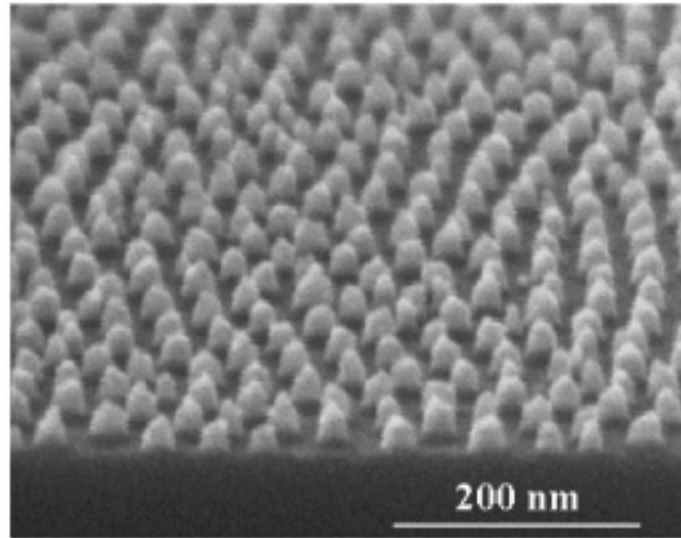


Figure 1-3-3 SEM image of polystyrene-*b*-polyferrocenyldimethylsilane mask, after the polystyrene has been removed by O₂ RIE. ^[14]



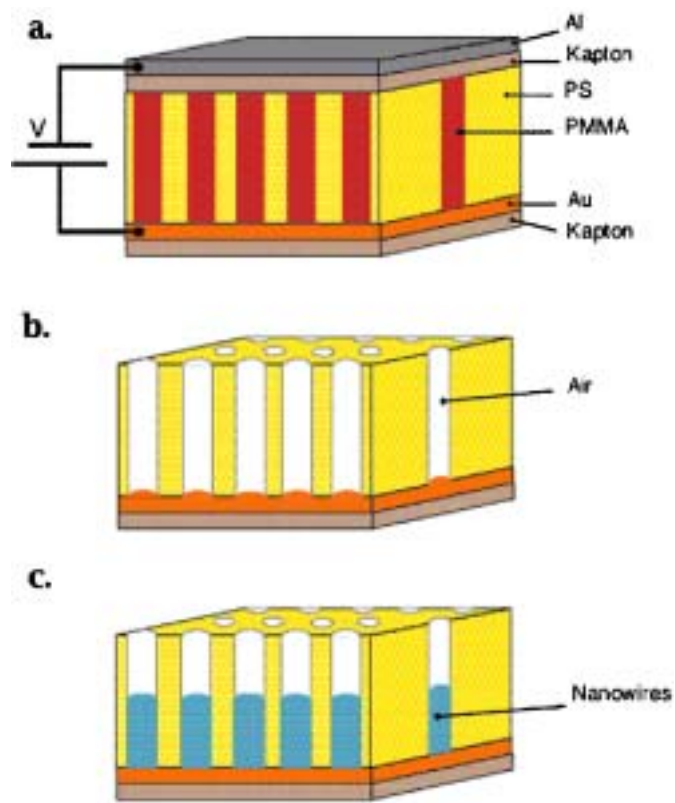


Figure 1-3-4 Schematic representation of high density nanowire fabrication in a polystyrene-*b*-poly(methylmethacrylate) matrix. ^[15]

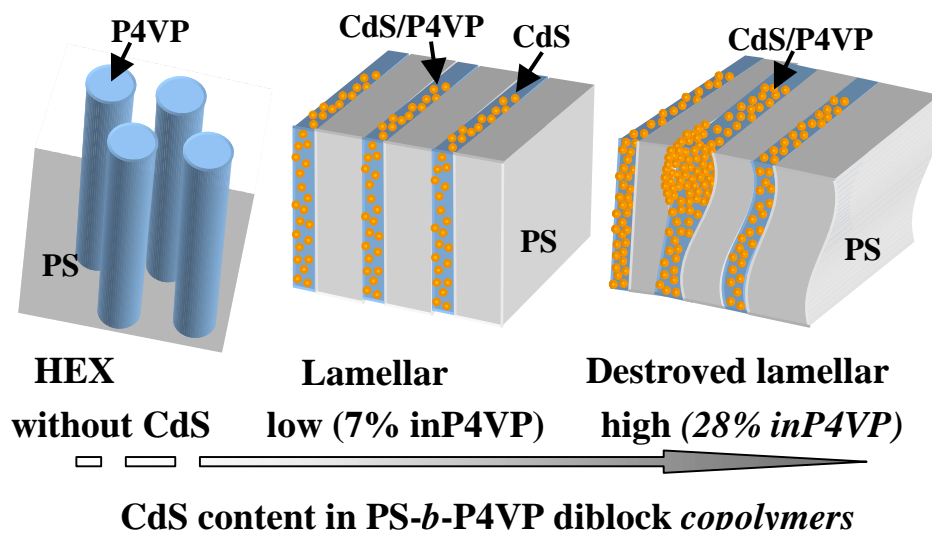


Figure 1-3-5 The morphological transformation from a hexagonally packed cylinder structure of pure polystyrene-*b*-poly(4-vinylpyridine) (PS-*b*-P4VP) diblock copolymers to lamellar (CdS/P4VP)-*b*-PS composites. ^[18]

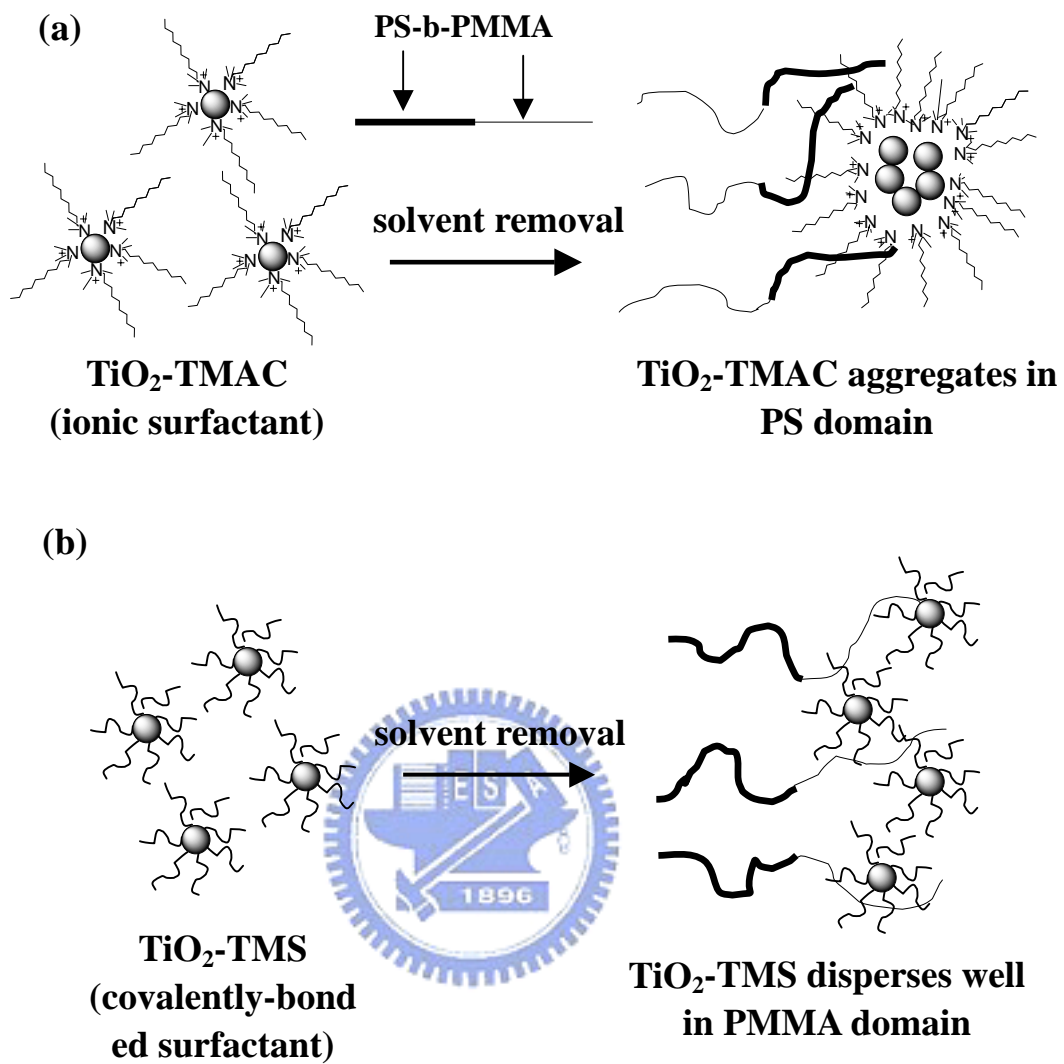


Figure 1-3-6 Schematic of selected distribution of TiO₂ nanoparticles in polystyrene-*b*-poly(methylmethacrylate) diblock copolymer.^[19]

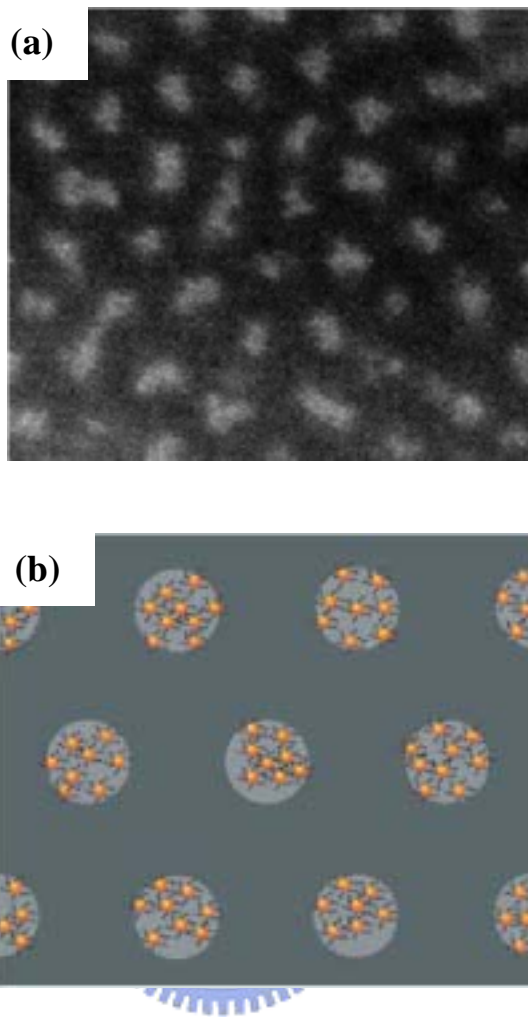


Figure 1-3-7 (a) Secondary electron SEM image of the surface of a thin film of a diblock copolymer–CdSe nanoparticle mixture spin-coated onto a silicon wafer and annealed at 170 °C for 2 days (image width, 250 nm) taken at 1-kV acceleration voltage. (b) Schematic representation of nanoparticle assembly at the poly(2-vinylpyridine) cylinders. ^[25]

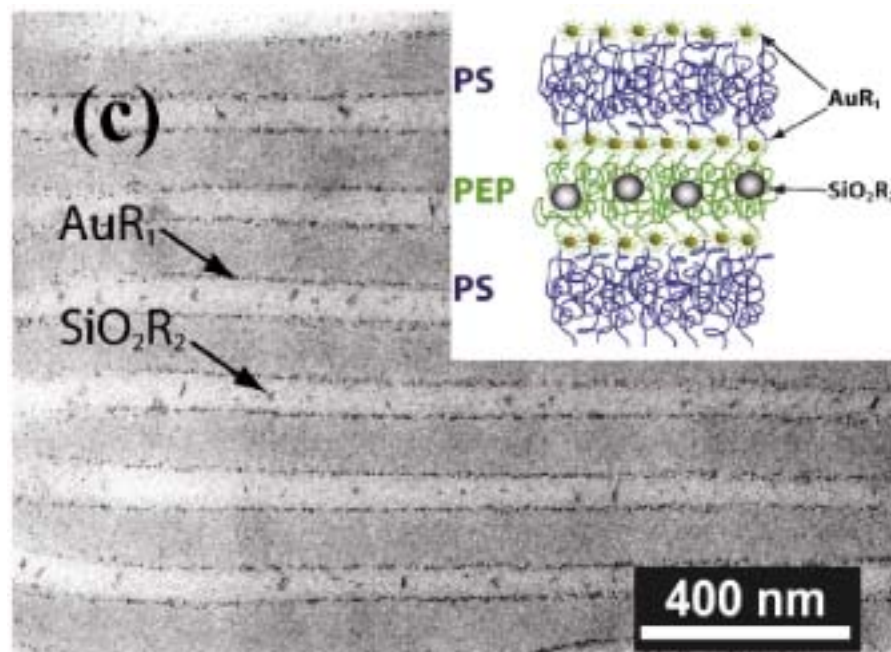


Figure 1-3-8 TEM micrograph of a ternary blend of polystyrene-*b*-poly(ethylene propylene) + AuR₁ + SiO₂R₂ with inorganic filling fraction $f = 0:02$; respectively, after micro-sectioning normal to the layer direction (no stain).^[26] (AuR₁ is Au-S-C₁₈H₃₇ and SiO₂R₂ is SiO₂-(Si(CH₃)₃)₂)

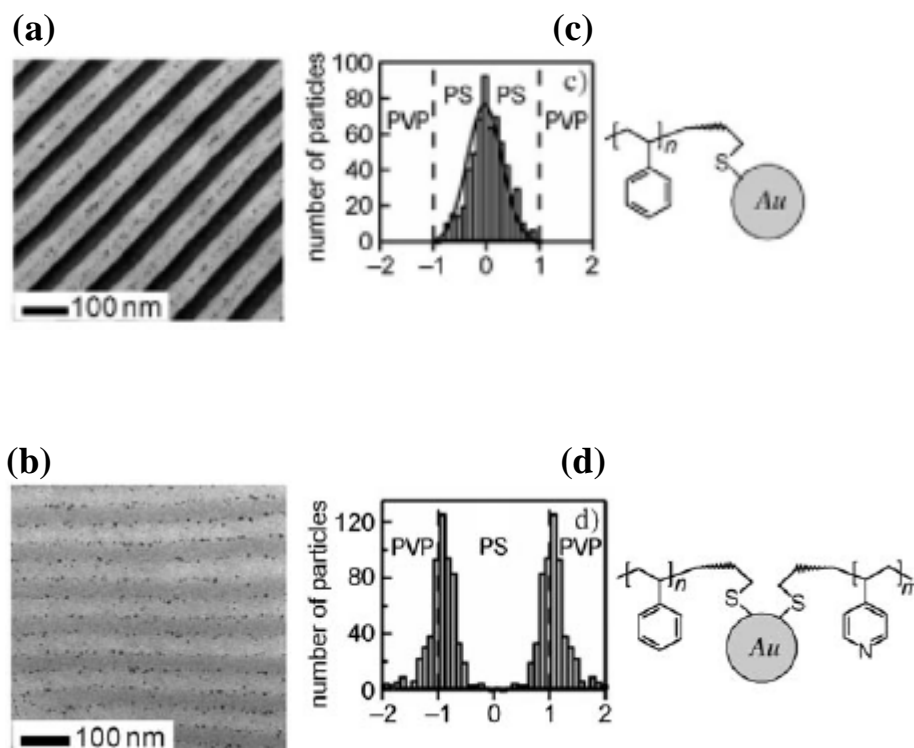


Figure 1-3-9 (a) Assembly of Au nanoparticles (core: 3.9 ± 1.0 nm; shell: polystyrene; (core+shell)=7.7 nm) into polystyrene-*b*-poly(2-vinylpyridine) diblock copolymers. (b) Assembly of Au nanoparticles (core: 3.9 ± 1.0 nm; shell: polystyrene and poly(2-vinylpyridine); (core+shell)=7.7 nm) into polystyrene-*b*-poly(2-vinylpyridine) diblock copolymers. (c), (d) The respective histograms of particle locations for the samples shown in (a) and (b). Reprinted with permission. ^[27]

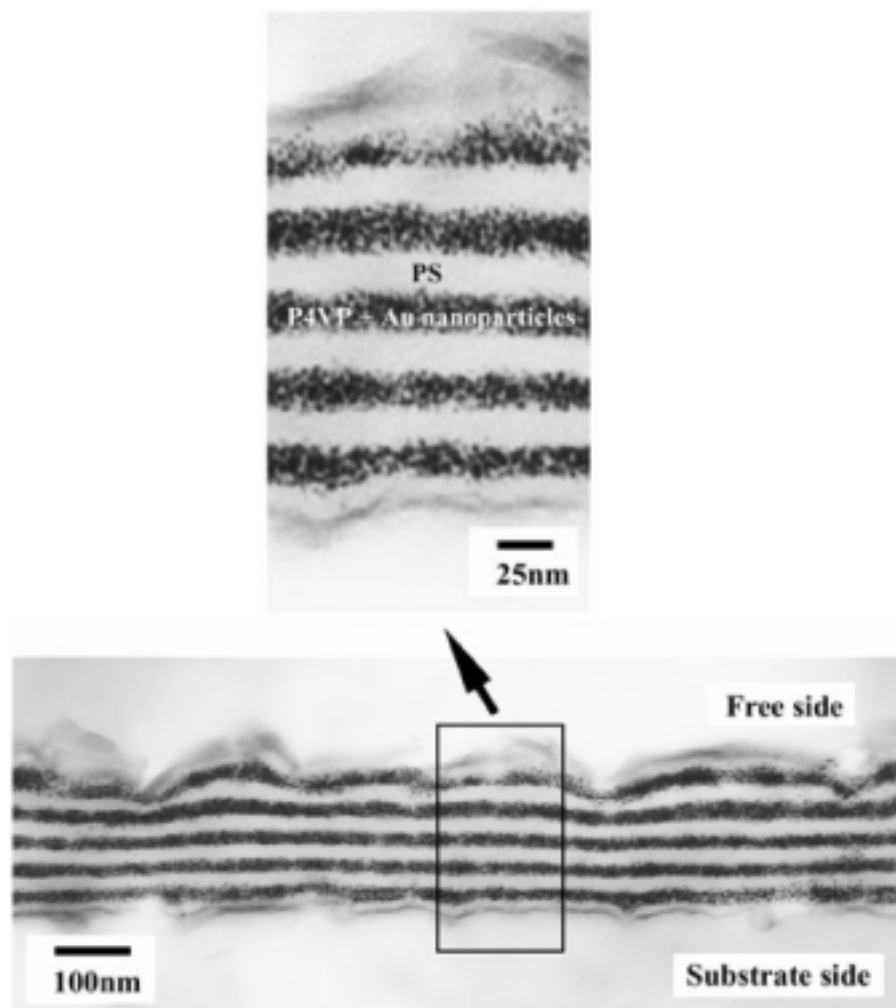


Figure 1-3-10 Cross-sectional transmission electron micrograph showing Au nanoparticles patterned within the poly(4-vinylpyridine) lamellae formed by a polystyrene-*b*-poly(4-vinylpyridine) diblock copolymer. ^[34]

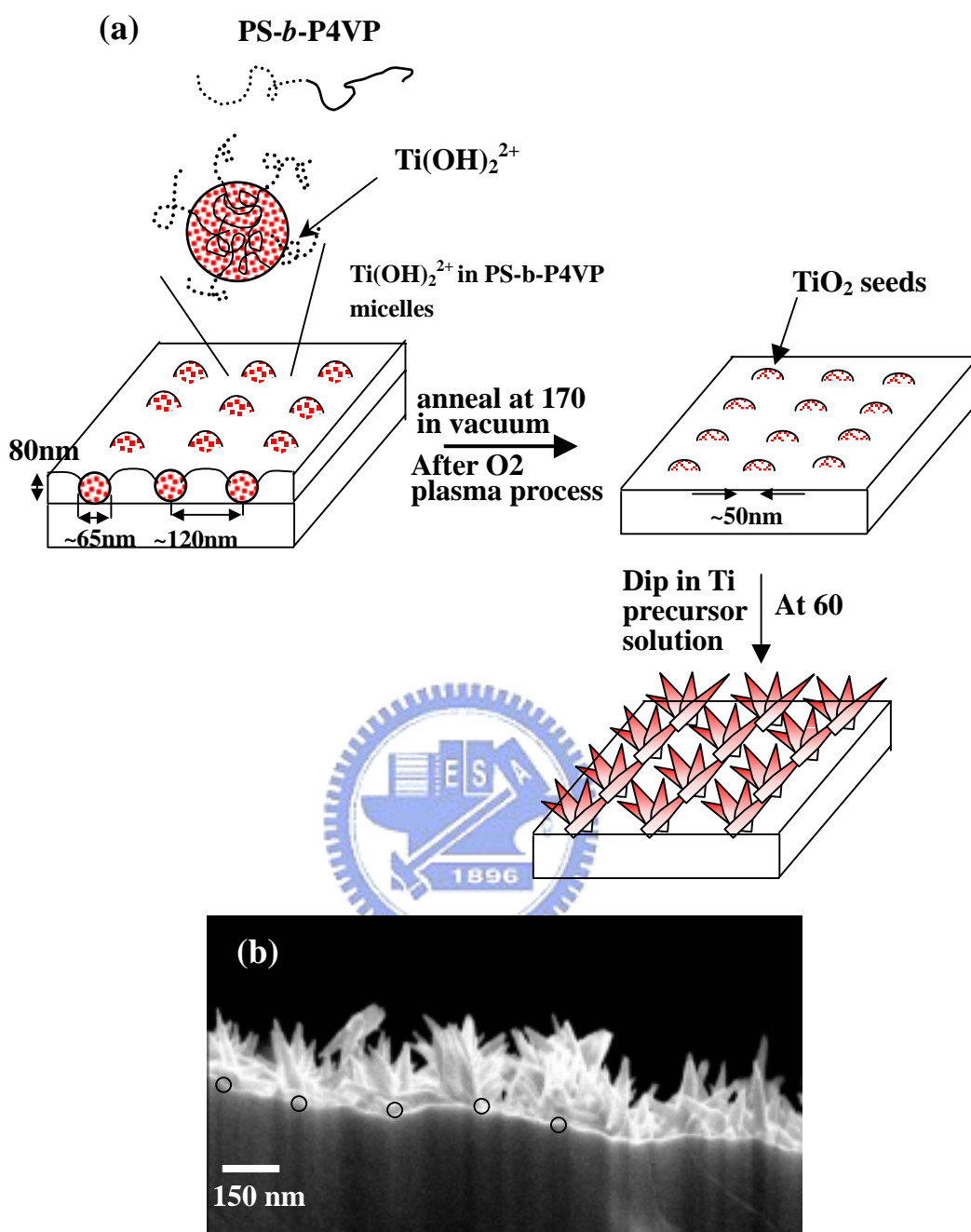


Figure 1-3-11 Schematic of synthesis of needle-like TiO₂ nanostructures with ordered patterns. ^[36]

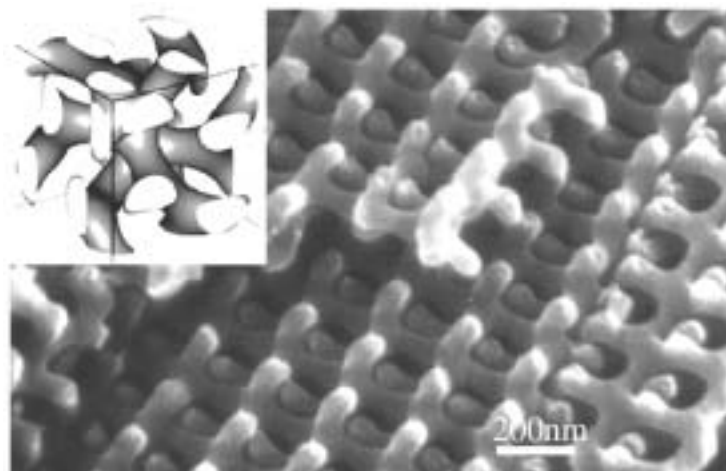


Figure 1-3-12 SEM image of an etched polystyrene-*b*-polyisoprene diblock, showing a fracture surface. The polystyrene network channels remaining after removal of polyisoprene are clearly visible. ^[39]



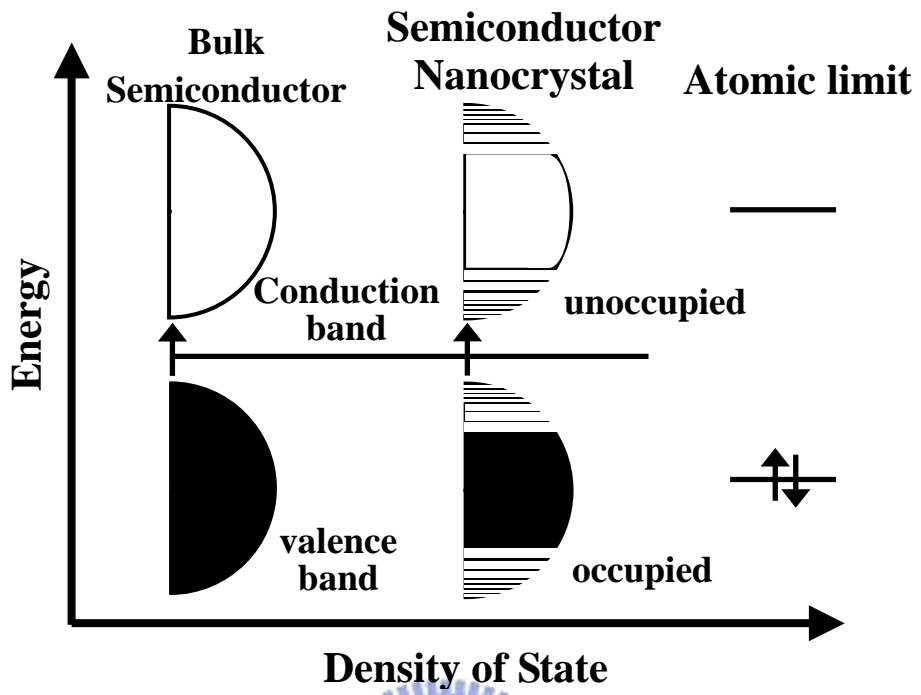


Figure 1-4-1 Schematic illustrations the density of state in semiconductor. ^[42]



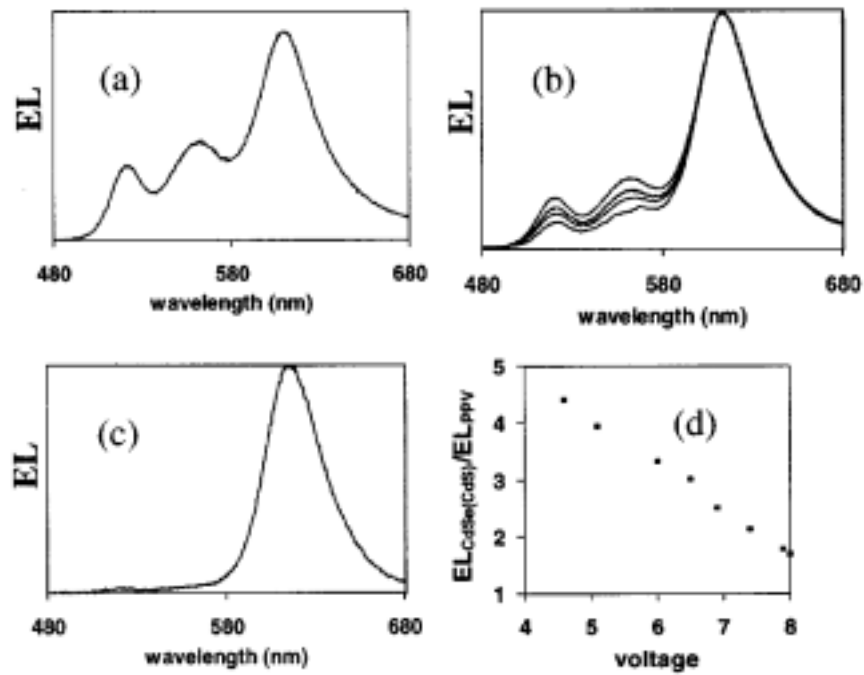


Figure 1-4-2 EL spectra collected on ITO/PPV (400 Å)/CdSe(CdS)/Mg/Ag devices having average nanocrystal layer thicknesses of 100 (a), 200 (b), and 400 Å (c). (d) Show the voltage dependence of the ratio of integrated nanocrystal EL to integrated PPV EL for the device shown in (b).^[51]

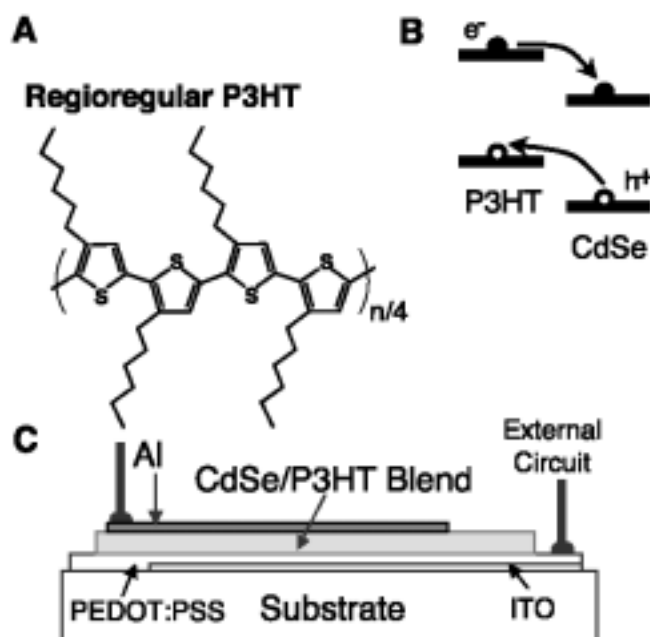


Figure 1-4-3 (a) The structure of regioregular P3HT. (b) The schematic energy level diagram for CdSe nanorods and P3HT showing the charge transfer of electrons to CdSe and holes to P3HT. (c) The device structure consists of a film ;200 nm in thickness sandwiched between an aluminum electrode and a transparent conducting electrode of PEDOT:PSS.^[52]

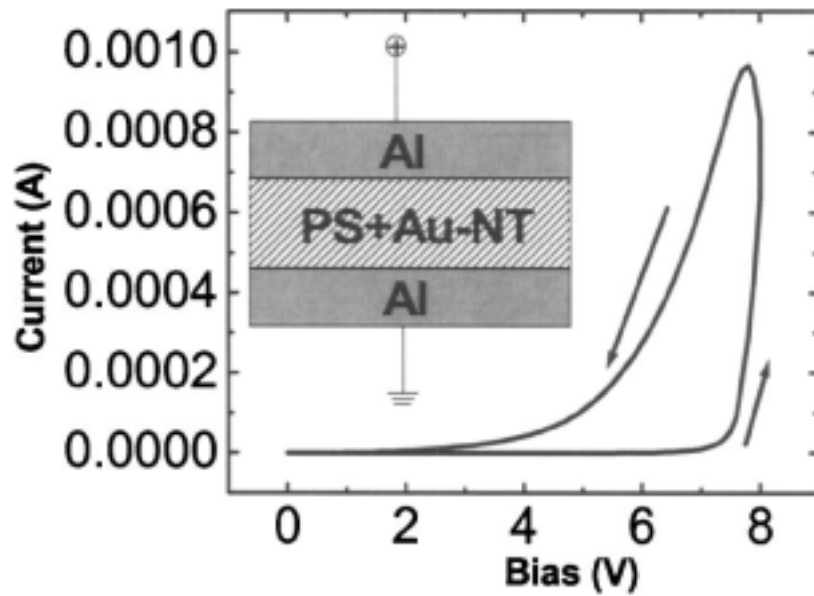


Figure 1-4-4. *I-V* curve of Al/Au-2NT NPs+PS/ Al. The arrows indicate the bias scanning directions and the inset the device structure.^[58]



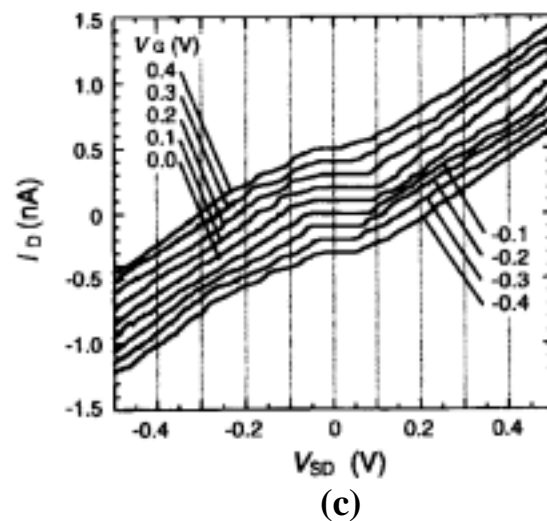
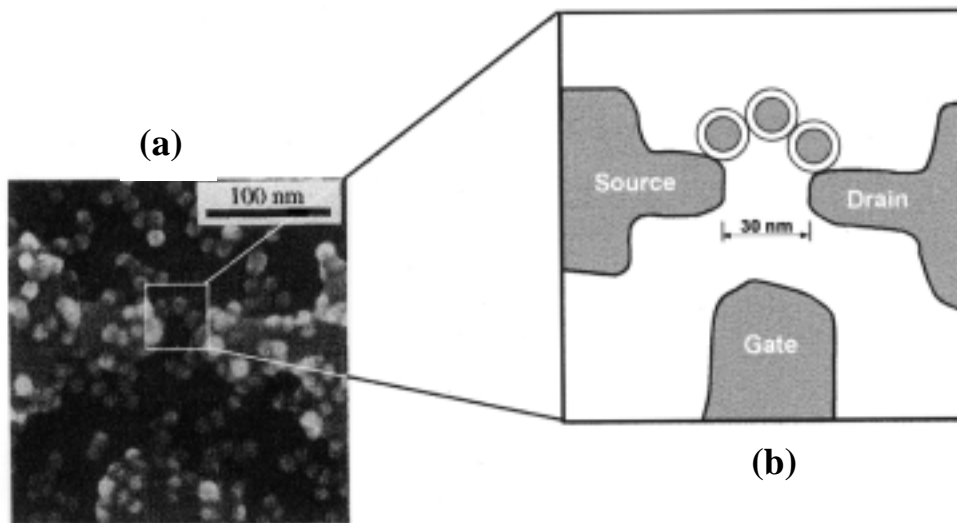


Figure 1-4-5. (a) SEM image of a chain consisting of three Au nanoparticles incorporated in a system of source, drain, and gate metal electrodes. (b) Scheme of electrode pattern defined by electron beam lithography. (c) Drain current (I_D) versus source-drain voltage (V_{SD}) characteristics of the SET transistor measured at 4.2 K with various gate voltages (V_G)^[60]

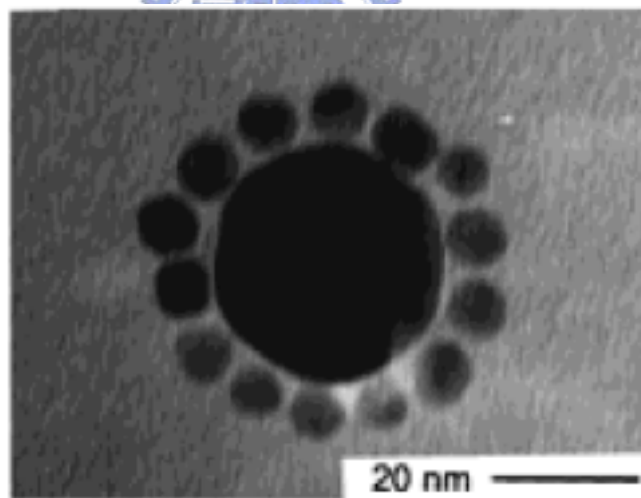
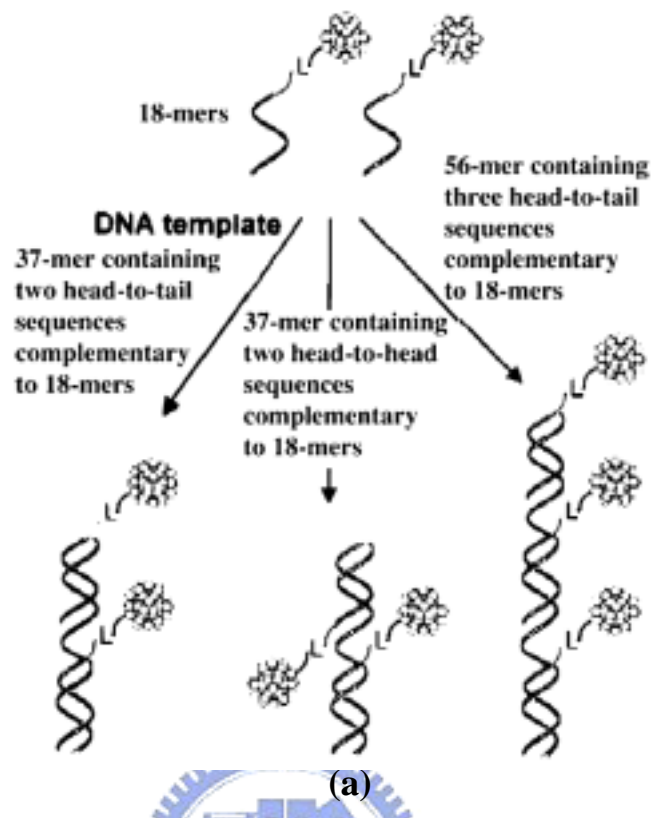


Figure 1-4-6. (a) Preparation of “nanocrystal molecules” consisting of two or three DNA modified Au nanoparticles attached to a complementary DNA template. ^[61] (b) TEM images of the binary Au nanoparticles network materials supported on holey carbon grids. ^[62]

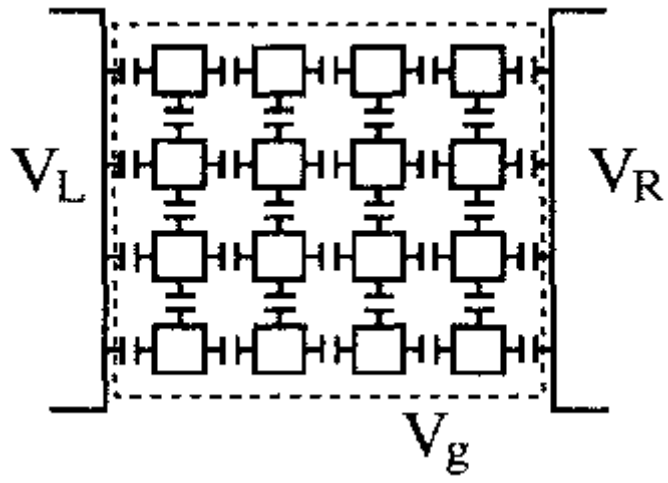


Figure 1-4-7 Schematic of a threshold voltage proportional to the linear array size. ^[64]



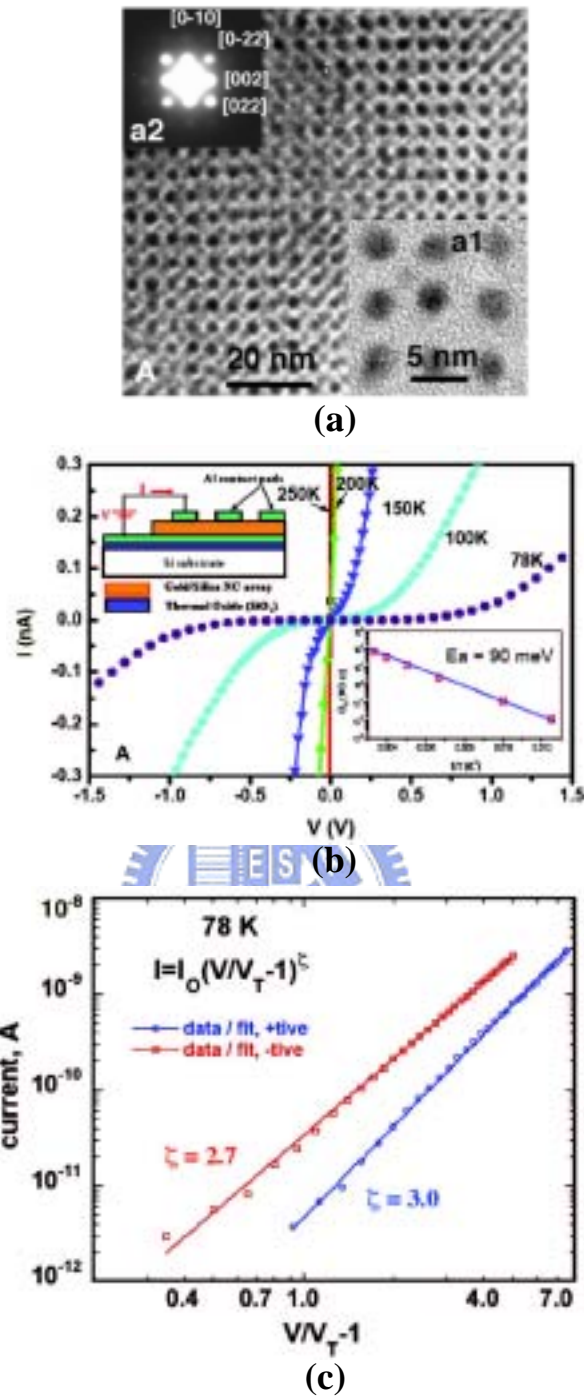
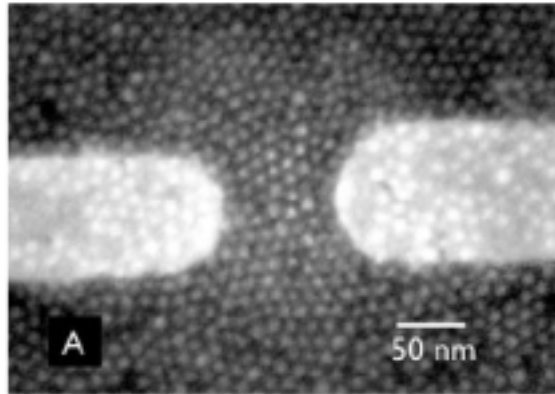
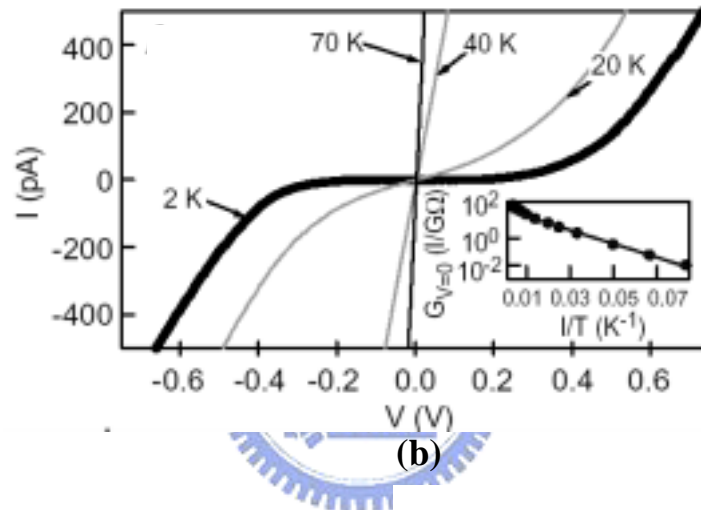


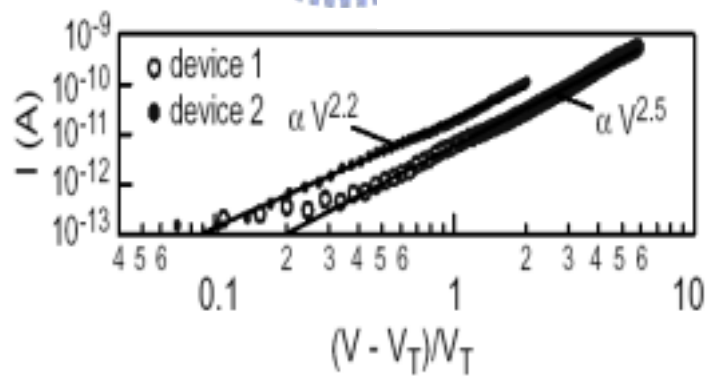
Figure 1-4-8 (a) Representative TEM images of Au nanoparticles /silica mesophases. (b) I - V curves measured from 300 K to 78 K. The inset plots the zero-bias conductance (G_0) versus $1/T$. (c) At $T = 78$ K, current displays a power-law dependence for $V > V_T$ with scaling exponent $\zeta = 2.7$ (negative bias) and $\zeta = 3.0$ (positive bias).^[66]



(a)



(b)



(c)

Figure 1-4-9 (a) SEM image of self-assembled Co nanoparticles superlattice device (b) Device I - V characteristic, for $T= 2$ K (dark line) and 20, 40, and 70 K (light lines). (Inset) Plot of zero-bias conductance versus $1/T$. (c) For $V > V_T$, current displays a power-law dependence.^[67]

Chapter 2: Basic Electron Transport Theory

2-1 Introduction

To understand the electrical conduction of a metal-molecule system, the energy level matching (or mismatching) of the available electrons in the metal (the Fermi level) and the available molecular orbital in the terminal molecule must be considered. In general, the Fermi level of the metallic contact does not energetically line up with either the HOMO or LUMO levels in the molecule.^[68] This mismatch gives rise to a contact barrier, analogous to a Schottky contact. Electron (or hole) transport through such a contact will exhibit a range of phenomena, depending on the height of the barrier, the effective barrier thickness, and the presence of defects; the most prevalent are thermionic emission, direct tunneling, and defect-mediated transport such as hopping.^[69]

2-2 Conduction Mechanisms

Table 1 lists the possible conduction mechanisms with their characteristic behavior, temperature dependence, voltage dependence, and schematic band diagrams. Schottky emission is a process in which carriers overcome the metal-dielectric barrier by thermionic emission, whose current is a strong function of temperature. The extra voltage term on the exponential lowers the barrier at the metal-insulator interface due to image-force correction. Frenkel-Poole (FP) conduction is due to field-enhanced thermal excitation of trapped electrons into the conduction band, a process similar to Schottky emission. Instead of the metal-dielectric barrier height found in Schottky emission, the barrier height in FP conduction represents the depth of the trap potential with respect to the edge of the conduction band. Its current has the same temperature dependence as that of Schottky emission, but with different voltage dependence. As seen from its characteristics, the barrier lowering is twice

that observed in Schottky emission, because of the immobility of the positive charge associated with the trap. Hopping conduction refers to the process in which thermally excited electrons hop from one isolated state to the next, whose conductance also depends strongly on temperature. Different from Schottky emission, there is no barrier lowering effect. The tunneling processes (both Fowler Nordheim tunneling and direct tunneling) do not depend on temperature (to first order), but strongly depend on film thickness and voltage. For a given metal-dielectric film-metal system, certain conduction mechanisms may dominate in certain voltage and temperature regimes. For example, Schottky emission usually plays an important role at high temperatures and low barrier heights; Frenkel-Poole conduction will dominate if there is a high density of traps in the dielectrics; tunneling current will be a major contribution if the dielectrics is thin and under high voltage biases; and for a dielectric film that has a very low density of thermally generated free carriers in the conduction band, hopping conduction is more likely to be observed, especially at low applied voltages and high temperatures.

2-3 Alkanethiol Self-assembled Monolayers (SAMs)

Metal-Insulator-Metal Tunneling

When the molecular layer is a large bandgap insulator, well-defined metal-insulator-metal (MIM) tunneling should occur. Temperature-independent electron transport due to direct tunneling should be the dominant conduction mechanism. Other mechanisms will be discussed in further sections; however, a MIM signature is important to determine if the transport is determined by the band structure of the molecular layer, or due to other less intrinsic effects. An investigation of these systems has been done,^[70,71] specifically alkanethiol $[\text{CH}_3(\text{CH}_2)_{n-1}\text{SH}]$ because it forms a robust SAM on Au surfaces. A few groups have utilized the scanning tunneling microscope,^[73] the conducting atomic force

microscope, ^[73,74] or mercury-drop junctions ^[75] to investigate electron transport through alkanethiols at room temperature, and they claimed that the transport mechanism is tunneling. Although the electron conduction is expected to be tunneling when the Fermi levels of contacts lie within the HOMO-LUMO gap of a short length molecule as for the case of these alkanethiols, in the absence of I (V, T) characteristics such a claim is unsubstantiated since other conduction mechanisms (such as thermionic or hopping conduction) can contribute and complicate the analysis.

Decay coefficients for alkanethiol tunneling obtained by various experimental techniques have previously been reported. ^[72-75] These reported decay coefficients were mainly deduced from the equation ^[76]






$$G = G_0 \exp(-\beta \cdot d) \quad (2-1)$$

which has no explicit length factor d in G_0 . The β values determined from Eq. (2-1) are generally different from those determined from $J \propto \frac{1}{d} \exp(-\beta_0 \cdot d)$ that were deduced from the Simmons model. In order to compare with the previously reported β values, we also performed lengthdependent analysis on our experimental data according to Eq (2-1). This gives a β value from 0.83 to 0.72 \AA^{-1} in the bias range from 0.1 to 1.0 V, which is within the range of the results reported previously. For example, Holmlin, et al. reported a β value of 0.87 \AA^{-1} by mercury drop experiments. ^[75] Wold, et al. have reported β of 0.94 \AA^{-1} and Cui, et al. reported β of 0.6 \AA^{-1} for various alkanethiols by using the conducting atomic force microscope technique. ^[73,74] These reported β values were treated as bias-independent quantities, contrary to the results reported here and that observed in a slightly different alkane system (ligand-encapsulated nanoparticle/alkane-dithiol molecules). ^[79] We have also analyzed our experimental data using the Franz two-band model. ^[77,78] Since there is

no reliable experimental data on the Fermi level alignment in these metal-SAM-metal systems, Φ_B and m^* are treated as adjustable parameters. We performed least square fitting on our data with the Franz nonparabolic E-k relationship using the alkanethiol HOMO-LUMO gap of 8 eV. ^[80,81] Figure 2-1 shows the resultant *E-k* relationship (following references ^[77,78]) and the corresponding energy band diagrams. The best fitting parameters by minimized χ^2 were obtained as $\Phi_B = 1.39$ eV and $m^* = 0.45$ m. Both electron tunneling around LUMO and hole tunneling around HOMO in the forbidden gap can be described by these parameters. $\Phi_B = 1.39$ eV indicates that the Fermi levels are aligned close to one band in either case, therefore the Simmons model is a valid approximation. The previous best fits obtained from the Simmons model of $\Phi_B = 1.40$ eV and $\alpha = 0.65$ (corresponding to $m^* = 0.42$ m for the rectangular barrier case) are in excellent agreement.



Table 2-1: Possible conduction mechanisms.

Conduction Mechanism	Characteristic Behavior	Temperature Dependence	Voltage Dependence	Schematic Band Diagram
Schottky Emission	$I \sim T^2 \text{Exp}\left(-q \frac{F - \sqrt{\frac{qV}{4\pi\epsilon d}}}{kT}\right)$	$\ln\left(\frac{I}{T^2}\right) \sim \frac{1}{T}$	$\ln(I) \sim V^{\frac{1}{2}}$	
Frankel - Pool Conduction	$I \sim VT^2 \text{Exp}\left(-q \frac{F - 2\sqrt{\frac{qV}{\pi\epsilon d}}}{2kT}\right)$	$\ln\left(\frac{I}{T^2}\right) \sim \frac{1}{T}$	$\ln\left(\frac{I}{V}\right) \sim V^{\frac{1}{2}}$	
Hopping Conduction	$I \sim V \text{Exp}\left(-\frac{\Delta E}{kT}\right)$	$\ln\left(\frac{I}{V}\right) \sim \frac{1}{T}$	$I \sim V$	
Fowler-Nordheim Tunneling	$I \sim V^2 \text{Exp}\left(-\frac{4d\sqrt{2m}}{3q\hbar V}(qF)^{1.5}\right)$	—	$\ln\left(\frac{I}{V^2}\right) \sim \frac{1}{V}$	
Direct Tunneling	$I \sim V \text{Exp}\left(-\frac{4\pi d}{h}\sqrt{2mF}\right)$	—	$I \sim V$	



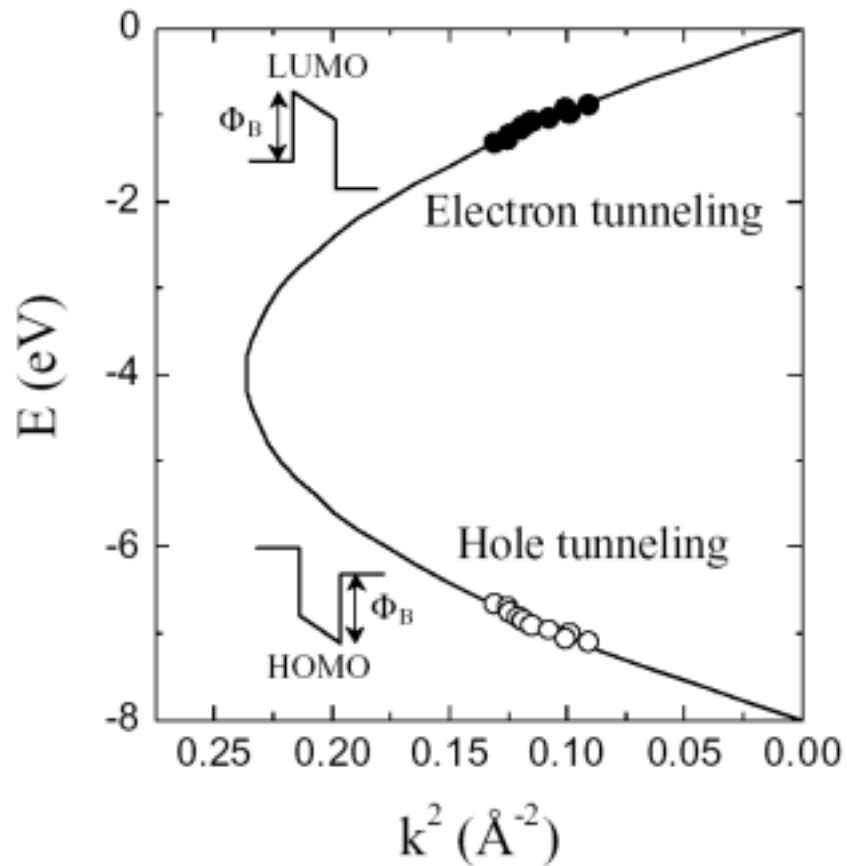


Figure 2-1: E - k relationship (symbols) generated from the length-dependent measurement data for alkanethiols. Solid and open symbols correspond to electron and hole tunnelings, respectively. The insets show the corresponding energy band diagrams. The solid curve is the Franz two-band expression for $m^* = 0.45 m$.

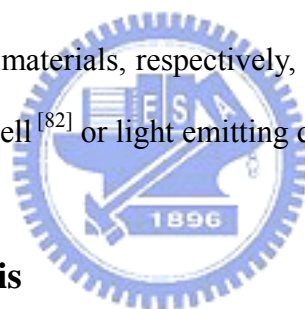
Chapter 3: Enhanced Collective Electron Transport by CdSe Quantum Dots Self-Assembled in the Poly(4-vinylpyridine) Nanodomains of a Poly(styrene-*b*-4-vinylpyridine) Diblock Copolymer Thin Film

3-1 Introduction

For semiconductor nanoparticles (NPs), quantum dots (QDs), that have sizes close to their Bohr exciton radius (typically between 1 and 10 nm), their size-dependent band gaps result in tunable optical properties.^[82] As a result, they possess a wide range of electrical and optical properties and can be used for various applications, such as light-emitting diodes, solar cells, lasers, and transistors. In these applications, composite materials involving nanoparticles and other organic materials were often adopted. Thus, an understanding of the collective electron transport of QDs dispersed in the organic materials is of both scientific and technological importance. A number of reports have described the three- and two-dimensional electron transport in ordered arrays of Au NPs/SiO₂ superlattices,^[83] ZnO QDs assemblies,^[84] and organically capped CdSe QDs.^[85] In addition, electron transport also has been examined in granular films of Au NPs linked by alkanethiol molecules^[86] or poly(4-vinylpyridine)^[87] and Au/spacer/CdSe QD^[88] assemblies. Orbital-selective electron transport through a single CdSe QD measured with an STM has also been reported.^[89]

Thin films of diblock copolymers are versatile templates for the preparation of long-range-ordered nanostructures of dots because their periodic thicknesses can be tuned between 10 and 100 nm.^[90] For example, the selective sequestration of pre-synthesized CdS,^[20] CdSe^[92] and TiO₂^[91a] nanoparticles into one block of diblock copolymers are performed by ensuring the presence of strong interactions between one block of a diblock copolymer and the surface ligands of the nanoparticles. An

assembly of Au nanoparticles enclosed by a block copolymer has also been reported.^[93] In the present study, we prepared self-assembled thin films that consisted of CdSe QDs sequestered in a poly(4-vinylpyridine) nanodomain of poly(styrene-*b*-4-vinylpyridine) (S4VP) diblock copolymer, following a previous approach.^[20,91] By conductive atomic force microscopy (C-AFM) and device measurements, we found that the electron tunneling rate constant in the case of CdSe QDs confined in a poly(4-vinylpyridine) nanodomain is much larger than that in the randomly distributed case. To our knowledge, this is the first time the nanodomain confined effect on the collective electron transport behavior of quantum dots has been reported. This work has great implications on hybrid photovoltaic cell or light-emitting diode applications because collective electron transport by CdSe QDs and hole transport by organic materials, respectively, are critical for producing highly efficient hybrid photovoltaic cell^[82] or light emitting diode.^[94]



3-2 Methods and Analysis

3-2-1 Materials. The poly(styrene-*b*-4-vinylpyridine) (S4VP) diblock copolymer and the poly(4-vinylpyridine) homopolymer were purchased from Polymer Source, Inc. The polydispersity index (Mw/Mn) was 1.23, and the molecular weights (Mn) of the PS and P4VP blocks were 365,300 and 29,400 g/mol, respectively. Cadmium oxide (CdO, 99.9%), selenium (Se, 99.9%, 100 mesh), and trioctylphosphine (TOP) were obtained from Aldrich. Trioctylphosphine oxide (TOPO), 1-octadecene (ODE), and *n*-hexadecylamine (HDA) were purchased from Lancaster. Stearic acid (99%, Avocado), hexane (99%, TEDIA USA), toluene (99%, TEDIA USA), methyl alcohol (MeOH, 99%, TEDIA USA), and pyridine (99%, Showa) were obtained from commercial sources.

3-2-2 Synthesis of CdSe/TOPO QDs. CdSe QDs were synthesized using a

modification of a procedure reported previously.^[100] First, a mixture of CdO (0.2 mmol), stearic acid (0.8 mmol), and ODE (2 g) was heated in a 25 mL three-neck flask to ca. 200 °C to obtain a colorless, clear solution. After this solution had cooled to room temperature, HDA (1.5 g) and TOPO (0.5 g) were added to the flask. This system was then reheated to 280 °C under an argon flow. At this temperature, a selenium solution, prepared by dissolving Se (2 mmol) in TOP (1 mL), was injected rapidly. The growth temperature was reduced to 250 °C for 30 s and then the reaction mixture was cooled to room temperature. The dots were collected as powders using size-selective precipitation with methanol and then redispersed in toluene.

3-2-3 Preparation of CdSe/pyridine QDs. CdSe/TOPO powder (30 mg) was dissolved in pyridine (5 mL) and then stirred at 65 °C for 6 h. Hexane (30 mL) was added to reprecipitate the CdSe. The orange/red suspension was centrifuged and then the powder was collected and redissolved in pyridine.

3-2-4 Preparation of bulk (CdSe/P4VP)-*b*-PS. PS-*b*-P4VP (0.05 g) was added to pyridine (1 mL). Samples of 10, 15, 26, 33, and 48% CdSe/pyridine (with respect to the volume fraction of P4VP block) were mixed in the PS-*b*-P4VP/pyridine polymerization solution. These mixtures were dried slowly under vacuum at 50 °C and then maintained at 160 °C for 48 h to obtain the bulk (CdSe/P4VP)-*b*-PS composites.

3-2-5 Preparation of thin films of (CdSe/P4VP)-*b*-PS. Micellar solutions (0.5 wt%) of (CdSe/P4VP)-*b*-PS were prepared by dissolving bulk (CdSe/P4VP)-*b*-PS in toluene. The micellar solutions were spin-coated at 5000 rpm for 60sec on carbon-coated silicon wafers for transmission electron microscopy (TEM), and Pt-coated wafer for conductance atomic force microscopy (C-AFM) and device measurement. We prepared the sample of CdSe distributed in P4VP homopolymer under the same

conditions we had used to prepare (CdSe/P4VP)-*b*-PS, including the amount of CdSe in P4VP and the thickness of the thin CdSe/P4VP film.

3-2-6 Characterization. TEM images were obtained using a JOEL-2010 transmission electron microscope. The thin film sample for TEM was prepared by using 1% HF to remove it from the carbon-coated silicon wafer. C-AFM measurements were performed using a Digital Nanoscope IV3100 under ambient conditions. The current-voltage (I-V) characteristics of device of thin films of (CdSe/P4VP)-*b*-PS was measured by Hewlett-Packard 4156B. Using a base pressure below 1×10^{-6} Torr, a layer of Al (100nm) was vacuum deposited as top electrode. UV-Vis absorption spectra were obtained on an Agilent 8453 spectrometer by scanning between 190 and 1000 nm. Photoluminescence spectra (PL) were obtained at room temperature using a Hitachi F4500 fluorescence spectrophotometer. The concentrations of the CdSe/TOPO in toluene and CdSe/pyridine solutions were diluted to 6×10^{-5} M for the UV-Vis and PL spectroscopy experiments. Small-angle X-ray scattering experiments were performed on a wiggler beamline BL-01B1 at the National Synchrotron Radiation Research Center, Taiwan. The cyclic voltammetry (CV) curve of pure P4VP was measured by coating the polymer onto a Pt plate and using a standard calomel electrode as the reference and 0.1 M (*n*-Bu)₄NBF₄/acetonitrile as the electrolyte; the scanning rate was set to 50 mV/sec.

3-3 Results and Discussions

Scheme 3-1 demonstrates the process for preparing a mono-layered (CdSe/P4VP)-*b*-PS thin film. First, the TOPO ligands on CdSe QDs were exchanged by hydrophilic pyridine ligands. Then, pyridine-modified CdSe QDs and PS-*b*-P4VP block copolymer are dissolved and mixed in pyridine, and CdSe QDs are distributed selectively in the P4VP phase due to the dipole-dipole interactions. After

drying, (CdSe/P4VP)-*b*-PS in bulk form was obtained. Subsequently, toluene, which is a good solvent for PS but a poor one for P4VP, is used to form a solution containing micelles of CdSe/P4VP-core and PS-shell. Figure 3-1a displays the transmission electron microscopy (TEM) image of a thin film of 48% (CdSe/P4VP)-*b*-PS obtained without staining. The dark region represents the CdSe/P4VP composite phase (because of the higher electron density of cadmium). The spherical nanostructure of PS-*b*-P4VP is, therefore, revealed clearly. The diameter of the CdSe/P4VP sphere was ca. 35 nm, and the inter-domain distance was ca. 100 nm. The inset of Figure 3-1a reveals that CdSe QDs were dispersed homogeneously in the P4VP nanodomain. Figure 3-1b displays a schematic representation of the C-AFM method we used to analyze the CdSe/P4VP spheres embedded in the polystyrene. The current image was measured at the sample bias of $V_B = 8$ V. Figure 3-1c presents the topographic and current images of a section of the thin film of 48% (CdSe/P4VP)-*b*-PS. In the height image, the light regions having a size of ca. 35 nm represent the CdSe/P4VP domains, while the dark area represents the polystyrene matrix. Because the thickness of the thin film is smaller than the size of the CdSe/P4VP domain (23 vs. 30 nm), this image indicates that the microphase-separated (CdSe/P4VP)-*b*-PS exists as a monolayered thin film. In the current image, the values of the currents of the P4VP/CdSe phases (light region) were ca. 30–40 pA, whereas that of the PS phase (dark region) was at the level of the noise (ca. 0.5 pA).

Figure 3-2a displays the current–voltage (I – V) curves of a single CdSe/P4VP nanodomain as measured by C-AFM. The turn-on voltages for the CdSe/P4VP nanodomain decreased as the number of incorporated CdSe QDs increased. This phenomenon occurs because the electron mobility from the probe to the nanodomain increased upon increasing the density of the CdSe QDs. The linear regions of the I – V curves represent the Ohmic behavior,^[98] and indicate constant conductivities (σ)

that can be calculated from the slope of the curves.^[95] The nonlinear regions were due to the electron tunneling from probe tip to the conduction band of CdSe QDs, which must overcome the barrier height (ϕ_e) of the P4VP between the tip and CdSe (Inset of Figure 3-2a).^[95, 101a] A tunneling process, in which electron injection occurs under a forward bias, can be properly modeled using the Fowler–Nordheim (FN) equation. The FN equation can be used to determine the electron barrier height (ϕ_e).^[95] The ϕ_e values for the 10, 15, 26, 33, and 48% CdSe QDs in the P4VP block were 2.4, 2.2, 2.0, 1.8, and 1.5 eV, respectively.^[95] The electron barrier height (ϕ_e) decreases monotonically when the amount of CdSe QDs in the P4VP block increases, owing to the fact that the distance between tip and CdSe QDs decreased at higher CdSe QDs densities. Figure 3-2b displays the conductivity of a single CdSe/P4VP nanodomain plotted against the volume fraction of incorporated CdSe in P4VP. The conductivity of the CdSe/P4VP nanodomain displays only a slight change at low CdSe loading, exhibits a sharp increase at a critical loading, and becomes saturated at high loading. Hence, the conductivity of polymers incorporating CdSe QDs is best described by a percolation theory (the solid curve in Figure 3-2b represents the best fit to the experiment data).^[95] Table 3-1 lists the conductivity of a single CdSe/P4VP nanodomain of the samples, σ , as ranging from 10^{-5} to 10^{-7} cm^{-1} . The conductivity (σ) increases as the amount of CdSe increased, owing to the fact that the distance between CdSe QDs decreased at higher CdSe QDs densities. We also obtained the averaged current–voltage ($I_{\text{ave}}-V$) curves of a single CdSe/P4VP nanodomain in PS matrix by a sandwiched device.^[95] The conductivity (σ) also increases as the amount of CdSe increased and is of the same order of magnitude as compared to that by C-AFM measurement, ranging from 10^{-5} to 10^{-7} cm^{-1} , given in Table 3-1.

Figure 3-3a displays a plot of $-\ln(\sigma)$ vs. the edge-to-edge interparticle distance

(δ_e) as measured by C-AFM and in a device. The conductivity in terms of δ_e and temperature (T) is described^[86, 96] by Eq. (3-1):

$$\sigma(\delta_e, T) = \sigma_0 \exp[-\beta_d \delta_e] \exp\left[\frac{-E_A}{RT}\right] \quad (3-1)$$

where σ is the value of the conductivity of the resulting composite, β_d is the electron tunneling coefficient, δ_e is the edge-to-edge interparticle distance,^[95] E_A is the activation barrier energy, R is the gas constant, and T is the temperature. The linear slope in the plot of $-\ln(\sigma)$ vs. δ_e indicates an electron hopping mechanism and the value of the slope (i.e., β_d) is 0.3 A^{-1} . In our system, the value of β_d differs from that found in other cases. For instance, the value of β_d is $0.2\text{--}0.6 \text{ A}^{-1}$ for electron tunneling through π -bonded molecules, and ca. $0.6\text{--}1.0 \text{ A}^{-1}$ for saturated molecules.^[97] The electron tunneling coefficient β_d can be described^[97] by Eq. (3-2):

$$\beta_d = 2\sqrt{\frac{2m^* \phi_0}{\hbar^2}} \quad (3-2)$$

where m^* is the electron effective mass, ϕ_0 is the electron tunneling barrier height between the dots, and \hbar is the reduced Planck constant. Electron tunneling from one dot to the next must overcome the tunneling barrier height (ϕ_0) of the spacer between the two dots. We found that the value of β_d in the CdSe-P4VP-CdSe system (0.3 A^{-1}) is small when compared to that in the Au-alkanethiol-Au system ($0.8 - 1.2 \text{ A}^{-1}$), because the tunneling barrier height between the conduction band of CdSe and the lowest unoccupied molecular orbital (LUMO) of P4VP is smaller than that between the Fermi level of Au and the LUMO of an alkanethiol (Figure 3-3b).^[86, 87] The smaller β_d value for (CdSe/P4VP)-*b*-PS than that for Au-alkanethiol indicates that the edge-to-edge interparticle distance has less effect on the conductivity for (CdSe/P4VP)-*b*-PS than for the Au-alkanethiol-Au

system. The effective electron mass, $m^* = 0.14 m$, was calculated by Eq. (3-2). Where m is the free electron mass.

To compare the effect that nanodomain confinement has on the CdSe QDs, with respect to their randomly distributed state, we prepared four samples that had the same density in P4VP: the first two contained 48% CdSe by volume with respect to the P4VP block in a PS-*b*-P4VP diblock copolymer and the second two contained 48% CdSe by volume in a P4VP homopolymer. The electron tunneling rate constant (k_{ET}) can be estimated from the conductivity by assuming a cubic-lattice model described by an equation.^[86, 95] Table 3-1 indicates that both the electron tunneling rate constant and conductivity for the nanodomain confined case is about seven times larger than that for the randomly distributed case. This can be explained by the fact that the collective electron transport of CdSe QDs in the nanodomain confined case was restricted by the P4VP sphere, while the collective electron transport for the randomly distributed CdSe QDs followed a free pathway behavior. The electron tunneling rate constant increased as the amount of CdSe increased.

Table 3-2 displays the characteristic properties of CdSe QDs. The average size of the CdSe QDs was determined from both UV-Vis absorption spectroscopy and transmission electron microscopy measurements to be ca. 3.6 nm.

The FN equation can be expressed^[101] as Eq. (3-3):

$$I(C) = \frac{A_{eff} q^3 E^2 m}{8\pi h \phi_e m^*} \exp \left[\frac{-8\pi \sqrt{2m^*} \phi_e^{3/2}}{3h q E} \right] \quad (3-3)$$

where A_{eff} is the effective contact area, E is the applied electric field, ϕ_e is the electron barrier height, and q, m^*, m , and h are electron charge, effective mass of the electron, free electron mass, and Plank constant, respectively. If we assume $E = V/L$, where V is the applied voltage, and L is the separation between the two

electrodes, then

$$I(V) = D V^2 \exp(-B/V)$$

$$\text{where } D = \frac{A_{\text{eff}} q^3 m}{8\pi h \phi_e L^2 m^*}, \text{ and } B = \frac{8\pi \sqrt{2m^*} \phi_e^{3/2} L}{3 h q} = 6.83 L \left(\frac{m^*}{m} \right)^{1/2} \phi_e^{3/2} \text{ (volts)}$$

Here the units of L and ϕ_e are nm and eV, respectively. By fitting the measured I - V curves to FN theory, the B for the 10, 15, 26, 33, and 48% CdSe QDs in the P4VP block were 284.8 V, 249.9 V, 216.6 V, 184.9 V, and 140.7 V, respectively. Using the fitted B values and the thickness between two electrodes of ~ 30 nm, the ϕ_e for the 10, 15, 26, 33, and 48% CdSe QDs in the P4VP block were $1.24(m/m^*)^{1/3}$, $1.14(m/m^*)^{1/3}$, $1.03(m/m^*)^{1/3}$, $0.93(m/m^*)^{1/3}$, and $0.77(m/m^*)^{1/3}$ eV, respectively. The effective electron mass, $m^* = 0.14 m$, was calculated by Eq. (3-2). The ϕ_e for the 10, 15, 26, 33, and 48% CdSe QDs in the P4VP block were 2.4, 2.2, 2.0, 1.8, and 1.5 eV, respectively.

Additionally, we calculated the conductivity values using Eq. (3-4):

$$\sigma = \frac{1}{R} \times \frac{L}{A} \quad (3-4)$$

where R is the resistance, L is the thickness between two electrodes, and A is the contact area of the electrode. In this case, L is equal to the diameter of the nanodomain, and A is defined by the contact area between the tip and the sample, 100 nm^2 .^[102]

The percolation model for the conductivity of CdSe/P4VP is given in Eq. (3-5), which provides^[87] a first-order approximation:

$$\sigma = \sigma_c + (\sigma_m - \sigma_c) \left[\frac{(\varphi - \varphi_c)}{(F - \varphi_c)} \right]^t \quad (3-5)$$

where σ is the value of the conductivity of the resulting composite, σ_c is the value of the conductivity at the percolation threshold, σ_m is the maximal conductivity value, φ is the volume fraction of QDs, φ_c is the critical volume

fraction, F is the limiting value of the volume fraction, and t is the critical exponent. Table 3-3 lists the corresponding parameters for C-AFM and device measurements.

Figure 3-4a displays the averaged current–voltage ($I_{\text{ave}}-V$) curves of a single CdSe/P4VP nanodomain in PS matrix derived from the measurement of a sandwiched device, in which a Pt-coated Si wafer as the bottom electrode and Al film as the top electrode. The current was assumed to flow through CdSe/P4VP nanodomain, owing to a much higher resistance of PS phase. The current density of a single nanodomain can therefore be calculated from the density of CdSe/P4VP nanodomain in PS phase by using the following parameters, where the area of Al electrode is $1.96 \times 10^{-3} \text{ cm}^2$; the density of CdSe/P4VP nanodomain in PS phase is $3.1 \times 10^9 \text{ cm}^{-2}$ as obtained from TEM image. The number of CdSe/P4VP nanodomains under the Al electrode is a product of the area of Al electrode and the density of CdSe/P4VP nanodomains, which is about 6×10^6 . The I_{ave} is obtained by dividing the current by the number of CdSe/P4VP nanodomains and then by the area of a CdSe/P4VP nanodomain. Similar to the results by conductive-AFM, the turn-on voltages for the CdSe/P4VP nanodomain decreased as the number of incorporated CdSe QDs increased. Figure 3-4b displays the conductivity plotted against the volume fraction of incorporated CdSe in P4VP. The electron barrier height (ϕ_e), determined by Eq. (3-3), from the Al electrode to the nanodomain decreases monotonically when the amount of CdSe increases. We also calculated the conductivity values using the linear region of $I_{\text{ave}}-V$ curves by Eq. (3-4). The solid curve in Figure 3-4b represents the best fit of percolation model, Eq. (3-5), to the experiment data; Table 3-3 lists the corresponding parameters.

Figure 3-5a displays one-dimensional small-angle X-ray scattering patterns (SAXS) of (CdSe/P4VP)-*b*-PS obtained using synchrotron radiation. The scattering

maxima, which are denoted by the letter “i” (i = 1, 2), are form factor peaks associated with scattering from the isolated spherical domains. The form factor peaks shifted slightly to lower values of Q as the amount of incorporated CdSe increased, which indicates that the volume or size of the CdSe/P4VP composite domains increased. The average diameter of the P4VP domains of pure PS-*b*-P4VP, deduced from the positions of the form factor maxima, is 30 nm. The average diameters, measured by their volume, for the 10, 15, 26, 33, and 48% CdSe QDs in the P4VP block were 31, 31.4, 32.4, 33, and 34.2 nm, respectively, assuming that the density of P4VP and CdSe remained the same before and after mixing. Inset of Figure 3-5a lists the free volume per CdSe dot in a single P4VP domain (V_{free}), which is defined by the average volume of an occupied CdSe dot and can be estimated by using Eqs. (3-6) and (3-7):

$$\frac{V_{CdSe/P4VP} - V_{P4VP}}{V_{CdSe}} = n \quad (3-6)$$

$$\frac{V_{CdSe/P4VP}}{n} = V_{free} \quad (3-7)$$

where $V_{CdSe/P4VP}$ is the volume of a single CdSe/P4VP composite domain, V_{P4VP} is the volume of a single P4VP domain, V_{CdSe} is the volume of a CdSe QD, and n is the maximum number of CdSe QDs in a single P4VP domain. The relationship between the conductivity and the edge-to-edge interparticle distance (δ_e) can be determined by assuming a cubic lattice model for the CdSe QDs. The values of δ_e were calculated using Eq. (3-8) based on the cubic lattice model presented in the Figure 3-5b.^[86, 96]

$$\delta_e = L - D = (V_{free})^{1/3} - D \quad (3-8)$$

where D is the diameter of the CdSe QDs. The value of δ_e decreased when the amount of CdSe increased, as displayed in the inset of Figure 3-5b.

The first-order electron tunneling rate constant (k_{ET}) can be estimated from the conductivity by assuming a cubic-lattice model described^[86, 96] by Eq. (3-9):

$$k_{ET}(s^{-1}) = \frac{6RT\sigma}{F_a^2 \delta_c^2 C} \quad (3-9)$$

where R is the gas constant, T is the temperature, σ is the conductivity, F_a is the Faraday constant, δ_c is the average center-to-center interparticle distance ($\delta_c = \delta_e + 32 \text{ \AA}$), and C is the concentration of CdSe in the P4VP domain (mol/cm^3).^[103]

3-4 Conclusions

We have demonstrated that the electron tunneling rate constant in the case of CdSe QDs confined in a poly(4-vinylpyridine) nanodomain is much larger than in the randomly distributed case and it increases upon increasing the amount of CdSe. The value of electron tunneling coefficient of the CdSe-P4VP-CdSe system is 0.3 \AA^{-1} . The electron barrier height from the tip of the probe to the nanodomain decreased monotonically and the conductivity of the CdSe/P4VP nanodomain increased, following a percolation model, as the amount of CdSe increased.

Scheme 3-1: Fabrication of a self-assembled (CdSe/P4VP)-*b*-PS thin film by incorporating selectively dispersed pre-synthesized CdSe QDs in P4VP domain.

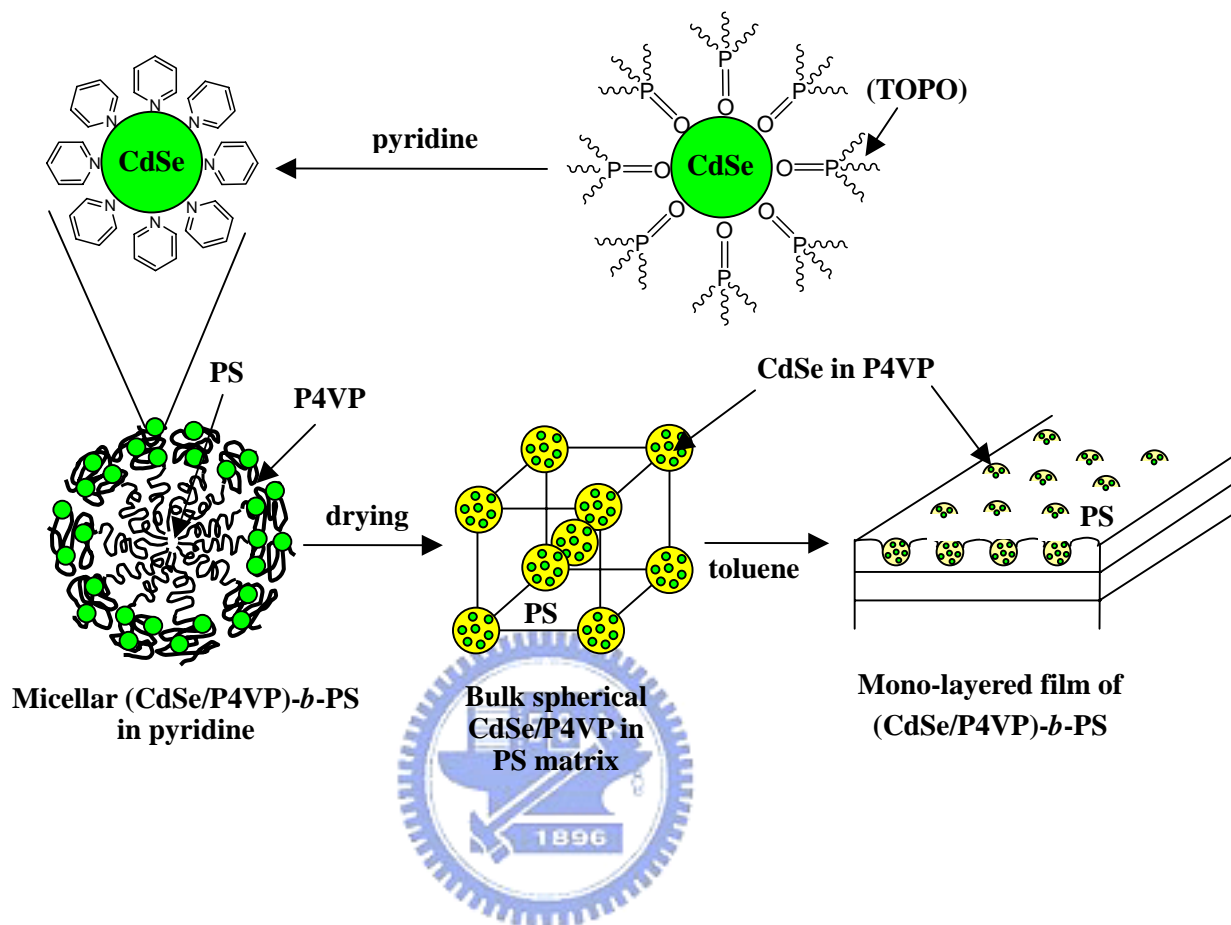


Table 3-1: Conductivity (σ) and electron tunneling rate constant (k_{ET}) for confined and non-confined CdSe in P4VP domain as measured by conductive-AFM and in a device.

vol% of CdSe in P4VP	σ (cm^{-1}) $\times 10^6$				k_{ET} (s^{-1}) $\times 10^{-3}$			
	(CdSe/P4VP)- <i>b</i> -PS (confined)		CdSe/P4VP (non-confined)		(CdSe/P4VP)- <i>b</i> -PS (confined)		CdSe/P4VP (non-confined)	
	C-AFM	device	C-AFM	device	C-AFM	device	C-AFM	device
10	0.2	0.13	0.03	0.01	1.4	0.9	0.2	0.09
15	0.6	0.46	0.08	0.05	4.2	3.2	0.5	0.4
26	7.4	5.2	0.82	0.6	39	27	4.3	3.1
33	20	14	2.2	1.6	87	60	9.6	6.9
48	41	28	4.8	2.9	179	127	21.3	13.2



Table 3-2: Characteristic Properties of CdSe Quantum Dots

Absorption onset (λ_0) ^a	Diameter in toluene ^b	First absorption peak ^c	Emission wavelength ^d	Average diameter ^e
498 nm	3.7 nm	540 nm	565 nm	3.6 nm

^a The onset absorption wavelength of CdSe QDs in toluene as obtained from UV–Vis spectra.

^b The sizes of the CdSe QDs in toluene were calculated using the onset absorption obtained from UV–Vis spectra and the following equation:

$$E_{g_{as}} - E_{g_{ref}} = \Delta E_g \approx \frac{\hbar^2 \pi^2}{2R^2} \cdot \frac{1}{\mu} - \frac{1.8e^2}{\epsilon R}$$

^c The first excitonic absorption wavelength of CdSe QDs in toluene as obtained from UV–Vis spectra.

^d The emission wavelength was determined from the photoluminescence measurements.

^e The sizes of the CdSe QDs were determined from TEM analyses.



Table 3-3: Electrical conductivity parameters for the CdSe/P4VP nanodomain

measuring mode	$\log \sigma_c$ (cm^{-1})	$\log \sigma_m$ (cm^{-1})	φ_c	F	t
C-AFM	-6.38	-4.32	0.15	0.5	1.7
device	-6.65	-4.58	0.15	0.5	1.7



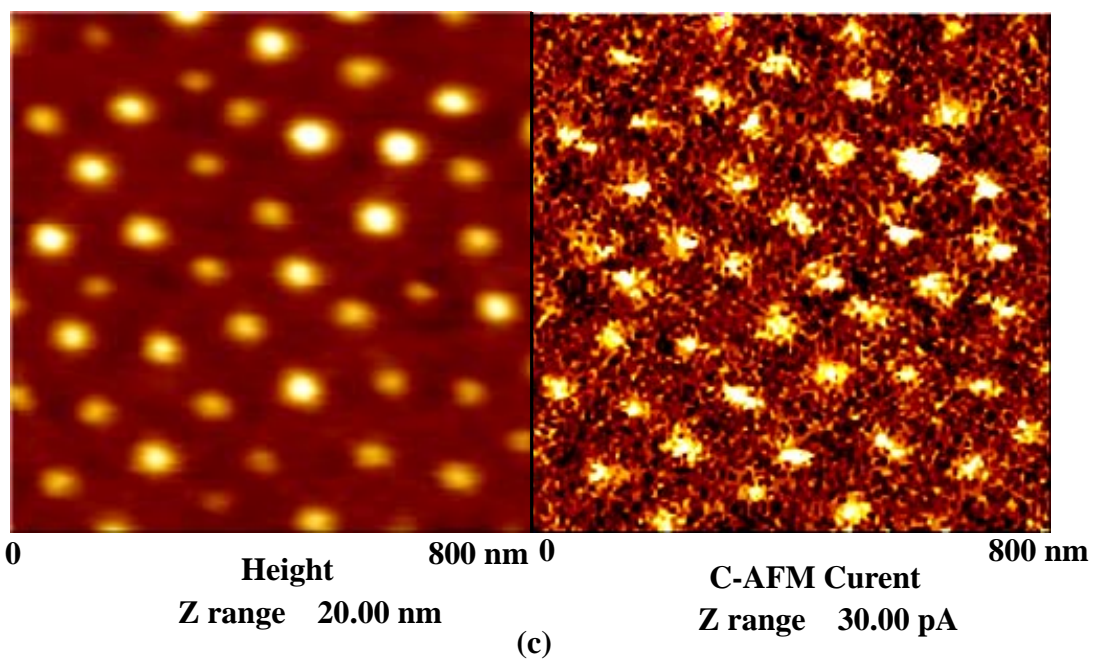
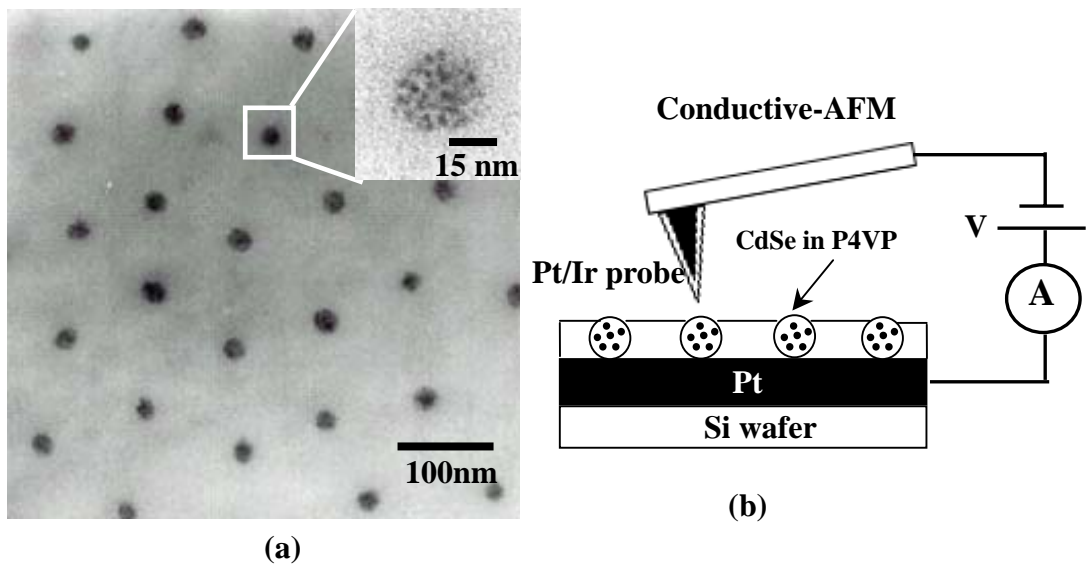


Figure 3-1: (a) TEM image of a thin film of 48% (CdSe/P4VP)-*b*-PS obtained without staining. (b) A schematic representation of the conductive-AFM imaging mode employed. (c) Conductive-AFM image of a thin film of 48% (CdSe/P4VP)-*b*-PS.

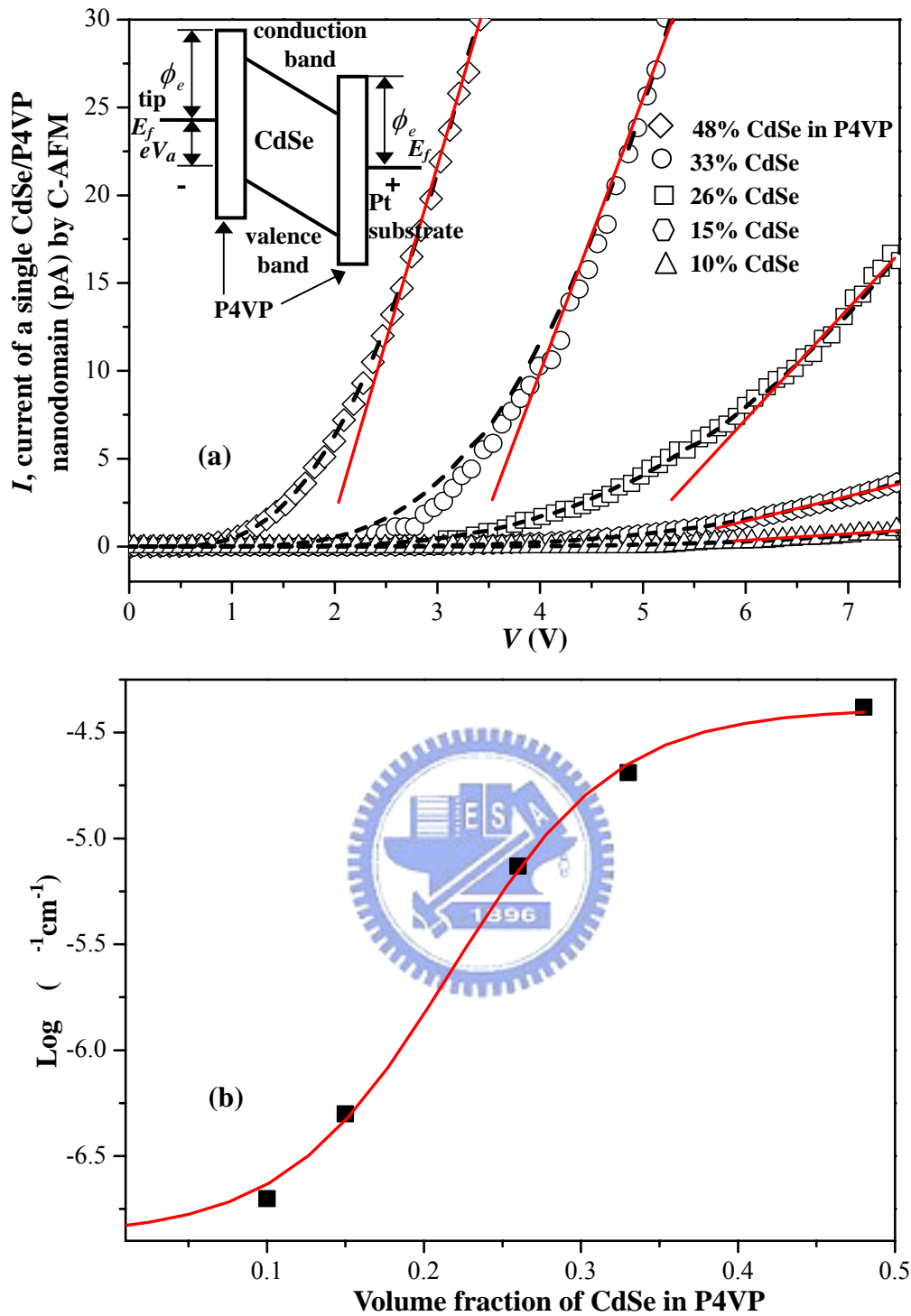


Figure 3-2: (a) I - V curves of thin film (CdSe/P4VP)- b -PS by conductive-AFM. The dotted lines denote best fits to the FN equation. Inset: The energy bands of the conductive-AFM tip, CdSe/P4VP monolayer, and the substrate. E_f is the electron Fermi energy inside the Pt, and ϕ_e is the barrier height between Pt and CdSe/P4VP. eV_a is the applied potential energy difference between the tip and the substrate. (b) Plot of the conductivity vs. the amount of CdSe in P4VP.

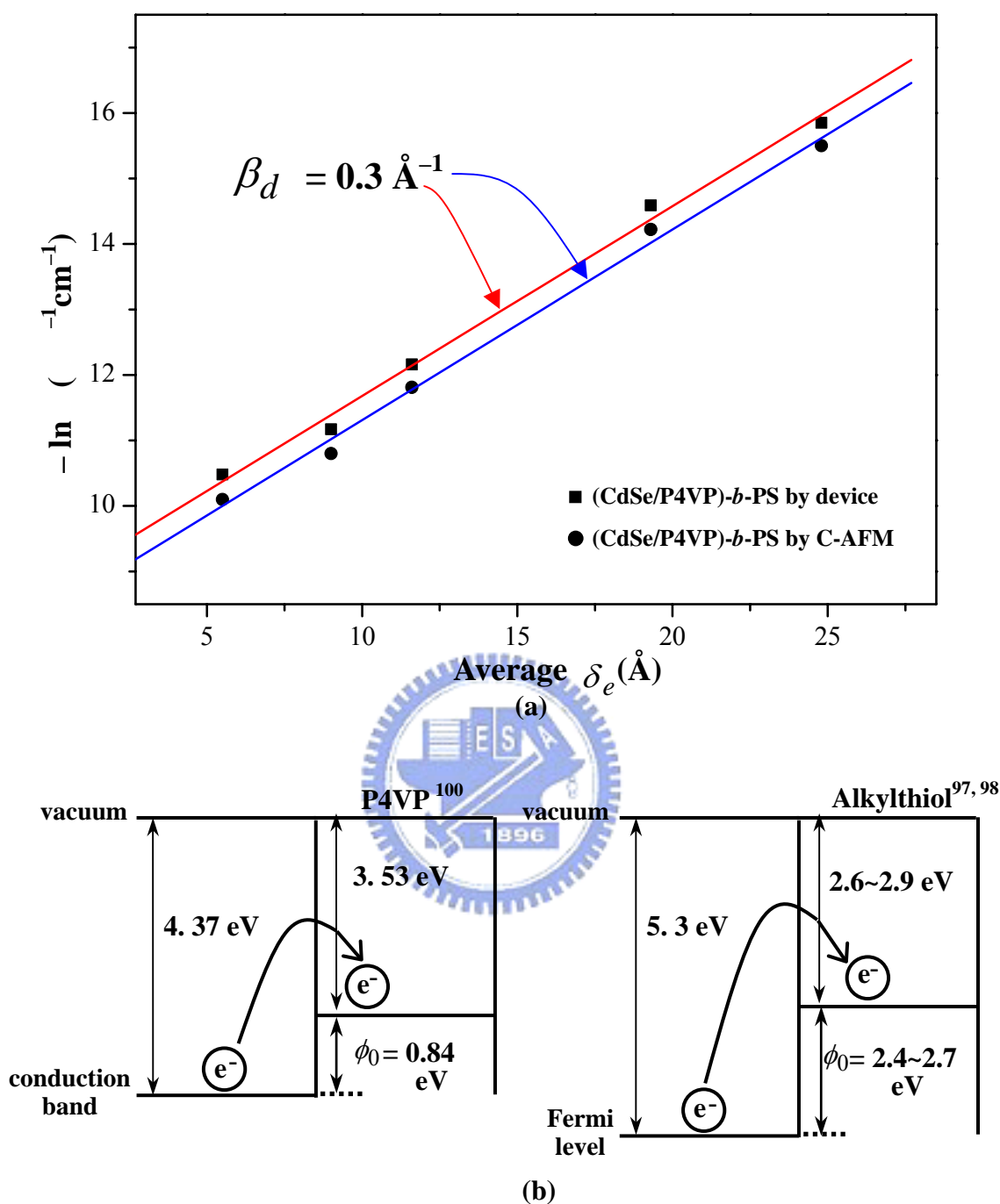


Figure 3-3: (a) Plot of $-\ln(\sigma_{(\text{CdSe/P4VP})\text{-}b\text{-PS}})$ vs. δ_e as measured by conductive-AFM and device. (b) Schematic diagram of the barrier height for electron tunneling from the conduction band of CdSe to the LUMO of P4VP and from the Fermi level of Au to the LUMO of an alkanethiol.

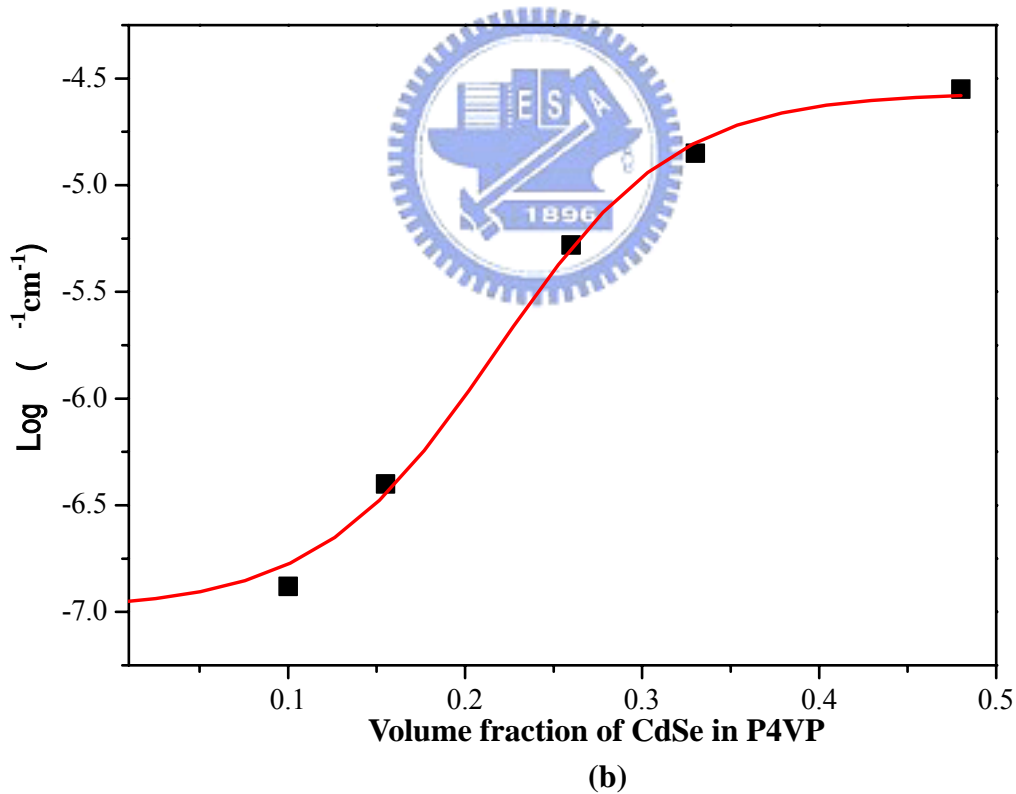
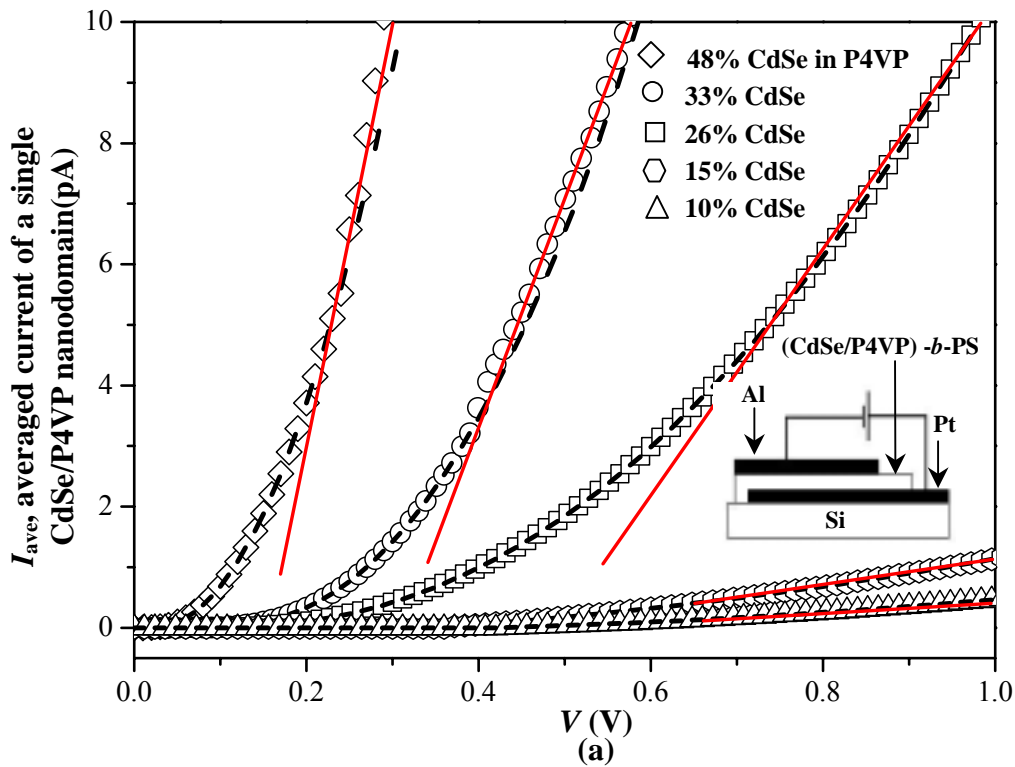


Figure 3-4: (a) $I_{ave}\text{-}V$ curves of thin film $(\text{CdSe/P4VP})\text{-}b\text{-PS}$ nanocomposites having various contents of CdSe as measured in a device. The dotted lines denote best fits to the FN equation. (b) Plot of the conductivity vs. the amount of incorporated CdSe in P4VP.

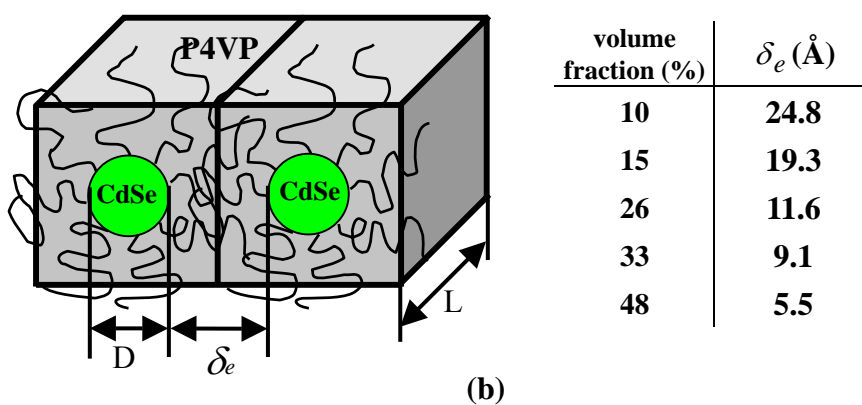
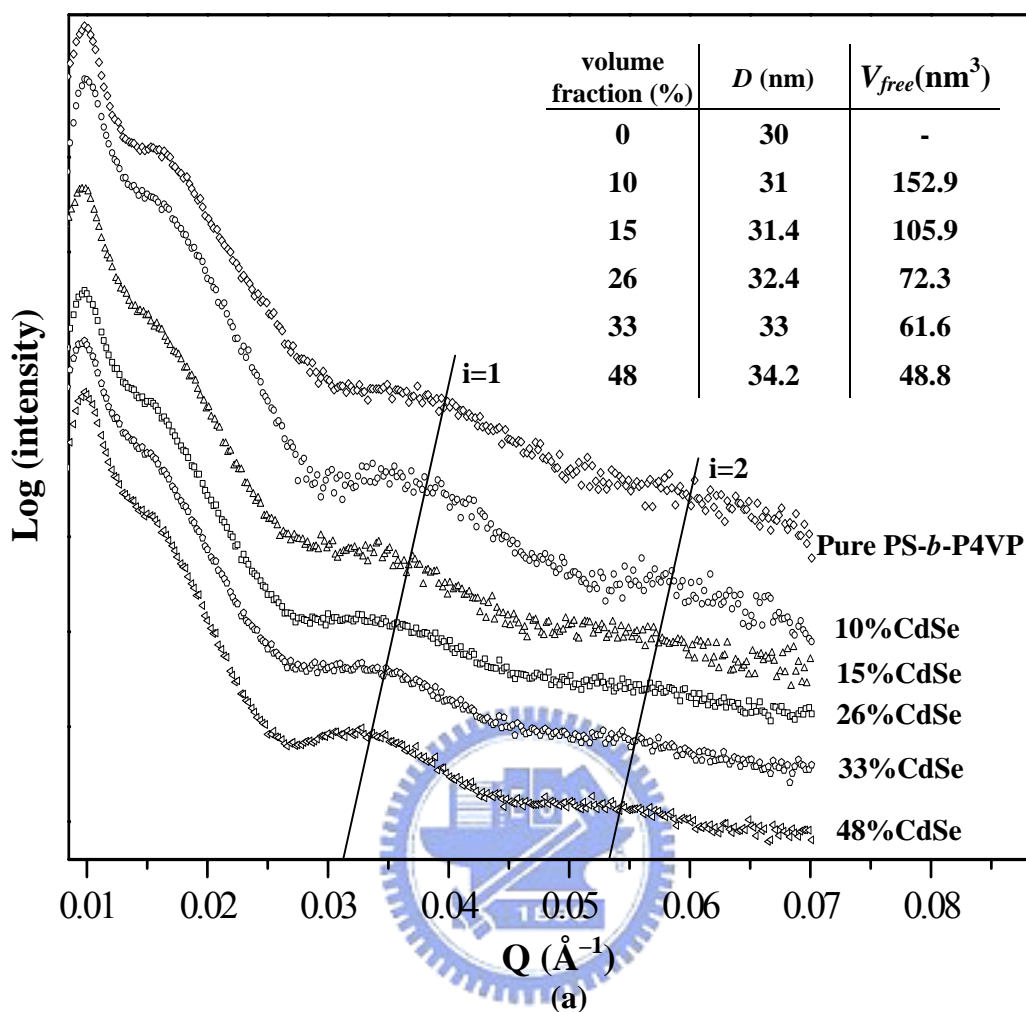


Figure 3-5: (a) Small-angle X-ray scattering of bulk (CdSe/P4VP)-*b*-PS nanocomposites having various contents of CdSe. (b) A schematic representation of the cubic lattice model for the free volume per CdSe dot in a single P4VP domain.

Chapter 4: Collective Electron Transport in Au Nanoparticles Self-Assembled in the Poly(4-vinylpyridine) Nanodomains of a Poly(styrene-*b*-4-vinylpyridine) Diblock Copolymer Thin Film

4-1 Introduction

Metal nanoparticles (NPs) that have diameters in the range of 1–10 nm are the subject of much current research interest because the optical, electronic, and chemical properties of these materials, such as their single charge tunneling and plasmon resonances, are size-dependent.^[104–106] As a result, such NPs are being investigated for use in various applications, including memory cells,^[107] single-electron transistors,^[108] biological sensors,^[109] and catalysts.^[110] In these applications, the NPs are often capped with organic ligands or are surrounded by other dielectric materials. Thus, an understanding of the collective electron transport of NPs dispersed in organic or dielectric materials is of both scientific and technological importance. A number of reports have described two- or three-dimensional electron transport in (a) ordered arrays of dodecanethiol-capped Ag^[111] and Au^[112] nanoparticles, Au NPs/SiO₂ superlattices,^[113] organically capped Co NPs,^[114] and CoPt₃ NPs^[115] and (b) disordered arrays of granular films of Au NPs linked by alkanethiol molecules^[116] and Au/spacer/CdSe NP assemblies.^[117] In contrast, very few reports describe one-dimensional electron transport within granular films, mainly because of the difficulties encountered when preparing such samples.

Nanostructured block copolymers that have period thicknesses between 10 and 100 nm, because of microphase separation of incompatible blocks, can be used as templates to selectively control the spatial arrangement of NPs within one of the blocks.^[118–121] For example, the selective sequestration of pre-synthesized CdSe,^[122a,b] CdS,^[134] and TiO₂^[91a] NPs into one block of a diblock copolymer can be performed by ensuring that strong interactions exist between that block of the

copolymer and the surface ligands of the NPs. Block copolymers can also be used as nanoreactors for the synthesis of nanomaterials. For example, quasi-regular arrays of Au clusters^[123] and TiO₂ needles^[36] have been obtained through the selective sequestration of metal ions into one block of poly(styrene-*b*-vinylpyridine). In this present study, we followed a previously reported^[124] approach to prepare self-assembled thin films that consisted of Au NPs sequestered in the poly(4-vinylpyridine) (P4VP) nanodomains of a poly(styrene-*b*-4-vinylpyridine) (PS-*b*-P4VP) diblock copolymer. From the current–voltage (*I*–*V*) characteristics of these thin films, we determine the collective electron transport behavior of the Au NPs confined within the P4VP nanodomains and of randomly distributed Au NPs.

4-2 Methods and Analysis

4-2-1 Materials. The poly(styrene-*b*-4-vinylpyridine) (S4VP) diblock copolymer and the poly(4-vinylpyridine) homopolymer were purchased from Polymer Source, Inc. The polydispersity index (Mw/Mn) of S4VP was 1.07; the molecular weights (Mn) of the PS and P4VP blocks were 557,000 and 75,000 g/mol, respectively. Hydrogen tetrachloroaurate(III) trihydrate (HAuCl₄·3H₂O), tri-*n*-octylammonium bromide (TOAB, 99%), and sodium borohydride (NaBH₄, 99%) were obtained from Acros. Trioctylphosphine (TOP, 90%) were purchased from Aldrich. Toluene (99%, TEDIA USA), hexane (99%, TEDIA USA), methyl alcohol (MeOH, 99%, TEDIA USA), and pyridine (99%, Showa) were obtained from commercial sources.

4-2-2 Synthesis of Au/TOP NPs. Au/TOP NPs were synthesized using a modification of a procedure reported previously.^[127] First, HAuCl₄·3H₂O (0.24 g, 0.616 mmol) was dissolved in deionized water (6.25 mL) in a 50-mL three-neck flask. This solution was added to a mixture of TOAB (0.39 g, 0.711 mmol) in toluene (8.125 mL) and stirred vigorously. Once all of the color has transferred from the

aqueous layer into the organic phase, a solution of TOP (0.20 mL, 0.43 mmol) in toluene (2 mL) was injected into the reaction mixture. The organic phase turned bright red; neat TOP was then slowly added dropwise until the mixture turned a milky white color. A solution of NaBH₄ (88.0 mg, 2.33 mmol) in deionized water (5 mL) was then added to the mixture at a nominal rate of 7 mL/h using a syringe pump. Upon addition, the organic phase immediately darkened, progressively turning a deeper brown/black color. After the complete addition of NaBH₄, the reaction mixture was stirred for 30 min. The nanoparticles were collected as a powder through size-selective precipitation with methanol and then they were redispersed in toluene.

4-2-3 Preparation of Au/Pyridine NPs. The Au/TOP NP powder (30 mg) was dissolved in pyridine (5 mL) and then stirred at 65 °C for 6 h. Hexane (30 mL) was added to reprecipitate the Au NPs. The suspension was centrifuged and then the powder was collected and redissolved in pyridine.

4-2-4 Preparation of Bulk (Au NPs/P4VP)-*b*-PS. PS-*b*-P4VP (0.05 g) was added to pyridine (1 mL). Samples of 10, 15, 26, 33, and 48% Au/pyridine (percentages with respect to the volume fraction of P4VP block) were mixed in the PS-*b*-P4VP/pyridine polymerization solution. These mixtures were dried slowly under vacuum at 50 °C and then maintained at 160 °C for 48 h to obtain the bulk (Au NPs/P4VP)-*b*-PS composites.

4-2-5 Preparation of Thin Films of (Au NPs/P4VP)-*b*-PS. Micellar solutions (0.5 wt%) of (Au NPs/P4VP)-*b*-PS were prepared by dissolving bulk (Au NPs/P4VP)-*b*-PS in toluene. The micellar solutions were spin-coated at 5000 rpm for 60 s onto carbon-coated silicon wafers [for transmission electron microscopy (TEM)] and Au-coated wafers [for current-voltage (*I*-*V*) curves measurements]. The sample of Au NPs distributed in the P4VP homopolymer was prepared under the same

conditions used to prepare (Au NPs/P4VP)-*b*-PS, including the amount of Au in P4VP and the thickness of the thin Au NPs/homo-P4VP film.

4-2-6 Preparation of a Sample for Cross-Sectional TEM Imaging. A micellar solution of 48% (Au NPs/P4VP)-*b*-PS in toluene was spin-coated at 5000 rpm for 60 s onto a Au-coated polyethersulfone substrate; a layer of Au (200 nm) was then vacuum-deposited as the top electrode. The sandwiched sample was placed into an epoxy capsule, which was cured at 70 °C for 48 h in a vacuum oven. The cured epoxy samples were microtomed using a Leica Ultracut Uct into ca. 50-nm-thick slices.

4-2-7 Characterization. TEM images were obtained using a JOEL-2010 transmission electron microscope. The thin film sample for TEM was obtained after using 1% HF to remove the film from the carbon-coated silicon wafer. The current–voltage (*I*–*V*) characteristics of the thin film device of (Au NPs/P4VP)-*b*-PS were measured using a Hewlett–Packard 4156B instrument. Using a base pressure below 1×10^{-6} torr, a layer of Au (100 nm) was vacuum-deposited as the top electrode. Small-angle X-ray scattering experiments were performed on a wiggler beamline BL-01B1 at the National Synchrotron Radiation Research Center (NSRRC), Taiwan.

4-3 Results and Discussions

Scheme 4-1 outlines our approach toward preparing a monolayer (Au NPs/P4VP)-*b*-PS thin film. First, the trioctylphosphine (TOP) ligands on the Au NPs, which were used during their synthesis, were replaced with hydrophilic pyridine ligands. These pyridine-modified Au NPs and the PS-*b*-P4VP block copolymer were then dissolved and mixed in pyridine; the Au NPs were distributed selectively in the P4VP phase as a result of dipole–dipole interactions. After drying, the (Au

NPs/P4VP)-*b*-PS sample was obtained in bulk form. Subsequently, toluene, which is a good solvent for PS but a poor one for P4VP, was used to form micelles—having Au NPs/P4VP cores and PS shells—in a solution that was spun into a thin film. Figure 4-1a displays a transmission electron microscopy (TEM) image, obtained without staining, of the top view of a thin film of 48% (Au NPs/P4VP)-*b*-PS. The dark region represents the Au NPs/P4VP composite phase (because of the higher electron density of gold). It is clear that PS-*b*-P4VP had a spherical nanostructure. The diameter of the Au NPs/P4VP sphere was ca. 30 nm, and the inter-domain distance was ca. 90 nm. Figure 4-1b displays an HRTEM image of a single Au NPs/P4VP nanodomain within a thin film of 48% (Au NPs/P4VP)-*b*-PS. The Au NPs were dispersed fairly homogeneously in the P4VP nanodomain. The inset of Figure 4-1b reveals the HRTEM lattice image (with a lattice spacing of ca. 2.8 Å) of one of the Au NPs incorporated within a P4VP nanodomain. The average diameter of the Au NPs was ca. 3.1 nm. Figure 4-1c displays a cross-sectional TEM image of a 48% (Au NPs/P4VP)-*b*-PS thin film. The dark regions at the top and bottom of this image are the Au electrodes; the circled regions are the domains of the Au NPs/P4VP composite. From analyses of the small-angle X-ray scattering peaks, we estimated that the maximum number of Au NPs sequestered within the P4VP nanodomains were ca. 65, 129, 169, 244, and 302 for the 10, 15, 26, 33, and 48% Au NPs, respectively. Figure 4-1d displays a cross-sectional TEM image of a 48% Au NPs/homo-P4VP. Au NPs were randomly distributed in the P4VP thin film.

To compare the effect that nanodomain confinement has on the Au NPs, with respect to their randomly distributed state, we prepared two samples that had the same density of NPs in P4VP: the first contained 48% Au NPs by volume with respect to the P4VP block in a PS-*b*-P4VP diblock copolymer, and the second contained 48% Au NPs by volume in a P4VP homopolymer. Figures 4-2a and 4-2b display the

averaged I - V characteristics of the monolayer (Au NPs/P4VP)- b -PS and Au NPs/P4VP thin films, both measured at temperatures within the range from 250 to 78 K. In both cases, the I - V curves were ohmic at 250 K, but become increasingly nonlinear upon decreasing the temperature. At 100 K and below, conduction occurred through the composite only at potentials above a minimum threshold voltage, V_T , which indicates that a collective Coulomb blockade resulted from electrical isolation of the NPs. A model for low-voltage electron transport through an array of Coulomb islands predicts thermally activated behavior for the zero-bias conductance: [112–115,125]

$$G_0 \propto \exp\left[\frac{-E_a}{k_B T}\right] \quad (4-1)$$

where G_0 is the zero-bias conductance, E_a is the activation energy to charge an electrically neutral nanocrystal, k_B is the Boltzmann constant, and T is the temperature. The insets to Figures 4-2a and 4-2b present plots of $\ln G_0$ vs. $1/T$. From the slopes of the theoretical fits obtained using Eq. (4-1), we calculated the experimental values for the activation energies (E_a) of the nanodomain-confined and randomly distributed samples to be 27 and 28 meV, respectively. The value of E_a can be expressed as $e^2/2C$, where e is the charge of the electron and C is the total capacitance of a nanoparticle, resulting from the inter-nanoparticle capacitance, C_i , and the nanoparticle self-capacitance, C_s . Neglecting the small contribution to C from C_s , we obtained $C \approx n \cdot C_i \approx n \cdot 2\pi\epsilon_0\epsilon r \ln[(r + d/2)/(d/2)]$, where ϵ is the dielectric constant of the surrounding P4VP matrix (ca. 3), r is the nanoparticle radius (1.5 nm), d is the interparticle distance (0.55 nm), and n is the average number of nearest neighbors (assuming each nanoparticle has an average of between six to twelve nearest neighbors).^[114, 126] We estimated that the total capacitance (C) would be between 2.3 and 4.5 aF; therefore, we calculated the activation energy to be

35–17.5 meV ($E_a \approx e^2/2C$). Thus, the experimental values of the activation energies within both the nanodomain-confined and randomly distributed samples are in reasonable agreement with the calculated values. Figure 4-2c displays representative current–voltage scaling data obtained for these two samples at 78 K. The accessible current-conducting pathways are described^[112–115,124] by Eq. (4-2):

$$I \propto \left(\frac{V}{V_T} - 1 \right)^\zeta \quad (4-2)$$

(for $V > V_T$), where I is the current, V is the voltage, ζ is a scaling exponent, and V_T is the threshold voltage. The scaling exponent ζ can be regarded as the dimensionality for collective electron transport for arrays of dots as modeled in a previous study.^[124] We obtained power-law scalings (ζ) of 1.31 for the nanodomain-confined sample and 2.84 for the randomly distributed sample. These results indicate that quasi-one-dimensional collective electron transport occurs for the nanodomain-confined Au NPs and that quasi-three-dimensional collective electron transport occurs for the randomly distributed Au NPs. Figure 4-2d presents a plot of V_T vs. d for nanodomain-confined and randomly distributed samples having various Au NP contents. The values of V_T of the Au NPs in the P4VP domains of PS-*b*-P4VP were ca. 14% smaller than those of the Au NPs in the homo-P4VP. In both cases, the values of V_T of these composites increased linearly upon increasing the interparticle distance, because the pathway of collective electron transport increases with respect to the interparticle distance (see inset of Figure 4-2d).^[124]

Figure 4-3a displays one-dimensional small-angle X-ray scattering patterns (SAXS) of (Au NPs/P4VP)-*b*-PS obtained using synchrotron radiation. The scattering maxima, which are denoted by the letter “i” ($i = 1$), are form factor peaks associated with scattering from the isolated spherical domains. The form factor peaks shifted slightly to lower values of Q as the amount of incorporated Au increased,

which indicates that the volume or size of the Au NPs/P4VP composite domains increased. The average diameter of the P4VP domains of pure PS-*b*-P4VP, deduced from the positions of the form factor maxima, was 26.6 nm. The average diameters, measured by their volume, for the 10, 15, 26, 33, and 48% Au NPs in the P4VP block were 27.3, 27.8, 28.6, 29.3, and 30.2 nm, respectively, assuming that the density of P4VP and Au remained the same before and after mixing. The inset of Figure 4-3a lists the free volume per Au particle in a single P4VP domain (V_{free}), which is defined by the average volume of an occupied Au particle and can be estimated using Eqs. (4-3) and (4-4):

$$\frac{V_{Au/P4VP} - V_{P4VP}}{V_{Au}} = n \quad (4-3)$$

$$\frac{V_{Au/P4VP}}{n} = V_{free} \quad (4-4)$$

where $V_{Au/P4VP}$ is the volume of a single Au NPs/P4VP composite domain, V_{P4VP} is the volume of a single P4VP domain, V_{Au} is the volume of a Au NP, and n is the maximum number of Au NPs in a single P4VP domain. The edge-to-edge interparticle distance (d) can be determined by assuming a cubic lattice model for the Au NPs. The values of d were calculated using Eq. (4-5) based on the cubic lattice model presented in Figure 4-3b.^[128]

$$d = L - 2r = (V_{free})^{1/3} - 2r \quad (4-5)$$

where r is the radius of the Au NPs. The value of d decreased when the amount of Au increased, as displayed in the inset of Figure 4-3b.

Figures 4-5a and 4-6a display the I - V characteristics, measured at 78 K, of monolayer (Au NPs/P4VP)-*b*-PS and Au NPs/homo-P4VP thin films, respectively, having various contents of Au. For the (Au NPs/P4VP)-*b*-PS samples, the current was assumed to flow through the Au/P4VP nanodomain, owing to the much higher

resistance of the PS phase. The conductivity of the Au NPs/P4VP composite increased monotonically when the amount of Au increased, both in the nanodomain-confined and randomly distributed samples. Figures 4-5b and 4-6b display representative I - V scaling data, recorded at 78 K, for (Au NPs/P4VP)-*b*-PS and Au NPs/homo-P4VP thin films having various contents of Au. Table 4-1 provides details regarding the fitting of the curves and the calculation of the threshold voltages and scaling exponents. The data in Figure 4-5b provide power-law scalings, ζ , for the 15, 26, 33, and 48% Au NPs of 1.42, 1.39, 1.32, and 1.31, respectively. These values indicate that the effect of nanodomain confinement for quasi-one-dimensional collective electron transport for Au NPs in a nanodomain decreases when the number of Au NPs decreases. The data in Figure 4-6b provide power-law scalings, ζ , for the 15, 26, 33, and 48% Au NPs of 2.89, 2.89, 2.87, and 2.84, respectively. These values indicate that the dimensionality for collective electron transport in the randomly distributed sample is independent of the number of Au NPs; i.e., quasi-three-dimensional collective electron transport occurs for the randomly distributed Au NPs.

4-4 Conclusions

We have demonstrated that the collective electron transport behavior between Au NPs confined within a single P4VP nanodomain is quasi one-dimensional, as opposed to the three-dimensional behavior displayed by Au NPs in homo-P4VP. The threshold voltage of these composite increased linearly upon increasing the inter-nanoparticle distance for both the nanodomain-confined and randomly distributed samples.

Scheme 4-1. Fabrication of a self-assembled (Au NPs/P4VP)-*b*-PS thin film through the selective incorporation of dispersed pre-synthesized Au NPs into P4VP domains.

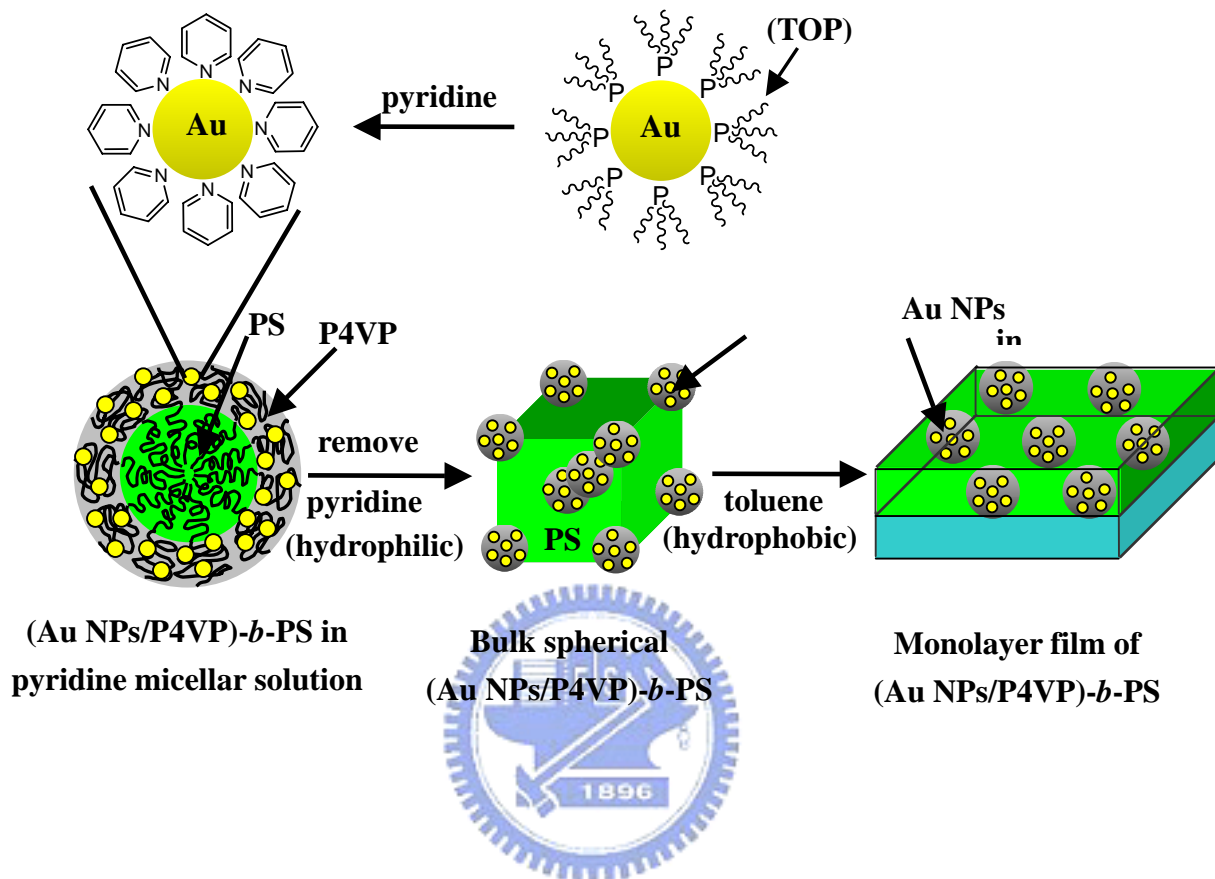
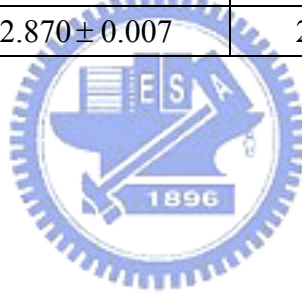


Table 4-1. Details of the Fitting of $I-V$ Curves, Measured at 78 K, for (Au NPs/P4VP)- b -PS and Au NPs/P4VP Thin Films Having Various Contents of Au NPs, and Determination of the Threshold Voltages and Scaling Exponents.

(Au NPs/P4VP)-b-PS $I = I_0 (V/V_T - 1)^\zeta$				
	48%	33%	26%	15%
I_0	$(2.32 \pm 0.55) \times 10^{-9}$	$(1.81 \pm 0.45) \times 10^{-9}$	$(7.82 \pm 0.85) \times 10^{-10}$	$(7.07 \pm 0.88) \times 10^{-10}$
V_T	0.299 ± 0.006	0.363 ± 0.007	0.429 ± 0.006	0.498 ± 0.007
ζ	1.312 ± 0.007	1.362 ± 0.008	1.395 ± 0.006	1.420 ± 0.009

Au NPs/P4VP $I = I_0 (V/V_T - 1)^\zeta$				
	48%	33%	26%	15%
I_0	$(4.38 \pm 0.67) \times 10^{-9}$	$(3.17 \pm 0.50) \times 10^{-9}$	$(1.30 \pm 0.39) \times 10^{-10}$	$(9.94 \pm 0.84) \times 10^{-10}$
V_T	0.349 ± 0.005	0.415 ± 0.006	0.489 ± 0.007	0.549 ± 0.007
ζ	2.846 ± 0.009	2.870 ± 0.007	2.893 ± 0.007	2.895 ± 0.008



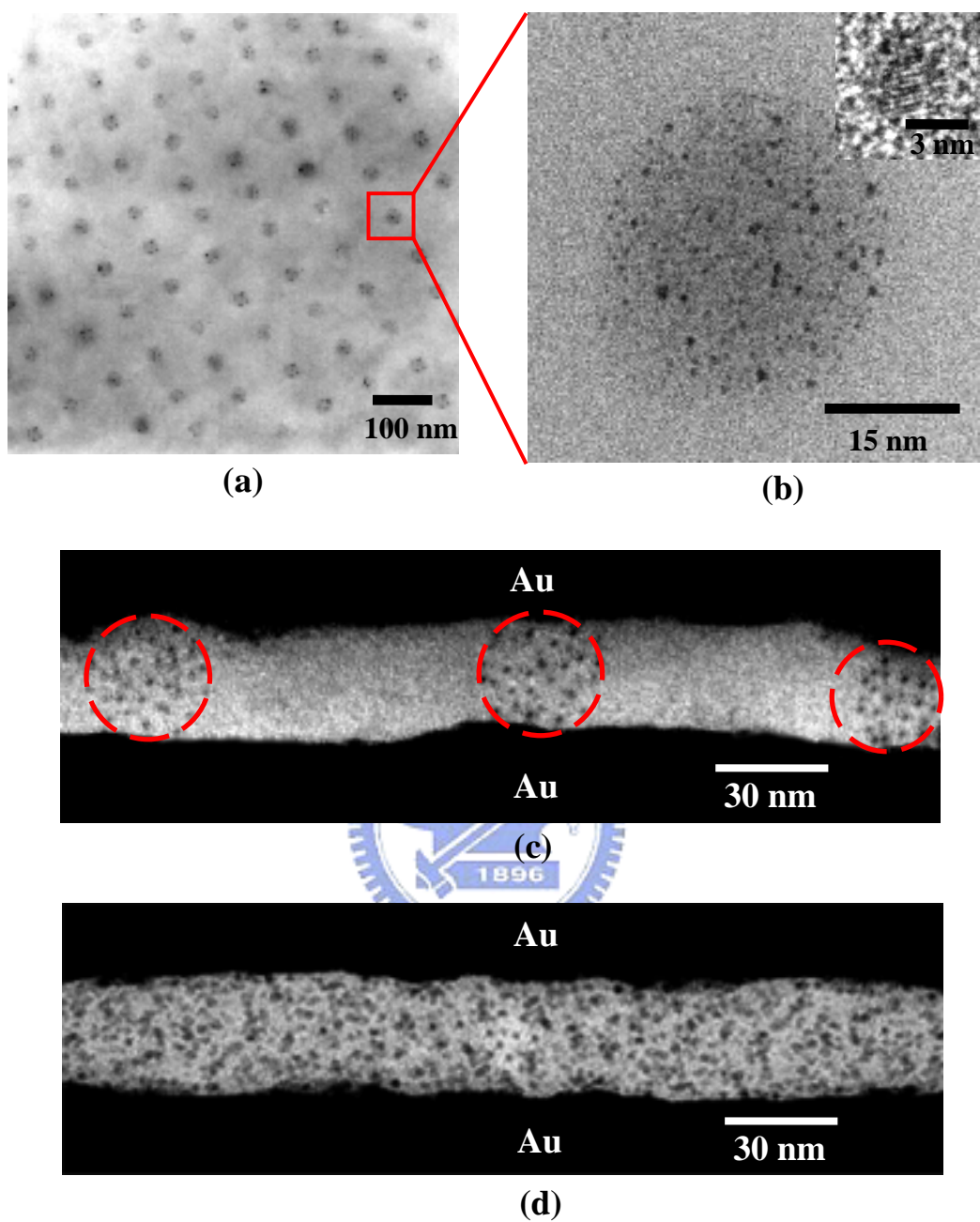
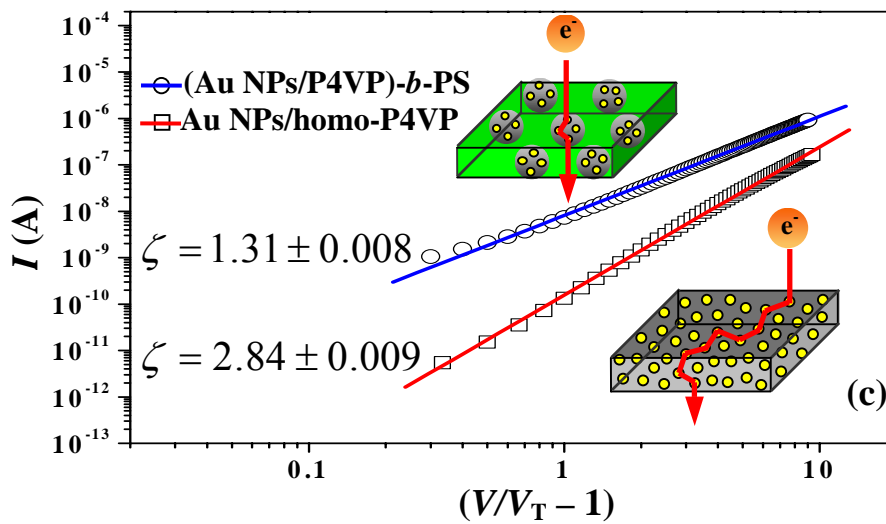
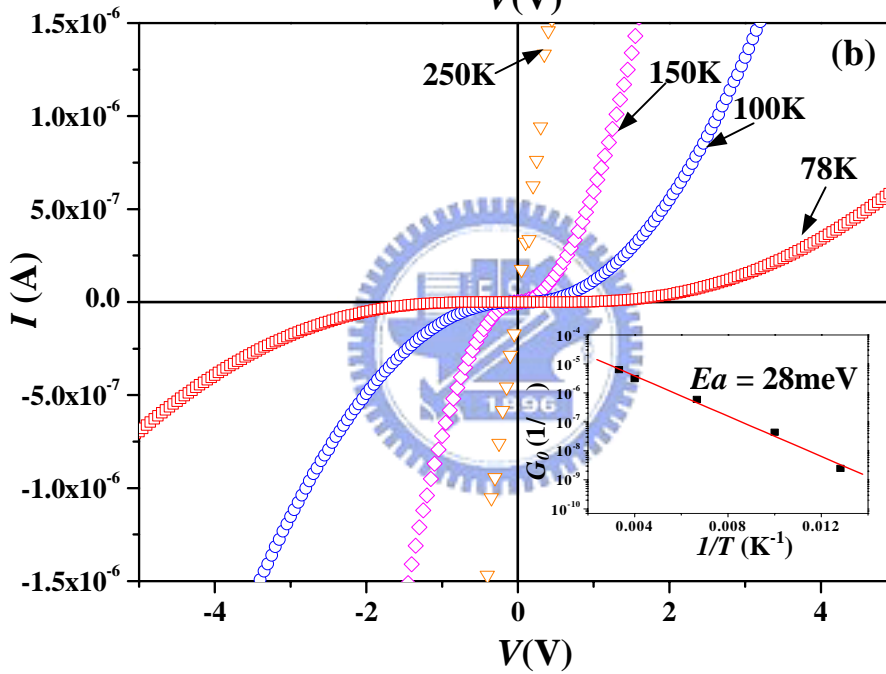
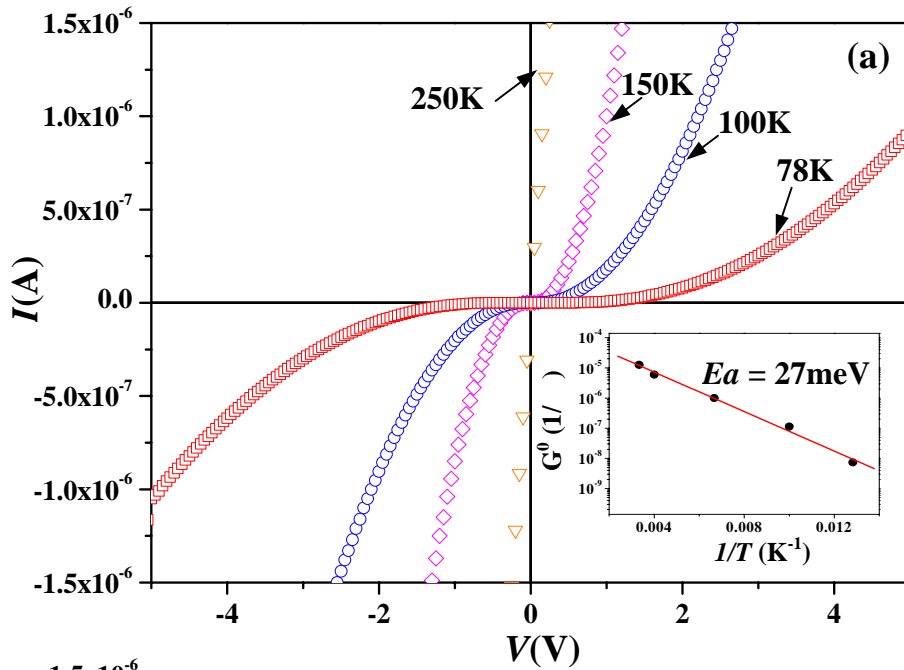


Figure 4-1 (a) Conventional, (b) high-resolution, and (c) cross-sectional TEM images, obtained without staining, of a thin film of 48% (Au NPs/P4VP)-*b*-PS. (d) Cross-sectional TEM image of a thin film of 48% Au NPs/homo-P4VP.



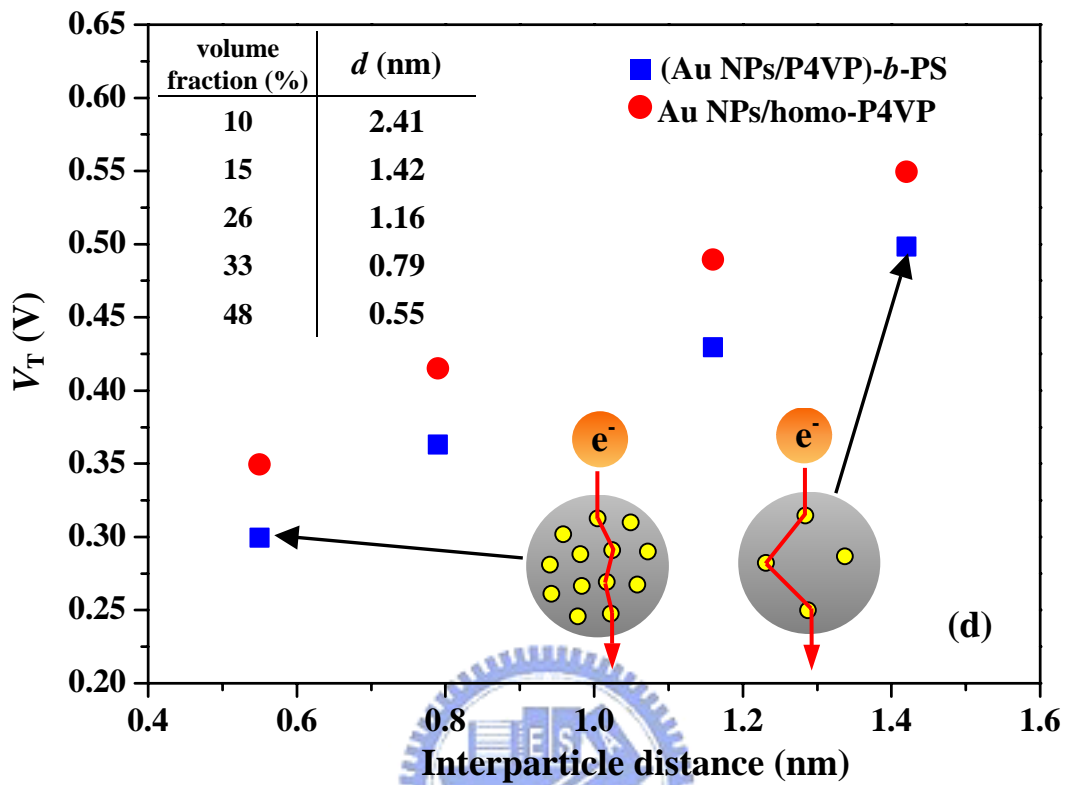


Figure 4-2 I - V curves of (a) 48% (Au NPs/P4VP)-*b*-PS and (b) Au NPs/homo-P4VP thin films measured at temperatures between 250 and 78 K. (c) Scaling behavior of the I - V curves of 48% (Au NPs/P4VP)-*b*-PS and Au NPs/homo-P4VP at 78 K. (d) Plots of V_T vs. d for the 48% (Au NPs/P4VP)-*b*-PS and Au NPs/homo-P4VP samples having various contents of Au NPs.

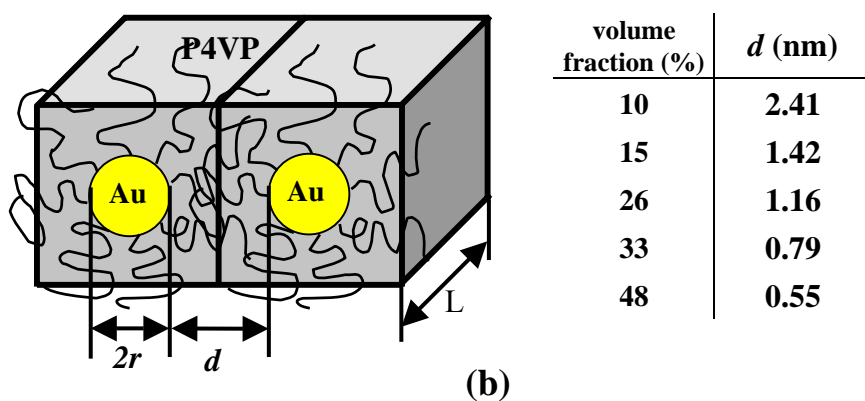
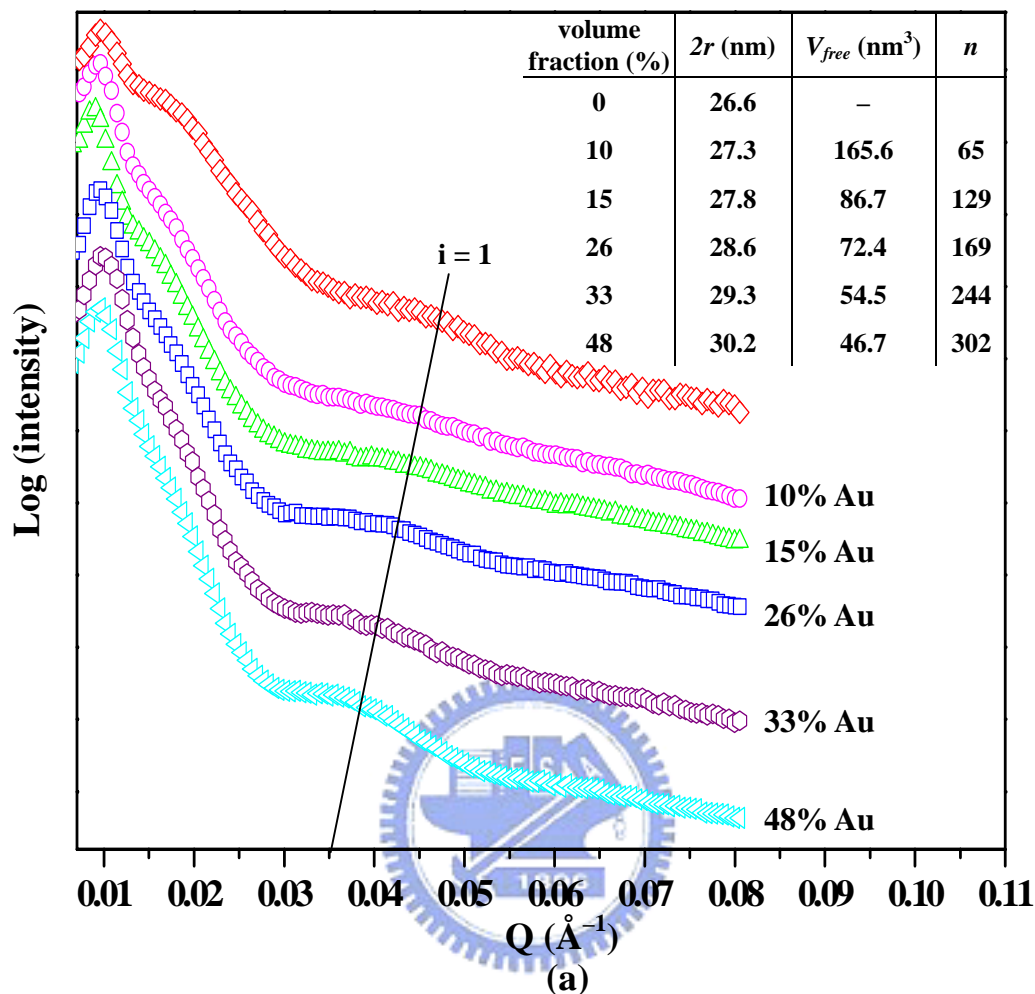


Figure 4-3 (a) Small-angle X-ray scattering of bulk (Au NPs/P4VP)-*b*-PS nanocomposites having various contents of Au NPs. (b) Schematic representation of the cubic lattice model for the free volume per Au nanoparticle in a single P4VP domain.

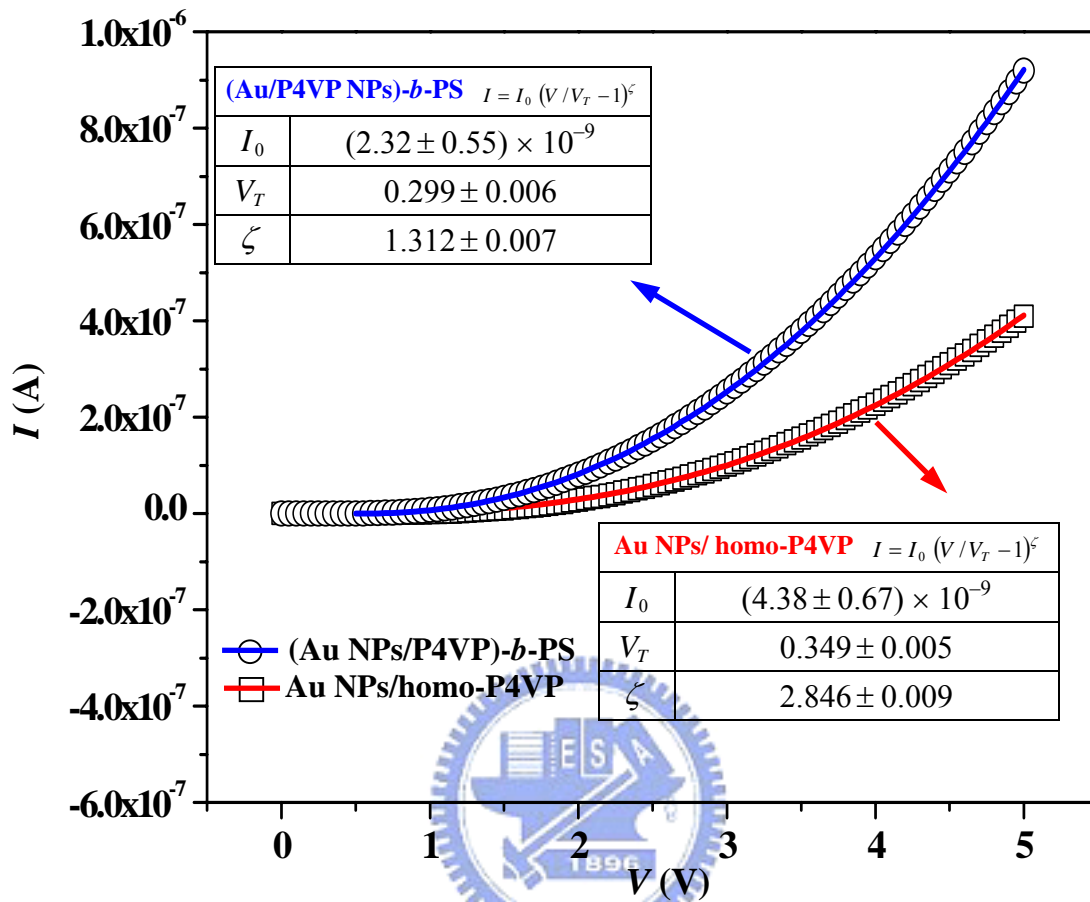


Figure 4-4 I - V Curves measured at 78 K for (Au NPs/P4VP)- b -PS and Au NPs/P4VP thin films. Details of the fitting and determination of the threshold voltages and scaling exponents are provided in the corresponding tables.

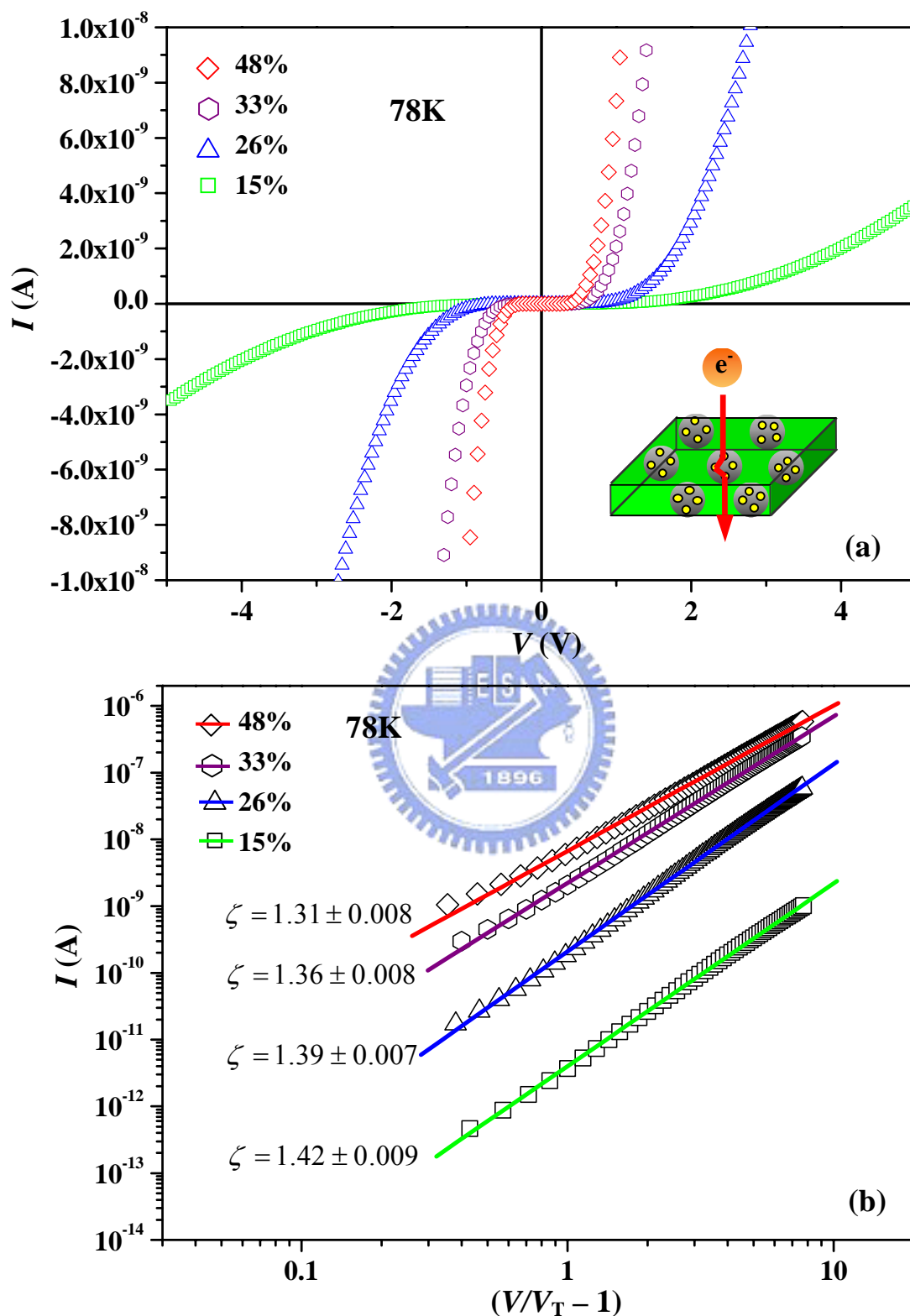


Figure 4-5 (a) I - V Curves, measured at 78 K, of (Au NPs/P4VP)- b -PS thin films having various contents of Au NPs. (b) Scaling behavior of the I - V curves of (Au NPs/P4VP)- b -PS having various contents of Au NPs at 78 K.

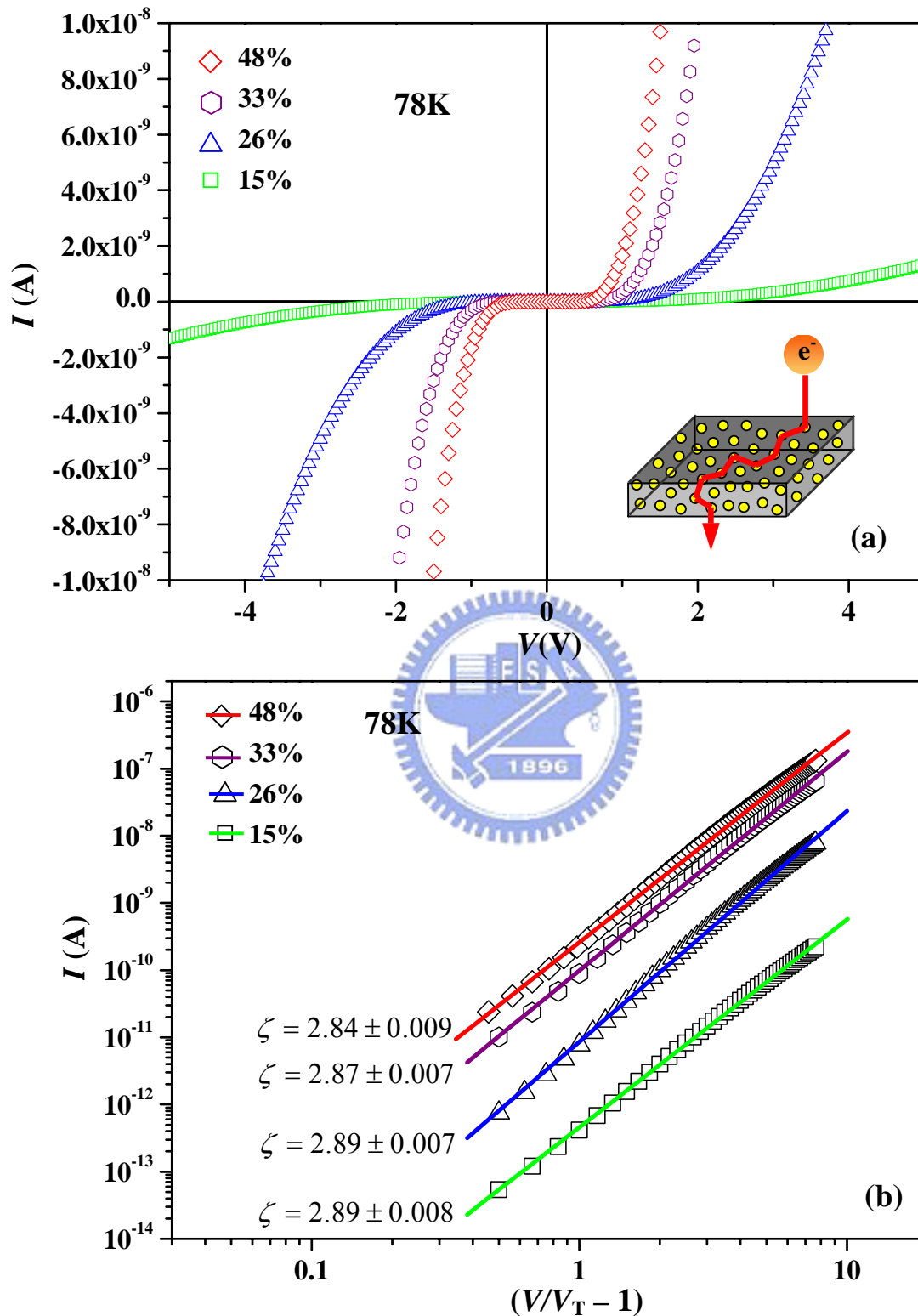


Figure 4-6 (a) I - V Curves, measured at 78 K, of Au NPs/homo-P4VP thin films having various contents of Au NPs. (b) Scaling behavior of the I - V curves of Au NPs/homo-P4VP having various contents of Au NPs at 78k.

Chapter 5: The Orientation of CdSe Nanorods Affects the Electron Mobility of CdSe/P4VP Nanodomains Self-Assembled within a Poly(styrene-*b*-4-vinylpyridine) Diblock Copolymer Thin Film

5-1 Introduction

Block copolymers are versatile platform materials because they can self-assemble—if they have appropriate compositions and are subjected to suitable conditions—into various nanostructures having period thicknesses between 10 and 100 nm through microphase separation of incompatible blocks.^[129,130] Nanostructured block copolymers can be used as templates for selectively controlling the spatial position of semiconductor nanoparticles within one of the blocks.^[131–133] For example, the selective sequestrations of pre-synthesized CdS,^[20, 22, 134] CdSe,^[131c] and TiO₂^[91a] nanoparticles into one block of a diblock copolymers can be performed by ensuring the presence of strong interactions between that block and the surface ligands of the nanoparticles. Block copolymers can also be used as nanoreactors for the synthesis of nanomaterials. For example, quasi-regular arrays of Au clusters^[133a] and TiO₂ needles^[36] have been obtained through the selective sequestration of metal ions into one block of poly(styrene-*b*-vinylpyridine).

The unique optical and electrical properties of one-dimensional (1D) semiconductor nanostructures, such as nanorods (NRs) and nanowires (NWs), can be exploited for use in a number of applications, including solar cells, photonic crystals, lasers, transistors, and sensors.^[135, 136, 139a,b] To take full advantage of the material properties of these 1D nanostructures, they must be pre-aligned or ordered in some other way. Several physical and chemical strategies have been used for the alignment or ordering of arrays 1D nanostructures. Examples for in-plane two-dimensional (2D) arrays include the unidirectional alignment of CdSe NRs,^[137] the assembly of BaCrO₄ NR monolayers through the use of the Langmuir–Blodgett

technique,^[138] and the alignment of a liquid-crystalline phase of CdSe NRs through surface deposition.^[139c] For out-of-plane 2D arrays, some examples are the use of e-beam lithography to obtain arrays of CdSe pillars and TiO₂ nanoneedles through electrochemical deposition and solution crystal growth,^[140, 91b] and the preparation of a periodic array of uniform ZnO NWs through vapor phase transport and catalytic growth.^[141] Although there are many bottom-up growth techniques for preparing 1D nanostructures in the out-of-plane 2D arrays and many techniques for pre-synthesized NRs in the in-plane 2D arrays, finding techniques for arranging pre-synthesized NRs in out-of-plane 2D arrays remains a great challenge.

The powerful aligning force of an electric field can be used to manipulate the orientation of anisotropic materials by taking advantage of their different anisotropic dielectric constants. Examples of this approach include the alignment of ZnO NRs and Au NWs,^[142] the alignment of carbon nanotubes suspended in a columnar liquid-crystalline polymer melt,^[143] and the electrically induced sphere-to-cylinder transition and patterning in diblock copolymers films.^[144] In this present study, we applied an electric field to induce the orientation of CdSe NRs that had been self-assembled in the poly(4-vinylpyridine) (P4VP) nanodomains of a poly(styrene-*b*-4-vinylpyridine) (PS-*b*-P4VP) diblock copolymer thin film. We varied the number of CdSe nanorods incorporated in the P4VP nanodomains by controlling the strength of the polar interactions and the loading concentration. The electron mobilities and the electron barrier heights of the CdSe/P4VP nanodomains incorporating out-of-plane and in-plane CdSe nanorods were monitored.

5-2 Methods and Analysis

5-2-1 Materials. The poly(styrene-*b*-4-vinylpyridine) (S4VP) diblock copolymer was purchased from Polymer Source, Inc. The polydispersity index (M_w/M_n) was 1.07;

the molecular weights (M_n) of the PS and P4VP blocks were 557,000 and 75,000 g/mol, respectively. Cadmium oxide (CdO, 99.9%), selenium (Se, 99.9%, 100 mesh), and trioctylphosphine (TOP) were obtained from Aldrich. Trioctylphosphine oxide (TOPO), *n*-hexylphosphonic acid (HPA), and *n*-octadecylphosphonic acid (ODPA) were purchased from Lancaster. Heptane (99%, TEDIA USA), toluene (99%, TEDIA USA), methyl alcohol (MeOH, 99%, TEDIA USA), and pyridine (99%, Showa) were obtained from commercial sources.

5-2-2 Synthesis of CdSe/TOPO and CdSe/Pyridine NRs. CdSe/TOPO NRs were synthesized using a modification of a procedure reported previously.^[149] A mixture of CdO (51.3 mg), HPA (88 mg), ODPA (88 mg), and TOPO (1.2 g) was heated in a 25-mL three-neck flask at 275 °C under an argon flow to obtain a colorless, clear solution. At this temperature, the selenium solution was injected in two lots. First, a solution of Se (5.26 mg) and TOP (105 mg) in toluene (0.15 mL) was injected rapidly; then, a solution of Se (20.84 mg) in TOP (290 mg) was injected dropwise. The growth temperature was maintained at 275 °C for 60 s and then the reaction mixture was cooled to room temperature. The CdSe/TOPO rods were collected as powders after their precipitation with methanol. The CdSe/TOPO powder (30 mg) was dissolved in pyridine (5 mL) and then stirred at 65 °C for 6 h. Heptane (30 mL) was added to reprecipitate the CdSe/pyridine NRs.

5-2-3 Preparation of Bulk and Thin Films of (CdSe/P4VP)-*b*-PS. PS-*b*-P4VP (0.05 g) was added to pyridine (1 mL). Samples of 33, 40, 48, 55, and 65% CdSe/pyridine (with respect to the volume fraction of P4VP block) were mixed in the PS-*b*-P4VP/pyridine polymerization solution. These mixtures were dried slowly under vacuum at 50 °C and then maintained at 160 °C for 72 h to obtain the bulk (CdSe/P4VP)-*b*-PS composites. Micellar solutions (0.5 wt%) of (CdSe/P4VP)-*b*-PS were prepared by dissolving bulk (CdSe/P4VP)-*b*-PS in toluene prior to the

preparation of thin films.

5-2-4 Orientation of CdSe Nanorods in P4VP Domains Under an Electric Field.

Samples of the micellar solutions of 33, 40, 48, 55, and 65% (CdSe/P4VP)-*b*-PS in toluene were spin-coated at 5000 rpm for 60 s onto Pt-coated silicon wafer; an aluminized Kapton film comprised the top electrode for electric field. The applied electric field was 12 V/ μm and the temperature was 160 °C.

5-2-5 Characterization. TEM images were obtained using a JOEL-2010 transmission electron microscope. For TEM analysis, the thin film sample spin-coated on a carbon-coated silicon wafer was removed from the wafer using 1% HF. The electric field was supplied using an AF-30R1 high-voltage power supply. SEM images were obtained using a thermal field emission scanning electron microscope (JSM-6500F) operated at an accelerating voltage of 15 kV. The current-voltage (*I*-*V*) characteristics of the devices containing thin films of (CdSe/P4VP)-*b*-PS were measured using a Hewlett-Packard 4156B instrument. Using a base pressure below 1×10^{-6} Torr, a layer of Al (200 nm) was vacuum-deposited to act as the top electrode.

5-3 Results and Discussions

Scheme 5-1 illustrates the process we used to prepare a monolayered (CdSe/P4VP)-*b*-PS thin film. Pyridine-modified CdSe NRs and PS-*b*-P4VP block copolymer were dissolved and mixed in pyridine; the CdSe NRs were distributed selectively in the P4VP phase as a result of their preference for experiencing polar interactions. Subsequently, toluene, which is a good solvent for PS, but a poor one for P4VP, was added to form a solution containing micelles having CdSe/P4VP cores and PS shells. Figure 5-1 displays TEM images of the P4VP domains of PS-*b*-P4VP samples containing different amounts of CdSe NRs. The dark regions represent the

CdSe NRs (because of the high electron density of cadmium). The orientation of these CdSe NRs was largely in the plane direction of the PS-*b*-P4VP film. The inter-domain distance of CdSe/P4VP domains was ca. 90 nm. In Figures 5-1a and 5-1b, where the loading concentrations of CdSe NRs were 65 and 48%, respectively, the average number of NRs incorporated within single P4VP nanodomains were ca. five and three, respectively. When the loading amount was 33%, some individually distinct CdSe nanorods were incorporated into the P4VP nanodomains (Figure 5-1c).

Figure 5-2a displays an SEM image of the tilted substrate of an as-prepared 33% (CdSe/P4VP)-*b*-PS thin film. Some small islands (diameters: ca. 30 nm), which represent the CdSe/P4VP domains, appear because the CdSe NRs were not totally horizontally aligned with respect to the substrate and because their lengths (50 nm) were slightly larger than the size of the P4VP domain. Figure 5-2b presents an SEM image of the tilted substrate of a 33% (CdSe/P4VP)-*b*-PS thin film after it had experienced an applied electric field of 12 V/μm at 160 °C under vacuum for 24 h. The protruded CdSe NRs appear to be oriented by ca. 65° with respect to the plane of the P4VP-*b*-PS thin film. The applied electric field induced charge separation and the resulting polarization generated a net dipole moment, which aligned the long axes of the CdSe NRs parallel to the applied electric field. The force on the nanorods in an electric field is expressed to a good first approximation by Eq. (5-1):^[145]

$$f = \vec{P} \cdot \partial \vec{E} / \partial r = (\varepsilon - 1) \cdot \partial (|\vec{E}|^2) / 8\pi \partial r \quad (5-1)$$

where f is the force per unit volume, \vec{P} is the polarization, \vec{E} is the electric field strength, and ε is the dielectric constant. Because the dielectric constant of the long axis ($\varepsilon = 10.2$) of a CdSe NR is larger than that of the short axis ($\varepsilon = 9.33$),^[146] the induced force along the long axis is larger than that along the short axis; thus, the long axis of the CdSe NR tends to align parallel to the applied electric field

more so than does its short axis. The orientations (equilibrium angles) of the CdSe nanorods appear to be determined by both the induced polarization force on the nanorods and the viscous force of the P4VP domain surrounding them. The critical field strength where the alignment can be turned on and off was $12 \text{ V}/\mu\text{m}$ (Figure 5-5). The states of the (CdSe/P4VP)-*b*-PS thin films before and after applying the electric field was shown in Scheme 5-1.

Figure 5-3a displays a cross-sectional TEM image of a 33% (CdSe/P4VP)-*b*-PS thin film prior that had not been subjected to an applied electric field. The dark regions at the top and bottom of this image are the Al and Pt electrodes; the lighter region is the domain of the CdSe/P4VP composite. The dark rods are the CdSe NRs, which were aligned horizontally with respect to the electrodes. Because the CdSe NRs were not aligned completely parallel to the *x*-axis, their observed lengths are not their true lengths. The distance from the side surface of the CdSe NR to the surface of the Al electrode and to the Pt electrode was ca. 13 nm. Figure 5-3b displays a cross-sectional TEM image of a 33% (CdSe/P4VP)-*b*-PS thin film that had been subjected to an applied electric field. A micellar solution of 33% (CdSe/P4VP)-*b*-PS in toluene was spin-coated at 5000 rpm for 60 s on Pt-coated Kapton; an aluminized Kapton film comprised the top electrode for the applied electric field. After applying the electric field, the aluminized Kapton film was removed and a layer of Al (200 nm) was vacuum deposited as the top electrode. The sandwiched sample was placed into an epoxy capsule, which was cured at 70 °C for 48 h in a vacuum oven. The cured epoxy samples were microtomed using a Leica Ultracut Uct into ca. 90-nm-thick slices. In the image, the dark bars are the CdSe NRs; their angle of orientation was ca. 65°. These NRs were ca. 50 nm long and 5 nm wide. The distance between the Al electrode and the CdSe NR was ca. 8 nm; the CdSe NR was much closer to the Pt electrode. The insets of Figures 5-3a and 5-3b present the

HRTEM lattice images of CdSe NRs incorporated within single nanodomains of (CdSe/P4VP)-*b*-PS in the absence and presence of the electric field, respectively. The orientation of these wurtzite CdSe NRs is along the [00*l*] direction, with a spacing between adjacent (002) lattice planes of ca. 3.5 Å.

Figure 5-4 displays the averaged current density–electric field (J–E) curves of a single CdSe/P4VP nanodomain in a PS matrix incorporating various contents of out-of-plane and in-plane CdSe NRs. These plots were obtained and derived from measurements of a device sandwiched between a Pt-coated Si wafer (bottom electrode) and an Al film (top electrode). We assume that the current flowed through the CdSe/P4VP nanodomain, because of the much higher resistance of the PS phase. The current density of a single nanodomain can, therefore, be calculated from the density of the CdSe/P4VP nanodomain in the PS phase by using the following parameters obtained from the TEM image: the area of the Al electrode was $1.96 \times 10^{-3} \text{ cm}^2$ and the density of the CdSe/P4VP nanodomain in the PS phase was $3.1 \times 10^9 \text{ cm}^{-2}$. The number of CdSe/P4VP nanodomains under the Al electrode—i.e., the product of the area of the Al electrode and the density of CdSe/P4VP nanodomains—is ca. 6×10^6 . The value of J is obtained by dividing the current first by the number of CdSe/P4VP nanodomains and then by its area. The zero-current regions arise from electron tunneling from the Al electrode through the P4VP surrounding the CdSe NRs and to the conduction band of the CdSe NRs, which must overcome the barrier height (ϕ_e) of the P4VP between the electrode and CdSe. A tunneling process can be modeled accurately using the Fowler–Nordheim (FN) equation, which can be expressed as Eq. (5-2).^[147]

$$J(E) = \frac{A_{\text{eff}} q^3 E^2 m}{8\pi h \phi_e m^*} \exp \left[\frac{-8\pi \sqrt{2m^*} \phi_e^{3/2}}{3h q E} \right] \quad (5-2)$$

where A_{eff} is the effective contact area, E is the applied electric field, ϕ_e is the electron barrier height, and q , m^* , m , and h are the electron's charge and effective mass, free electron mass, and Planck's constant, respectively. By fitting the zero-current regions of the J–E curves to the FN theory, we obtained the values of ϕ_e that are presented in Table 5-1. The electron barrier height from the electrode to the nanodomain decreased monotonically when the amount of CdSe increased in both the out-of-plane and in-plane cases, owing to the fact that the distance between the Al electrode and CdSe NRs decreased at higher densities of CdSe NRs. The electron barrier heights in the out-of-plane cases were lower than those in the in-plane cases because the distance between the Al electrode and the CdSe NR was smaller in the out-of-plane case (Fig. 5-3c). With regard to the electron mobility in the higher-electric-field region, the J–E curve can be described using a space charge limited current (SCLC) model, which can be expressed as Eq. (5-3):^[148]

$$J = \frac{9}{8} \varepsilon \varepsilon_0 \mu(E) \frac{E^2}{L} = \frac{9}{8} \varepsilon \varepsilon_0 \mu_0 \exp(\sqrt{E/E_0}) \frac{E^2}{L} \quad (5-3)$$

where ε is the dielectric constant, ε_0 is the vacuum permittivity, μ is the field-dependent electron mobility, L is the thickness, μ_0 is the zero-field mobility, and E_0 is the field coefficient. By fitting the higher-electric-field regions of the J–E curves to this SCLC model, we obtained the values of μ_0 and E_0 presented in Table 5-1. For both the out-of-plane and in-plane cases, the electron mobility increased monotonically when the amount of CdSe increased because the distance between the CdSe NRs decreased at higher densities of CdSe NRs. The electron mobilities in the out-of-plane cases were ca. eight times larger than those of the in-plane cases because the CdSe NRs were much closer to the Pt electrode in the former system (Fig. 5-3c). Because the value of E_0 is material-dependent, these two cases provide similar values.

5-4 Conclusions

In conclusion, we have aligned CdSe nanorods that self-assembled in the P4VP nanodomains of a PS-*b*-P4VP diblock copolymer thin film through the use of polarization forces created by an applied electric field. The electron mobilities of the CdSe/P4VP nanodomains in the out-of-plane cases were ca. eight times larger than those in the in-plane cases. In both in the out-of-plane and in-plane cases, the electron mobility increased upon increasing the number of CdSe nanorods. The height of the electron barrier from the Al electrode to the nanodomain in the out-of-plane case was much smaller than that in the in-plane case; in both the out-of-plane and in-plane cases, the barrier height decreased upon increasing the number of CdSe nanorods.



Scheme 5-1: Fabrication of a self-assembled (CdSe/P4VP)-*b*-PS thin film through the selective incorporation of dispersed pre-synthesized CdSe NRs into P4VP domains.

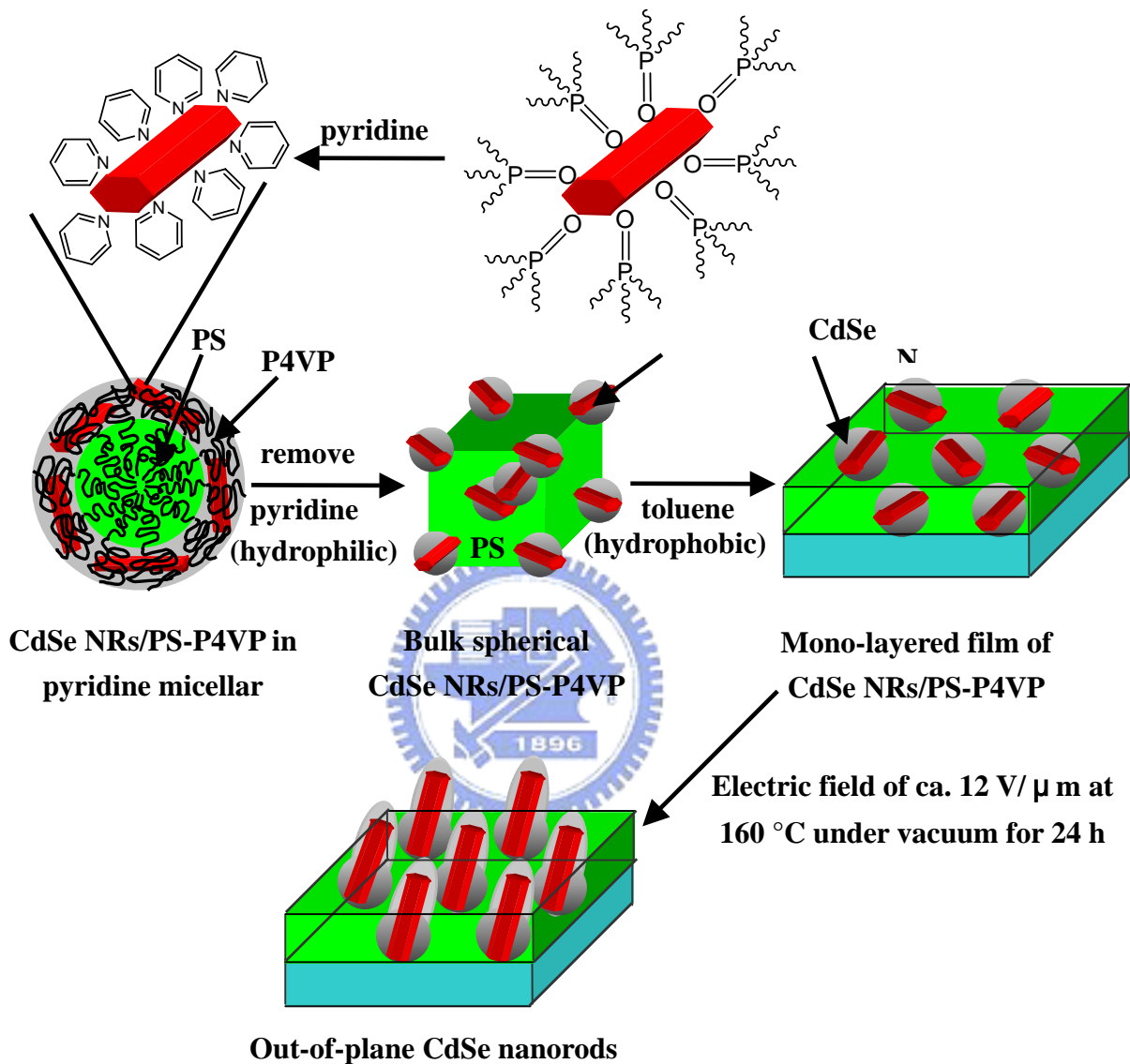
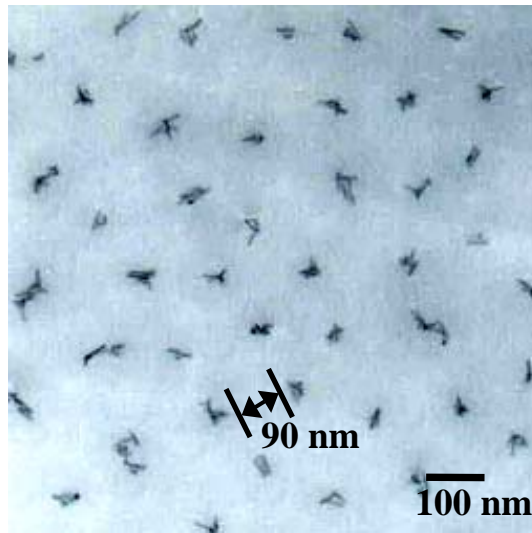


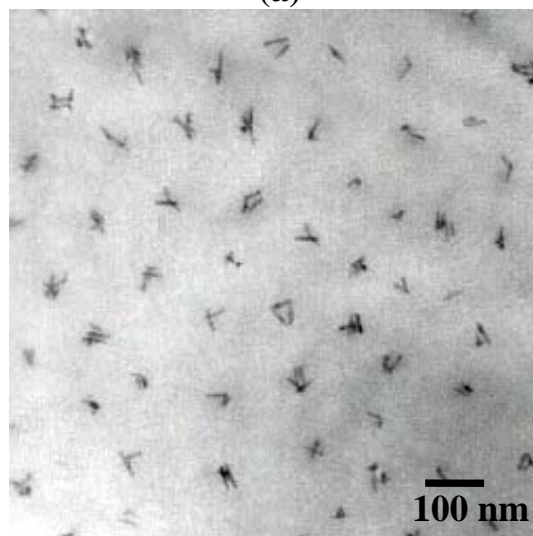
Table 5-1: Electron barrier heights (ϕ_e), electron mobilities (μ_0), and field coefficients (E_0) for in-plane and out-of-plane CdSe NRs incorporated within P4VP nanodomains in a PS matrix.

vol% of CdSe in P4VP	In-plane			Out-of-plane		
	$\phi_e \times (m/m^*)^{-1/3}$ (eV)	$\mu_0 \times 10^4$ (cm ² /Vs)	$E_0 \times 10^{-4}$ (V/cm)	$\phi_e \times (m/m^*)^{-1/3}$ (eV)	$\mu_0 \times 10^4$ (cm ² /Vs)	$E_0 \times 10^{-4}$ (V/cm)
33	1.66	1.2	5.8	1.45	9.3	6.2
40	1.54	4.1	5.6	1.35	32.3	5.8
48	1.43	17.6	6.1	1.21	141.5	5.6
55	1.37	31.1	5.9	1.16	248.4	6.3
65	1.29	90.2	5.7	1.05	723.2	5.9

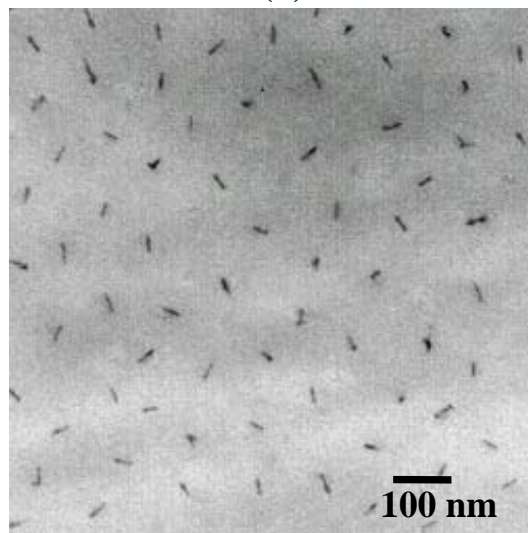




(a)

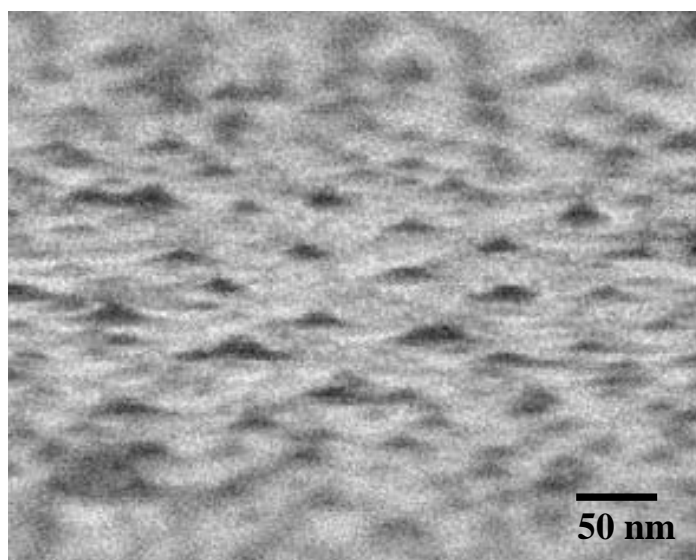


(b)

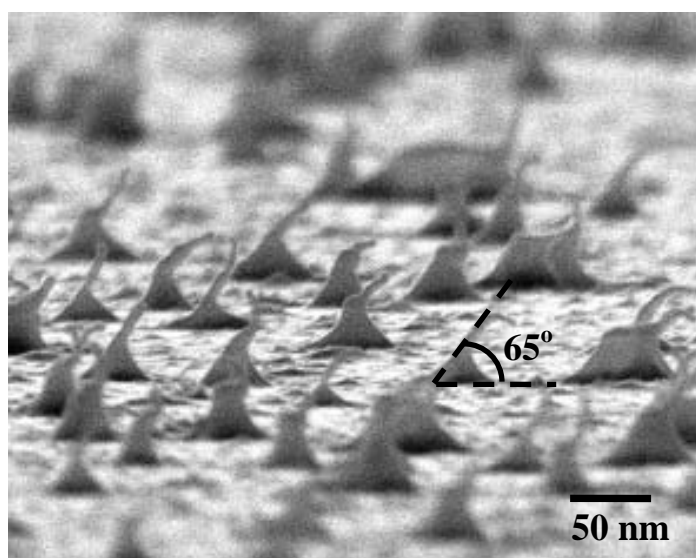


(c)

Figure 5-1 TEM images, obtained without staining, of thin films of (a) 65%, (b) 48%, and (c) 33% (CdSe/P4VP)-*b*-PS.

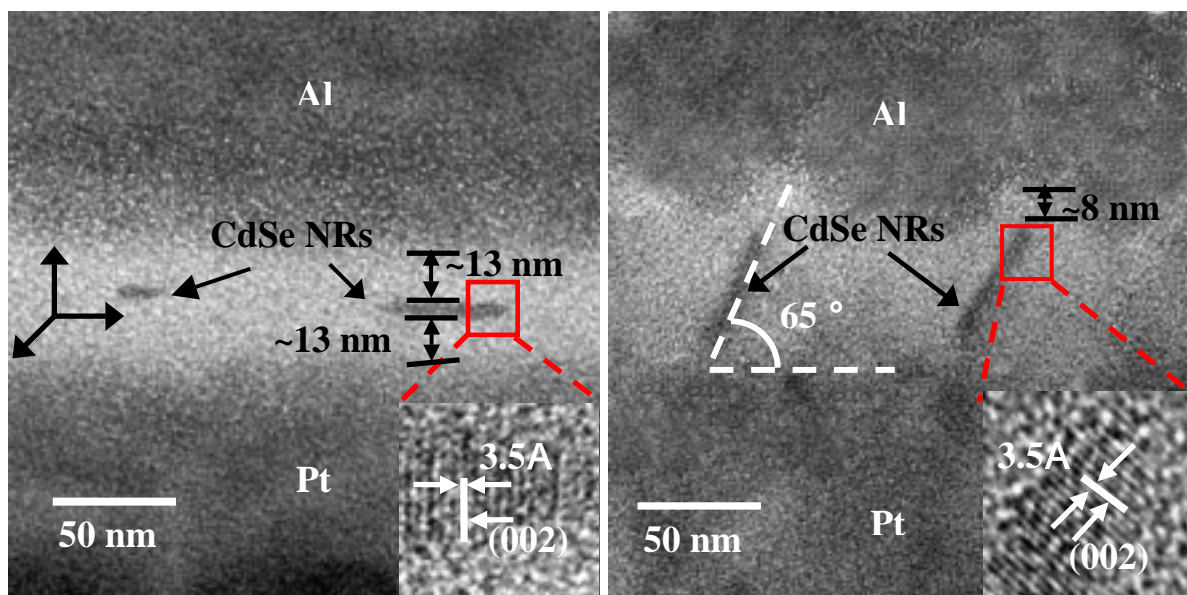


(a)



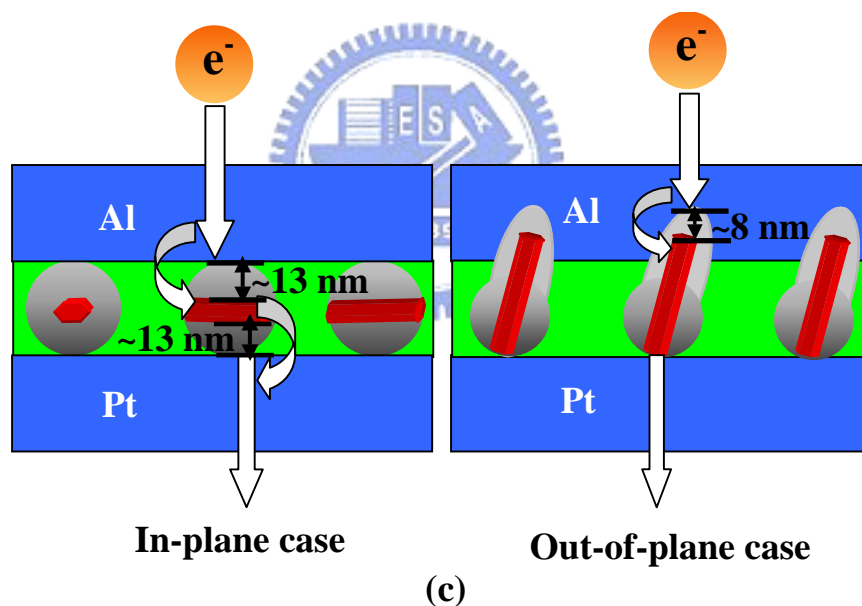
(b)

Figure 5-2 SEM images of 33% (CdSe/P4VP)-*b*-PS thin films prepared (a) in the absence and (b) in the presence of an applied electric field.



(a)

(b)



In-plane case

Out-of-plane case

(c)

Figure 5-3 Cross-sectional TEM images of 33% (CdSe/P4VP)-*b*-PS thin films prepared (a) in the absence of and (b) in the presence of an applied electric field. The insets display the respective HRTEM lattice images of a CdSe NR incorporated within a single P4VP nanodomain of (CdSe/P4VP)-*b*-PS. (c) A schematic depiction of the electron transport process.

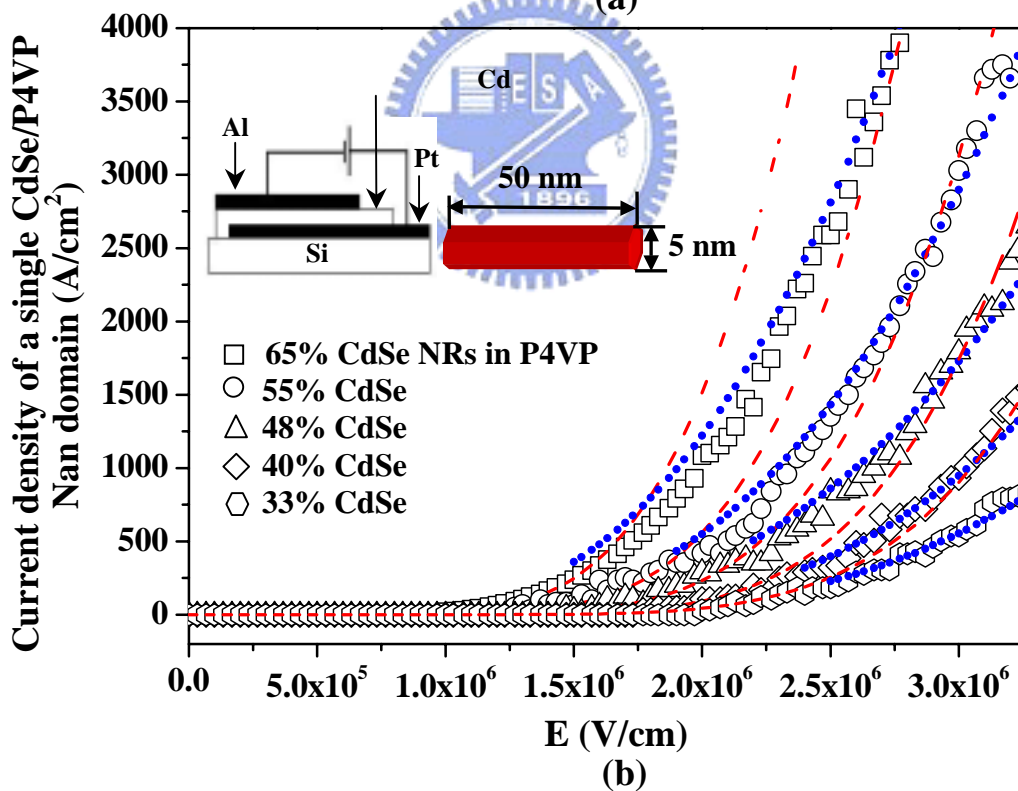
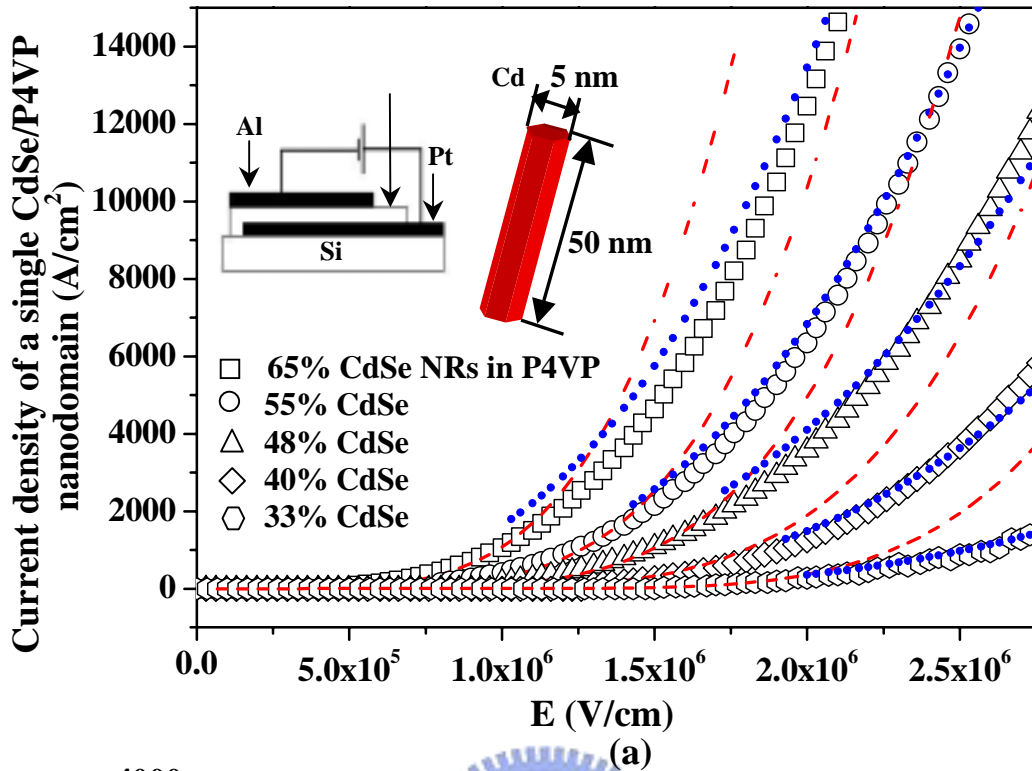


Figure 5-4 Averaged current density–electric field (J – E) curves of a single CdSe/P4VP nanodomain in a PS matrix incorporating various contents of (a) out-of-plane and (b) in-plane CdSe NRs. The dashed lines denote best fits to the FN equation; the dotted lines denote best fits to the SCLC model, which includes the field-dependent mobility.

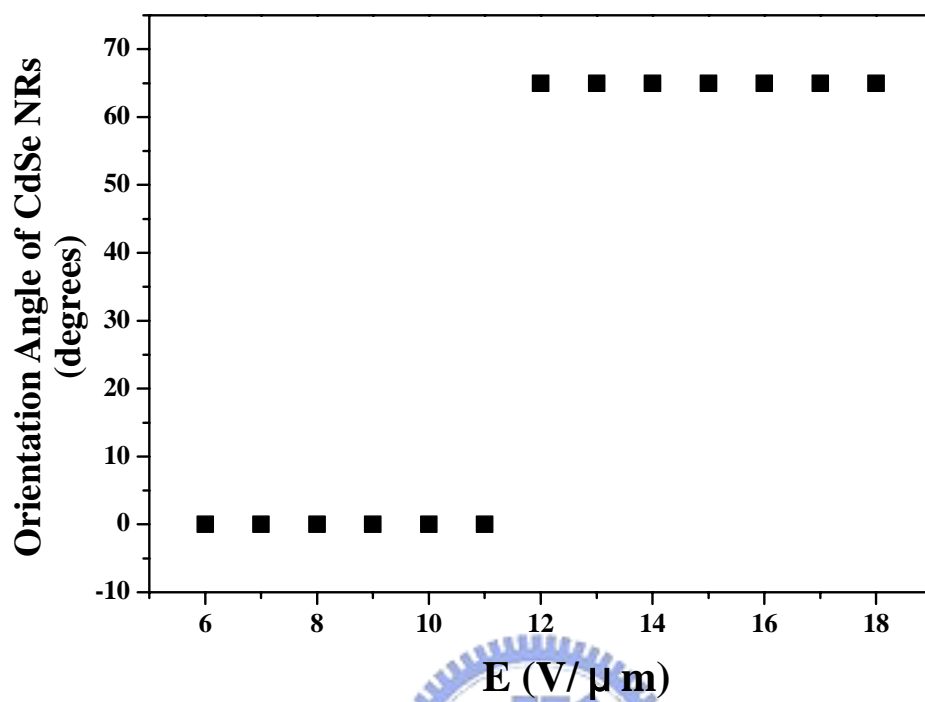


Figure 5-5: Orientation angle of the protruded CdSe NRs with respect to the plane of the P4VP-*b*-PS thin film as function of the electric field strength.

Chapter 6 Conclusions

In the (CdSe QDs/P4VP)-*b*-PS case, we have demonstrated that the electron tunneling rate constant in the case of CdSe QDs confined in a P4VP nanodomain is much larger than in the randomly distributed case and it increases upon increasing the amount of CdSe. The value of electron tunneling coefficient of the CdSe-P4VP-CdSe system is 0.3 \AA^{-1} . The electron barrier height from the tip of the probe to the nanodomain decreased monotonically and the conductivity of the CdSe/P4VP nanodomain increased, following a percolation model, as the amount of CdSe increased.

In the (Au NPs/P4VP)-*b*-PS case, we have demonstrated that the collective electron transport behavior between Au NPs confined within a single P4VP nanodomain is quasi one-dimensional, as opposed to the three-dimensional behavior displayed by Au NPs in homo-P4VP. The threshold voltage of these composite increased linearly upon increasing the inter-nanoparticle distance for both the nanodomain-confined and randomly distributed samples.

In the (CdSe NRs/P4VP)-*b*-PS case, we have aligned CdSe nanorods that self-assembled in the P4VP nanodomains of a PS-*b*-P4VP diblock copolymer thin film through the use of polarization forces created by an applied electric field. The electron mobilities of the CdSe/P4VP nanodomains in the out-of-plane cases were ca. eight times larger than those in the in-plane cases. In both in the out-of-plane and in-plane cases, the electron mobility increased upon increasing the number of CdSe nanorods. The height of the electron barrier from the Al electrode to the nanodomain in the out-of-plane case was much smaller than that in the in-plane case; in both the out-of-plane and in-plane cases, the barrier height decreased upon increasing the number of CdSe nanorods.

Chapter 7 References

- [1] F. S. Bates and G. H. Fredrickson *Annu. Rev. Phys. Chem.* **1990**, *41*, 525.
- [2] I. W. Hamley *The Physics of Block Copolymers* (Oxford: Oxford University Press) **1998**.
- [3] N. Hadjichristidis, S. Pispas and G. Floudas *Block Copolymers. Synthetic Strategies, Physical Properties and Applications* (New York: Wiley), **2003**.
- [4] M. W. Matsen *J. Phys.: Condens. Matter* **2001**, *14*, R21.
- [5] I. W. Hamley *J. Phys.: Condens. Matter* **2001**, *13*, R643.
- [6] F. S. Bates and G. H. Fredrickson *Phys. Today* **1999**, *52*, 32.
- [7] F. Drolet and G. H. Fredrickson *Phys. Rev. Lett.* **1999**, *83*, 4317.
- [8] M. Lazzari, M. A. Lopez-Quintela *Adv. Mater.* **2003**, *15*, 1583.
- [9] C. Park, J. Yoon, E. L. Thomas *Polymer* **2003**, *44*, 6725.
- [10] M. Park, C. Harrison, P. M. Chaikin, R. A. Register and D. H. Adamson *Science* **1997**, *276*, 1401.
- [11] C. Harrison, M. Park, P. M. Chaikin, R. A. Register and D. H. Adamson *J. Vac. Sci. Technol. B* **1998**, *16*, 544.
- [12] C. Harrison, M. Park, R. A. Register, D. Adamson, P. Mansky and P. M. Chaikin *US Patent Specification* **1999**, 5948470.
- [13] M. Park, P. M. Chaikin, R. A. Register and D. H. Adamson *Appl. Phys. Lett.* **2001**, *79*, 257.
- [14] J. Y. Cheng, C. A. Ross, V. Z.-H. Chan, E. L. Thomas, R. G. H. Lammertink and G. J. Vancso *Adv. Mater.* **2001**, *13*, 1174.
- [15] T. Thurn-Albrecht, J. Schotter, G. A. K̄astle, N. Emley, T. Shibauchi, L. Krusin-Elbaum, K. Guarini, C. T. Black, M. T. Tuominen and T. P. Russell *Science* **2000**, *290*, 2126.
- [16] E. Jeoung, T. H. Galow, J. Schotter, M. Bal, A. Ursache, M. T. Tuominen, C. M.

- Stafford, T. P. Russell and V. M. Rotello *Langmuir* **2001**, *17*, 6396.
- [17] K. Liu, S. M. Baker, M. Tuominen, T. P. Russell and I. K. Schuller *Phys. Rev. B* **2001**, *63*, 060403(R).
- [18] S. W. Yeh, K. H. Wei, Y. S. Sun, U. S. Jeng, K. S. Liang, *Macromolecules* **2005**, *38*, 6559.
- [19] C. C. Weng and K. H. Wei, *Chem. Mater.* **2003**, *15*, 2936.
- [20] S. W. Yeh, K. H. Wei, Y. S. Sun, U. S. Jeng, K. S. Liang, *Macromolecules* **2003**, *36*, 7903.
- [21] U. S. Jeng, Y. S. Sun, H. Y. Lee, C. H. Hsu, and K. S. Liang, S. W. Yeh, K. H. Wei, *Macromolecules* **2004**, *37*, 4617.
- [22] S. W. Yeh, Y. T. Chang, C. H. Chou and K. H. Wei, *Macromolecular Rapid Communications* **2004**, *25*, 1679.
- [23] S. W. Yeh, T. L. Wu, K. H. Wei, Y. S. Sun, and K. S. Liang, *J. Polym. Sci. B Polym. Phys.* **2005**, *43*, 1220.
- [24] S. W. Yeh, T. L. Wu and K. H. Wei, *Nanotechnology* **2005**, *16*, 683.
- [25] Y. Lin, A. Boker, J. He, K. Sill, H. Xiang, C. Abetz, X. Li, J. Wang, T. Emrick, S. Long, Q. Wang, A. Balazs, T. P. Russell *Nature* **2005**, *434*, 55.
- [26] M. R. Bockstaller, Y. Lapetnikov, S. Margel, E. L. Thomas *J. Am. Chem. Soc.* **2003**, *125*, 5276.
- [27] J. J. Chiu, B. J. Kim, E. J. Kramer, D. J. Pine, *J. Am. Chem. Soc.* **2005**, *127*, 5036.
- [28] S. Forster and M. Antonietti *Adv. Mater.* **1998**, *10*, 195.
- [29] R. E. Cohen *Curr. Opin. Solid State Mater. Sci.* **1999**, *4*, 587.
- [30] M. V. Seregina, L. M. Bronstein, O. A. Platonova, D. M. Chernyshov, P. M. Valetsky, J. Hartmann, E. Wenz and M. Antonietti *Chem. Mater.* **1997**, *9*, 923.
- [31] L. M. Bronstein, S. N. Sidorov, P. M. Valetsky, J. Hartmann, H. Cölfen and M.

- Antonietti *Langmuir* **1999**, *15*, 6256.
- [32] M. Antonietti, E. Wenz, L. Bronstein and M. Seregina *Adv. Mater.* **1995**, *7*, 1000.
- [33] O. A. Platonova, L. M. Bronstein, S. P. Solodovnikov, I. M. Yanovskaya, E. S. Obolonkova, P. M. Valetsky, E. Wenz and M. Antonietti *Colloid Polym. Sci.* **1997**, *275*, 426.
- [34] B. H. Sohn and B. H. Seo *Chem. Mater.* **2001**, *13*, 1752.
- [35] J. Spatz, S. Mossmer, M. Moller, M. Kocher, D. Neher and G. Wegner *Adv. Mater.* **1998**, *10*, 473.
- [36] C. C. Weng, K. F. Hsu and K. H. Wei, *Chem. Mater.* **2004**, *16*, 4080.
- [37] A. C. Edrington *Adv. Mater.* **2001**, *13*, 421.
- [38] Y. Fink, A. M. Urbas, M. G. Bawendi, J. D. Joannopoulos and E. L. Thomas *J. Lightwave Technol.* **1999**, *17*, 1963.
- [39] M. Maldovan, A. M. Urbas, N. Yufa, W. C. Carter and E. L. Thomas *Phys. Rev. B* **2002**, *65*, 165123.
- [40] A. M. Urbas, M. Maldovan, P. DeRege and E. L. Thomas *Adv. Mater.* **2002**, *14*, 1850.
- [41] T. Hashimoto, K. Tsutsumi and Y. Funaki *Langmuir* **1997**, *13*, 6869.
- [42] A. P. Alivisatos, *Endeavour* **1997**, *21*, 56.
- [43] M. A. El-Sayed, *M. Acc. Chem. Res.* **2004**, *37*, 326.
- [44] H. S. Naiwa, Hitachi Research lab. *In Handbook of Nanostructure Materials and nanotechnology v4. Chapter 5*, **2000**.
- [45] Y. Wang and N. Herron *J. Phys. Chem.* **1991**, *95*, 525.
- [46] J. T. Hu, L. S. Li, W. D. Yang, L. Manna, L. W. Wang and A. P. Alivisatos *Science* **2001**, *292*, 2060.
- [47] X. Chen, A. Nazzal, D. Goorskey, M. Xiao, Z. A. Peng and X. Peng *Phys. Rev. B*

- 2001**, *64*, 5304.
- [48] M. Kazes, D. Y. Lewis, Y. Ebenstein, T. Mokari and U. Banin *Adv. Mater.* **2002**, *14*, 317.
- [49] D. Katz, T. Wizansky, O. Millo, E. Rothenberg, T. Mokari and U. Banin *Phys. Rev. Lett.* **2002**, *89*, 86801.
- [50] C. B. Murray, D. J. Norris, M. G. Bawendi, *J. Am. Chem. Soc.* **1993**, *115*, 8706.
- [51] M. C. Schlamp, X. G. Peng, A. P. Alivisatos *J. Appl. Phys.* **1997**, *82*, 5837.
- [52] W. Huynh, J. J. Dittmer, A. P. Alivisatos *Science* **2002**, *295*, 2425.
- [53] V. I. Klimov, A. A. Mikhailovsky, S. Xu, A. Malko, J. A. Hollingsworth, C. A. Leatherdale, H. J. Eisler, M. G. Bawendi *Science* **2000**, *290*, 314.
- [54] M. P. Bruchez, M. Moronne, P. Gin, S. Weiss, A. P. Alivisatos *Science* **1998**, *281*, 2013.
- [55] A. P. Alivisatos *Science* **1996**, *271*, 933.
- [56] M. Brust, C. J. Kiely *Colloids Surf. A: Physicochem. Eng. Asp.* **2002**, *202*, 175.
- [57] R. P. Andres, T. Bein, M. Dorogi, S. Feng, J. I. Jenderson, C. P. Kubiak, W. Mahoney, R. G. Osifchin, R. Reifengerger *Science* **1996**, *272*, 1323.
- [58] J. Ouyang, C. -W. Chu, D. Sieves, Y. Yang *Appl. Phys. Lett.* **2005**, *86*, 123507.
- [59] U. Simon *Adv. Mater.* **1998**, *10*, 1487.
- [60] T. Sato, H. Ahmed, D. Brown, B. F. H. Johnson, *J. Appl. Phys.* **1997**, *82*, 696.
- [61] C. A. Mirkin, T. A. Taton *Nature* **2000**, *405*, 626.
- [62] A. P. Alivisatos, K. P. Johnsson, X. Peng, T. E. Wislon, C. J. Loweth, M. P. Bruchez, P. G. Schultz *Nature* **1996**, *382*, 609.

- [63] A. Ueda, T. Oshima, M. Haruta *Appl. Catal. B* **1997**, *12*, 81.
- [64] A. A. Middleton, N. S. Wingreen *Phys. Rev. Lett.* **1993**, *71*, 3198.
- [65] U. Geigenmuller, G. Schon, *Europhys. Lett.* **1989**, *10*, 765.
- [66] H. Fan, K. Yang, D. M. Boye, T. Sigmon, K. J. Malloy, H. Xu, G. P. López, C. J. Brinker *Science* **2004**, *304*, 567.
- [67] C. T. Black, C. B. Murray, R. L. Sandstrom, S. Sun *Science* **2000**, *290*, 1131.
- [68] S. Datta, W. Tian, S. Hong, R. Reifenberger, J. Henderson, C. P. Kubiak, *Phys. Rev. Lett.* **1997**, *79*, 2530.
- [69] D. R. Lamb, “Electrical Conduction Mechanisms in Thin Insulating Films”, Methue, London, **1967**.
- [70] C.P. Collier, G. Mattersteig, E. W. Wong, Y. Luo, K. Beverly, J. Sampaio, F. M. Raymo, J. F. Stoddart, and J. R. Heth, *Science* **2000**, *289*, 1171.
- [71] M. A. Reed, J. Chen, A. M. Rawlett, D. W. Price, and J. M. Tour, *Appl. Phys. Lett.* **2001**, *78*, 3735.
- [72] L. A. Bumm, J. J. Arnold, T. D. Dunbar, D. L. Allara, and P. S. Weiss, *J. Phys. Chem. B* **1999**, *103*, 8122.
- [73] D. J. Wold, R. Haag, M. A. Rampi, and C. D. Frisbie, *J. Phys. Chem. B* **2002**, *106*, 2813.
- [74] X. D. Cui, X. Zarate, J. Tomfohr, O. F. Sankey, A. Primak, A. L. Moore, T. A. Moore, D. Gust, G. Harris, and S. M. Lindsay, *Nanotechnology* **2002**, *13*, 5.
- [75] R. Holmlin, R. Haag, M. L. Chabinyc, R. F. Ismagilov, A. E. Cohen, A. Terfort, M. A. Rampi, and G. M. Whitesides, *J. Am. Chem. Soc.* **2001**, *123*, 5075.
- [76] M. P. Samanta, W. Tian, S. Datta, J. I. Henderson, and C. P. Kubiak, *Phys. Rev. B* **1996**, *53*, R7636.
- [77] G. H. Parker and C. A. Mead, *Phys. Rev. Lett.* **1968**, *21*, 605.
- [78] B. Brar, G. D. Wilk, and A. C. Seabaugh, *Appl. Phys. Lett.* **1996**, *69*, 2728.

- [79] X. D. Cui, A. Primak, X. Zarate, J. Tomfohr, O. F. Sankey, A. L. Moore, T. A. Moore, D. Gust, L. A. Nagahara, and S. M. Lindsay, *J. Phys. Chem. B* **2002**, *106*, 8609.
- [80] Although the HOMO-LUMO gap of alkyl chain type molecules has been reported (see references [92]), there is no experimental data on HOMO-LUMO gap for Au/alkanethiol SAM/Au system. 8 eV is commonly used as HOMO-LUMO gap of alkanethiol.
- [81] C. Boulas, J. V. Davidovits, F. Rondelez, and D. Vuillaume, *Phys. Rev. Lett.* **1996**, *76*, 4797.
- [82] W. Huynh, J. J. Dittmer, A. P. Alivisatos, *Science* **2002**, *295*, 2425.
- [83] H. Fan, K. Yang, D. M. Boye, T. Sigmon, K. J. Malloy, H. Xu, G. P. López, C. J. Brinker, *Science* **2004**, *304*, 567.
- [84] a) A. L. Roest, J. J. Kelly, D. Vanmaekelbergh *Phys. Rev. Lett.* **2002**, *89*, 036801;
b) A. L. Roest, J. J. Kelly, D. Vanmaekelbergh *Appl. Phys. Lett.* **2003**, *83*, 5530.
- [85] D. Yu, C. Wang, P. Guyot-Sionnest, *Science* **2003**, *300*, 1277.
- [86] W. P. Wuelfing, S. J. Green, J. J. Pietron, D. E. Cliffel, R. W. Murray, *J. Am. Chem. Soc.* **2000**, *122*, 11465.
- [87] R. J. Forster, L. Keane, *J. Electroanal. Chem.* **2003**, *554-555*, 345.
- [88] E. P. A. M. Bakkers, A. W. Marsman, L. W. Jenneskens, D. Vanmaekelbergh, *Angew. Chem.* **2000**, *112*, 2385-2388; *Angew. Chem. Int. Ed.* **2000**, *39*, 2297.
- [89] E. P. A. M. Bakkers, Z. Hens, A. Zunger, A. Franceschetti, L. P. Kouwenhoven, L. Gurevich, D. Vanmaekelbergh, *Nano Lett.* **2001**, *1*, 551.
- [90] J. P. Spatz, S. Mossmer, C. Hartmann, M. Möller, T. Herzog, M. Krieger, H. G. Boyen, P. Ziemann, B. Kabius, *Langmuir* **2000**, *16*, 407.
- [91] a) C. C. Weng, K. H. Wei, *Chem. Mater.* **2003**, *15*, 2936; b) C. C. Weng, C. P.

- Chen; C. H. Ting; K. H. Wei, *Chem. Mater.* **2005**, *17*, 3328.
- [92] Y. Lin, A. Böker, J. He, K. Sill, H. Xiang, C. Abetz, X. Li, J. Wang, T. Emrick, S. Long, Q. Wang, A. Balazs, T. P. Russell, *Nature* **2005**, *434*, 55.
- [93] Y. Kang, T. A. Taton, *Angew. Chem.* **2005**, *117*, 413.; *Angew. Chem. Int. Ed.* **2005**, *44*, 409.
- [94] N. Tesster, V. Medvedev, M. Kazes, S. Kan, U. Banin, *Science* **2002**, *295*, 1506.
- [95] X. D. Cui, X. Zarate, J. Tomfohr, O. F. Sankey, A. Primak, A. L. Moore, T. A. Moore, D. Gust, G. Harris, S. M. Lindsay, *Nanotechnology* **2002**, *13*, 5.
- [96] F. P. Zamborini, L. E. Smart, M. C. Leopold, R. W. Murry, *Anal. Chim. Acta* **2003**, *496*, 3.
- [97] a) A. Salomon, D. Cahen, S. Lindsay, J. Tomfohr, V. B. Engelkes, C. D. Frisbie, *Adv. Mater* **2003**, *15*, 1881; b) X. D. Cui, X. Zarate, J. Tomfohr, O. F. Sankey, A. Primak, A. L. Moore, T. A. Moore, D. Gust, G. Harris, S. M. Lindsay, *Nanotechnology* **2002**, *13*, 5.
- [98] N. Boden, R. J. Bushby, J. Clements, B. Movaghar, *J. Appl. Phys* **1998**, *83*, 3207.
- [99] We measured the HOMO and LUMO states of P4VP through the use of cyclic voltammetry (CV).
- [100] Z. A. Peng, X. Peng, *J. Am. Chem. Soc.* **2001**, *123*, 183.
- [101] a) D. Xu, G. D. Watt, J. N. Harb, R. C. Davis *Nano Lett.* **2005**, *5*, 571; b) Y. Kawabe, M. M. Morrell, G. E. Jabbour, S. E. Shahan, B. Kippelen, *J. Appl. Phys* **1998**, *84*, 5306.
- [102] C. I. Zanetti, A. Mechler, S.A. Carter, R. Lal, *Adv. Mater.* **2004**, *16*, 385.
- [103] We calculated the concentration of CdSe in the P4VP domain (mol/cm^3) from

the loading amount of CdSe in P4VP. The value of C obtained by dividing the entire mole of CdSe by the entire volume of P4VP.

- [104] W. J. Parak, T. Pellegrino, C. M. Micheel, D. Gerion, S. C. Williams, A. P. Alivisatos, *Nano Lett.* **2003**, *3*, 33.
- [105] M. Brust, M. Walker, D. Bethell, D. J. Schiffrin, R. Whyman, *J. Chem. Soc. Chem. Commun.* **1994**, 801.
- [106] C. B. Murray, C. R. Kagan, M. G. Bawendi *Annu. Rev. Mater. Sci.* **2000**, *30*, 545.
- [107] J. Ouyang, C. -W. Chu, D. Sieves, Y. Yang, *Appl. Phys. Lett.* **2005**, *86*, 123507.
- [108] U. Simon *Adv. Mater.* **1998**, *10*, 1487.
- [109] C. A. Mirkin, T. A. Taton, *Nature* **2000**, *405*, 626.
- [110] A. Ueda, T. Oshima, M. Haruta *Appl. Catal. B* **1997**, *12*, 81.
- [111] C. P. Collier, R. J. Saykally, J. J. Shiang, S. E. Henrichs, J. R. Heath, *Science* **1997**, *277*, 1978.
- [112] R. Parthasarathy, X. M. Lin, H. M. Jaeger *Phys. Rev. Lett.* **2001**, *87*, 186807.
- [113] H. Fan, K. Yang, D. M. Boye, T. Sigmon, K. J. Malloy, H. Xu, G. P. López, C. J. Brinker *Science* **2004**, *304*, 567.
- [114] C. T. Black, C. B. Murray, R. L. Sandstrom, S. Sun *Science* **2000**, *290*, 1131.
- [115] P. Beecher, A. J. Quinn, E. V. Shevchenko, H. Weller, G. Redmond *J. Phys. Chem. B* **2004**, *108*, 9564.
- [116] a) W. P. Wuelfing, S. J. Green, J. J. Pietron, D. E. Cliffel, R. W. Murry, *J. Am. Chem. Soc.* **2000**, *122*, 11465. b) W. P. Wuelfing, R. W. Murry, *J. Phys. Chem. B* **2002**, *106*, 3139.
- [117] E. P. A. M. Bakkers, A. W. Marsman, L. W. Jenneskens, D. Vanmaekelbergh, *Angew. Chem. Int. Ed.* **2000**, *39*, 2297.
- [118] a) Y. Lin, A. Böker, J. He, K. Sill, H. Xiang, C. Abetz, X. Li, J. Wang, T. Emrick,

- S. Long, Q. Wang, A. Balazs, T. P. Russell, *Nature* **2005**, *434*, 55. b) Q. Zhang, S. Gupta, T. Emrick, T. P. Russell, *J. Am. Chem. Soc.* **2005**, *128*, 3898.
- [119] a) B. J. Kim, J. J. Chiu, G. -R. Yi, D. J. Pine, E. J. Kramer, *Adv. Mater.* **2005**, *17*, 2618. b) J. J. Chiu, B. J. Kim, E. J. Kramer, D. J. Pine, *J. Am. Chem. Soc.* **2005**, *127*, 5036.
- [120] T. Ruotsalainen, J. Turku, P. Heikkilä, J. Roukolainen, A. Nykänen, T. Laitinen, M. Torkkeli, R. Serimaa, G. T. Brinke, A. Harlin, O. Ikkala, *Adv. Mater.* **2005**, *17*, 1048.
- [121] A. M. Urbas, M. Maldovan, P. DeRege, E. L. Thomas, *Adv. Mater.* **2002**, *14*, 1850.
- [122] a) C. P. Li, K. H. Wei, J. Y. Huang, *Angew. Chem. Int. Ed.* **2006**, *45*, 1449. b) C. P. Li, S. W. Yeh, H. C. Chang, J. Y. Huang, K. H. Wei, *Small* **2006**, *2*, 359.
- [123] a) J. P. Spatz, S. Mossmer, C. Hartmann, M. Möller, T. Herzog, M. Krieger, H. G. Boyen, P. Ziemann, B. Kabius, *Langmuir* **2000**, *16*, 407. b) J. P. Spatz, V. Z. H. Chan, S. Mößmer, F. -M. Kamm, A. Plettl, P. Ziemann, M. Möller, *Adv. Mater.* **2002**, *14*, 1827.
- [124] A. A. Middleton, N. S. Wingreen, *Phys. Rev. Lett.* **1993**, *71*, 3198.
- [125] C. A. Neugebauer, M. B. Webb, *J. Appl. Phys.* **1962**, *33*, 74.
- [126] In two- and three-dimensional hexagonal arrays, each nanoparticle has six and twelve nearest neighbors, respectively.
- [127] a) J. W. Grebinski, K. L. Richter, J. Zhang, T. H. Kosel, M. Kuno, *J. Phys. Chem. B* **2004**, *108*, 9745. b) W. W. Weare, S. M. Reed, M. G. Warner, J. E. Hutchison, *J. Am. Chem. Soc.* **2000**, *122*, 12890.
- [128] a) W. P. Wuelfing, S. J. Green, J. J. Pietron, D. E. Cliffel, R. W. Murry, *J. Am. Chem. Soc.* **2000**, *122*, 11465. b) F. P. Zamborini, L. E. Smart, M. C. Leopold, R. W. Murry, *Anal. Chim. Acta* **2003**, *496*, 3.

- [129] a) T. Ruotsalainen, J. Turku, P. Heikkilä, J. Roukolainen, A. Nykänen, T. Laitinen, M. Torkkeli, R. Serimaa, G. T. Brinke, A. Harlin, O. Ikkala, *Adv. Mater.* **2005**, *17*, 1048–1052; b) S. Valkama, H. Kosonen, J. Ruokolainen, T. Haatainen, M. Torkkeli, R. Serimaa, G. T. Brinke, O. Ikkala, *Nature Mater.* **2004**, *3*, 872.
- [130] a) M. Park, C. Harrison, P. M. Chaikin, R. A. Register, D. H. Adamson, *Science* **1997**, *267*, 1401; b) Y. L. Loo, R. A. Register, A. J. Ryan, *Macromolecules* **2002**, *35*, 2365.
- [131] a) M. J. Misner, H. Skaff, T. Emrick, T. P. Russell, *Adv. Mater.* **2003**, *15*, 221; b) D. H. Kim, S. H. Kim, K. Lavery, T. P. Russell, *Nano Lett.* **2004**, *4*, 1841; c) Y. Lin, A. Böker, J. He, K. Sill, H. Xiang, C. Abetz, X. Li, J. Wang, T. Emrick, S. Long, Q. Wang, A. Balazs, T. P. Russell, *Nature* **2005**, *434*, 55.
- [132] a) A. M. Urbas, M. Maldovan, P. DeRege, E. L. Thomas, *Adv. Mater.* **2002**, *14*, 1850; b) M. Bockstaller, R. Olb, E. L. Thomas, *Adv. Mater.* **2001**, *13*, 1783.
- [133] a) J. P. Spatz, S. Mossmer, C. Hartmann, M. Möller, T. Herzog, M. Krieger, H. G. Boyen, P. Ziemann, B. Kabius, *Langmuir* **2000**, *16*, 407; b) J. P. Spatz, V. Z.-H. Chan, S. Mößmer, F.-M. Kamm, A. Plettl, P. Ziemann, M. Möller, *Adv. Mater.* **2002**, *14*, 1827.
- [134] S. W. Yeh, K. H. Wei, Y. S. Sun, U. S. Jeng, K. S. Liang, *Macromolecules* **2005**, *38*, 6559.

- [135] a) X. Duan, Y. Huang, R. Agarwal, C. M. Lieber, *Nature* **2003**, 421, 241; b) Y. Cui, Q. Wei, H. Park, C. M. Lieber, *Science* **2001**, 293, 1289.
- [136] L. K. vanVugt, S. J. Veen, E. P. A. M. Bakkers, A. L. Roest, D. Vanmaekelbergh, *J. Am. Chem. Soc.* **2005**, 127, 13257.
- [137] M. Artemyev, B. Möller, U. Woggon, *Nano Lett.* **2003**, 3, 509.
- [138] F. Kim, S. Kwan, J. Akana, P. Yang, *J. Am. Chem. Soc.* **2001**, 123, 4360.
- [139] a) W. U. Huynh, J. J. Dittmer, A. P. Alivisatos, *Science* **2002**, 295, 2425; b) J. Hu, L. S. Li, W. Yang, L. Manna, L. W. Wang, A. P. Alivisatos, *Science* **2001**, 292, 2060; c) L. S. Li, A. P. Alivisatos, *Adv. Mater.* **2003**, 15, 408.
- [140] Y. W. Su, C. S. Wu, C. C. Chen, C. D. Chen, *Adv. Mater.* **2003**, 15, 49.
- [141] M. H. Huang, S. Mao, H. Feick, H. Yan, Y. Wu, H. Kind, E. Weber, R. Russo, P. Yang, *Science* **2001**, 292, 1897.
- [142] a) O. Harnack, C. Pacholski, H. Weller, A. Yasuda, J. M. Wessels, *Nano Lett.* **2003**, 3, 1097; b) P. A. Smith, C. D. Nordquist, T. N. Jackson, T. S. Mayer, B. R. Martin, J. Mbindyo, T. E. Mallouk, *Appl. Phys. Lett.* **2000**, 77, 1399.
- [143] R. A. Mrozek, T. A. Taton, *Chem. Mater.* **2005**, 17, 3384.
- [144] a) T. Xu, A. V. Zvelindovsky, G. J. A. Sevink, O. Gang, B. Ocko, Y. Zhu, S. P. Gido, T. P. Russell, *Macromolecules* **2004**, 37, 6980; b) H. Xiang, Y. Lin, T. P. Russell, *Macromolecules* **2004**, 37, 5358.

- [145] H. A. Pohl, *J. Appl. Phys.* **1915**, 22, 869.
- [146] L. S. Li, A. P. Alivisatos, *Phys. Rev. Lett.* **2003**, 90, 097402.
- [147] a) D. Xu, G. D. Watt, J. N. Harb, R. C. Davis *Nano Lett.* **2005**, 5, 571; b) Y. Kawabe, M. M. Morrell, G. E. Jabbour, S. E. Shahan, B. Kippelen, *J. Appl. Phys.* **1998**, 84, 5306.
- [148] P. W. M. Blom, M. J. M. de Jong, J. J. M. Vleggar, *Appl. Phys. Lett.* **1996**, 68, 3308.
- [149] Z. A. Peng, X. Peng, *J. Am. Chem. Soc.* **2002**, 124, 3343.



Publication Lists

Chung-Ping Li, Kung-Hwa Wei and Jung Y. Huang, “Enhanced Collective Electron Transport by CdSe Quantum Dots Self-Assembled in the Poly(4-vinylpyridine) Nanodomains of a Poly(styrene-*b*-4-vinylpyridine) Diblock Copolymer Thin Film”, *Angew. Chem. Int. Ed.* **2006**, 45, 1449. (Impact Factor 9.161)

Chung-Ping Li, Siao-Wei Yeh, Han-Chang Chang, Jung Y. Huang, and Kung-Hwa Wei, “The Orientation of CdSe Nanorods Affects the Electron Mobility of CdSe/P4VP Nanodomains Self-Assembled within a Poly(styrene-*b*-4-vinylpyridine) Diblock Copolymer Thin Film”, *Small* **2006**, 2, 359. (starts at 2005, no Impact Factor until 2007)

Chung-Ping Li, Ching-Mao Huang, Meng-Ting Hsieh and Kung-Hwa Wei, “Properties of Covalently Bonded Layered-Silicate/Polystyrene Nanocomposites Synthesized via Atom Transfer Radical Polymerization”, *J. Polym. Sci. Part A: Polym. Chem.* **2005**, 43, 534. (Impact Factor 2.773)

Chung-Ping Li, Chia-Hao Wu, Kung-Hwa Wei, Jeng-Tzong Sheu, and Jung Y. Huang, “Collective Electron Transport in Au Nanoparticles Self-Assembled in the Poly(4-vinylpyridine) Nanodomains of a Poly(styrene-*b*-4-vinylpyridine) Diblock Copolymer Thin Film”, *J. Am. Chem. Soc.* **2006**, submitted. (Impact Factor 6.903)

學經歷資料

- 姓名：李中斌
- 性別：男
- 生日：67年9月22日，台南人
- 電子郵件信箱：binbinlee.mse89g@nctu.edu.tw
- 聯絡電話：(學校) 03-5731771 (手機) 0922-110935
- 通訊地址：新竹市 300 大學路 1001 號
國立交通大學材料與工程研究所
- 永久地址：台南縣麻豆鎮建南街 122 巷 1 號



學歷

博士候選人：國立交通大學材料科學與工程研究所	2000. 9 ~ 2006. 6
大學：國立彰化師範大學化學系	1996. 9 ~ 2000. 6

參與計畫

-
- 高效率光電轉換自身組織功能性奈米結構材料與元件之前瞻研究。(2005. 8 ~ 2006. 6)
 - 量子點/自身組織塊式高分子奈米複合材料。(2002. 1 ~ 2005. 12)
 - 原位(In-situ)聚合之無機層狀材/聚苯乙烯(PS)奈米複合材料之製備。(2001. 8~2002. 7)
 - 低介電溶膠凝膠聚亞醯胺(PI)奈米複合材料之製備。(2000. 9 ~ 2001. 7)

專長

-
- 光電量測與奈米操控技術：
 1. 奈米區塊(nanodomain)之光電性質之量測。
 2. 光電應用奈米材料操控與分散技術。
 3. 無機奈米結構(nanostructure)之合成、鑑定分析與其界面改質分散技術。
 - 有機/無機奈米複合材料：
 1. 原位聚合奈米分散技術。
 2. 構裝用低介電聚亞醯胺(PI)與/無機物奈米複合材料。
 - 分析儀器操作：

小角 X 光散射(SAXS)、原子力顯微鏡(AFM)、掃描穿隧顯微鏡(STM)、穿透式電子顯微鏡(TEM)、掃描式電子顯微鏡(SEM)、X 光繞射分析、超薄切片機、光學量測儀器、電性量測分析、紅外線光譜分析、紫外光-可見光光譜分析、熱分析(DSC, TGA, TMA)、粒徑分析、及真空蒸鍍設備操作。